

ABSTRACT

HATLEY, REBECCA LOUISE. Evaluation of Distributed Temperature Sensing and Hydraulic Modeling to Improve Scour Predictions at Bridge Crossings. (Under the direction of Dr. Celso Castro-Bolinaga and Dr. Chadi Sayde).

Despite major advances in predicting the spatial and temporal scales of scour phenomena at bridge crossings, bridge failure due to hydraulically induced scour still represents a major technical, economical, and societal challenge. One reason for the common inaccuracies exhibited by the predictive equations is the lack of data with adequate resolution for validation and verification purposes. Application of scour-predicting equations typically consists of producing one-dimensional (1D) or two-dimensional (2D) numerical models to simulate the hydraulic processes in the stream. HEC-RAS (1D) and SRH-2D (2D) are common models being used. In most cases, scour data are collected immediately following flood events because of the difficulties associated with using and deploying conventional collection methods in real time. This means that post-event measurements do not capture the maximum scour depth, but rather a net value caused by both erosion and deposition processes. An alternative method to monitor scour phenomena is distributed temperature sensing (DTS). The DTS has the capability of taking measurements every second, so the maximum scour depth can be determined before sedimentation occurs again. The data from the DTS can be used to evaluate existing empirical methods, as well as to validate hydro-morphodynamic numerical models that allows for the examination of phenomena under a range of conditions that are difficult to measure in the field or to reproduce using physical models. Ultimately, the coupling of real-time measurements with hydro-morphodynamic numerical models will lead to a more detailed understanding of how scour holes form.

© Copyright 2022 by Rebecca Hatley

All Rights Reserved

Evaluation of Distributed Temperature Sensing and Hydraulic Modeling to Improve Scour
Predictions at Bridge Crossings

by
Rebecca Hatley

A thesis submitted to the Graduate Faculty of
North Carolina State University
in partial fulfillment of the
requirements for the degree of
Master of Science

Biological and Agricultural Engineering

Raleigh, North Carolina
2022

APPROVED BY:

Dr. Celso Castro-Bolinaga
Committee Co-Chair

Dr. Chadi Sayde
Committee Co-Chair

Dr. Alejandra Ortiz

DEDICATION
To my supportive family and friends.

BIOGRAPHY

Rebecca Hatley grew up in Arlington, Texas. As a kid, she loved to perform science experiments in the backyard. Usually these “science experiments” consisted of making mud canals and pouring water in them to see what happened. When she was 13 years old, she was introduced to a fluvial geomorphologist at her mom’s engineering firm. After learning about fluvial geomorphology, Rebecca became completely obsessed with rivers and has been ever since.

When it was time to go to college, Rebecca, being raised to bleed the brightest orange, had only one option: study Geology at Oklahoma State University (OSU). During her undergraduate studies, Rebecca enjoyed learning about the natural processes that shaped the earth. She excelled in the Geology program and as a senior became the Boone Pickens School of Geology Outstanding Senior. Also, during her time at OSU, Rebecca was involved in the Supplemental Instruction (SI) program. She started out as a Geology 101 SI leader in which she led structured study sessions weekly. She then rose in ranks to become an SI mentor. In her role as SI mentor, she learned that she greatly enjoyed helping her colleagues grow in their professional and personal skills.

After graduating from OSU, Rebecca decided to go to North Carolina State for her Master’s in Biological and Agricultural Engineering. There she focused on studying river dynamics and sediment transport. During her time at NC State, Rebecca enjoyed meeting new friends who were also passionate about rivers and taking wonderful classes.

Next on Rebecca’s journey is moving to Madison, WI and working at Stantec as an environmental engineer focusing on ecosystem restoration and stormwater improvements. Rebecca is looking forward to her next challenge.

ACKNOWLEDGMENTS

First off, I would like to acknowledge my two advisors, Dr. Castro-Bolinaga and Dr. Sayde, for their constant support and advice during my time at NC State. They have given me immense technical knowledge as well as valuable professional development skills. Secondly, I would also like to thank Dr. Ortiz for her guidance on my research in being part of my committee. In addition, I would like to acknowledge my fellow graduate students who have helped me in data collection and analysis. In particular, I would like to thank Mahmoud Shehata for all of his help with the fiber optic component of my research as well as Hanieh Mohamdi Moghadam for all of her help in field work.

This work would not have been possible without the support of the North Carolina Department of Transportation. The NCDOT has supported me every step of the way by not only funding the project, but also assisting in data collection and having a keen interest in the project.

I would next like to thank the many friends I have met in Raleigh. Specifically, Alexis Swanson who has been a great friend and support through graduate school.

Finally, if it were not for the constant and never-ending support from Andrew Hillman, none of this would have been possible. Thank you for all that you do for me.

TABLE OF CONTENTS

LIST OF TABLES.....	vii
LIST OF FIGURES	ix
Chapter 1: Introduction	1
1.1 Motivation.....	1
1.2 Thesis Overarching Goals and Specific Objectives.....	4
1.3 Technical Background	4
1.3.1 Predictive Equations for Bridge Scour	4
1.3.2 Numerical Modeling of Bridge Scour.....	7
1.3.3 Distributed Temperature Sensing Background.....	9
1.3.4 FO-DTS Applications in Environmental Research.....	11
Chapter 2: FO-DTS Experiments.....	13
2.1 Introduction.....	13
2.2 Methods.....	14
2.2.1 Flume Description.....	14
2.2.2 FO Device Description	15
2.2.3 Experiment Design.....	17
2.2.4 Field Installation	19
2.3 Results and Discussion	20
2.3.1 Prototype 1 Results	20
2.3.2 Prototype 2 Results	28
2.3.3 Field Installation Results.....	38
2.4 Conclusions.....	41

Chapter 3: One-Dimensional (1D) and Two-Dimensional (2D) Bridge Scour Modeling....	43
3.1 Introduction.....	43
3.2 Study Area and Selected Bridge Crossings	44
3.2.1 Ellerbe Creek	45
3.2.2 Middle Creek	46
3.2.3 Tar River	47
3.2.4 Roanoke River	48
3.3 Methods.....	49
3.3.1 Overview of Model Development and Modeling Workflow.....	49
3.3.2 Ellerbe Creek	54
3.3.3 Middle Creek	56
3.3.4 Tar River	58
3.3.5 Roanoke River	61
3.4 Results and Discussion	64
3.4.1 Ellerbe Creek	64
3.4.2 Middle Creek	75
3.4.3 Tar River	85
3.4.4 Roanoke River	93
3.4.5 Comparison of Bridge Crossings.....	104
3.5 Conclusions.....	110
Chapter 4: Conclusions	112
References.....	115
Appendices.....	119

LIST OF TABLES

Table 3.1 Relative Mean Absolute Error (RMAE) criteria from van Rijn et al. (2003) used for model calibration.....	52
Table 3.2 A comparison of the four channel-bed sediment samples taken at Ellerbe Creek.	68
Table 3.3 The summary of the calibration results of both hydrodynamic models for Ellerbe Creek.	69
Table 3.4 The results of the mesh calibration for the Ellerbe Creek SRH-2D model.	70
Table 3.5 A summary of the HEC-RAS 1D results for the various discharges.....	70
Table 3.6 The comparison of scour depths between 1D and 2D models at Ellerbe Creek.....	76
Table 3.7 Summary of the characteristics of the channel-bed sediment at Middle Creek.....	78
Table 3.8 Summary of both the hydrodynamic model calibration results at Middle Creek.....	79
Table 3.9 The results of the mesh calibration in SRH-2D at Middle Creek.	80
Table 3.10 Description of each discharge evaluated for Middle Creek.....	80
Table 3.11 Summary of the HEC-RAS 1D results for Middle Creek.	81
Table 3.12 Summary of the scour depth results in both 1D and 2D modeling approaches.....	86
Table 3.13 Characteristics of the channel-bed material sample taken at Tar River.	87
Table 3.14 The summary of the hydrodynamic models' calibration results at Tar River.	88
Table 3.15 The results of the mesh calibration of Tar River in SRH-2D.	89
Table 3.16 The discharges used to evaluate the Tar River.	89
Table 3.17 The summary of the 1D results for the steady flow simulations on Tar River.....	90
Table 3.18 The comparison between the scour depths of the 1D and 2D modeling approaches at the Tar River.	94
Table 3.19 Characteristics of the channel-bed sediment samples taken at the Roanoke River... .	95

Table 3.20 The hydrodynamic models' calibration results for the Roanoke River.....	97
Table 3.21 The mesh calibration results of the 2D model of the Roanoke River.....	98
Table 3.22 The discharges used to evaluate the Roanoke River.....	98
Table 3.23 Summary of the HEC-RAS 1D results for steady flow simulations.	98
Table 3.24 Comparison of 1D and 2D pier scour estimates for the Roanoke River.....	104
Table 3.25 The 1D HEC-18 produced values of pier scour used for normalization for Ellerbe Creek.....	108
Table 3.26 The 1D HEC-18 produced values of pier scour used for normalization for Middle Creek.....	109
Table 3.27 The 1D HEC-18 produced values of pier scour used for normalizations for Tar River.....	109
Table 3.28. The 1D HEC-18 produced values of pier scour used for normalization for Roanoke River.....	110

LIST OF FIGURES

Figure 2-1 Photograph of the flume used to test the FO-DTS prototype performance..	14
Figure 2-2 Prototype 1 was constructed by wrapping a fiber optic cable around a 5 cm diameter pipe. The total length of the wrapped section is 60 cm.	15
Figure 2-3 Prototype 2 was constructed by wrapping a fiber optic cable around a 5 cm diameter pipe. The total length of the wrapped section is 30 cm.	17
Figure 2-4 A cross-sectional view of the BRUsens fiber optic cable. Adapted from DeBell, 2021.....	17
Figure 2-5 The field setup of the two devices at Ellerbe Creek in Durham, NC.....	20
Figure 2-6 The results of the zero-flow condition for prototype 1. The x-axis represents both the mean temperature increase (blue line) and the temperature gradient (red line) observed along the cable while the y-axis is the vertical distance along the prototype. The vertical distance of zero represents the bottom of the prototype which was fully buried under sediment. The green star represents the calculated sediment-water interface, and the pink star marks the calculated water-air interface. The horizontal blue and black lines represent the location of the independently measured sand-water and water-air interfaces respectively.....	21
Figure 2-7 Error of sediment interface location versus heating time under zero flow for Prototype 1.....	22
Figure 2-8 The results of the low flow condition for prototype 1. The x-axis represents both the mean temperature increase (blue line) and the temperature gradient (red line) observed along the cable while the y-axis is the vertical distance along the prototype. The vertical distance of zero represents the bottom of the	

prototype which was fully buried under sediment. The green star represents the calculated sediment-water interface, and the pink star marks the calculated water-air interface. The horizontal blue and black lines represent the location of the independently measured sand-water and water-air interfaces respectively..... 24

Figure 2-9 The error of sediment interface location versus heating time under low flow for Prototype 1. 25

Figure 2-10 The results of the high flow condition for prototype 1. The x-axis represents both the mean temperature increase (blue line) and the temperature (red line) observed along the cable while the y-axis is the vertical distance along the prototype. The vertical distance of zero represents the bottom of the prototype which was fully buried under sediment. The green star represents the calculated sediment-water interface, and the pink star marks the calculated water-air interface. The horizontal blue and black lines represent the location of the independently measured sand-water and water-air interfaces respectively..... 25

Figure 2-11 The error of sediment interface location versus heating time under high flow..... 26

Figure 2-12 The before and after plots of the sediment-water and water-air interfaces in the scour-inducing experiment. 27

Figure 2-13 The results from the no flow tests. The x-axis is the temperature difference between immediately before heating began and after the heating stopped and the y-axis is the height of the device in centimeters. The green star represents the sand and water interface. The red star represented the water-air interface,

and the difference between the two stars was the water depth.....	29
Figure 2-14 The error versus heating time increments for the no flow tests.....	30
Figure 2-15 The results from the medium flow tests: test 1 (a), test 2 (b), and test 3 (c). The sand-water interface was indicated by the green star and the water-air interface by the red star.....	32
Figure 2-16 The error versus heating time increments for the medium flow tests.....	33
Figure 2-17 The results from the maximum flow tests: test 1 (a), test 2 (b), and test 3 (c). The sand-water interface was indicated by the green star and the water-air interface by the red star	35
Figure 2-18 The error versus heating time increments for the maximum flow tests.....	36
Figure 2-19 The results from the first device in the field installation. The green star represents the detected sediment-water interface while the red represents the water-air interface.....	39
Figure 2-20 The results from the second device in the field installation.....	40
Figure 3-1 A map of the selected bridge crossings. Ellerbe Creek is marked in yellow, Middle Creek in purple, Tar River in blue, and the Roanoke River in red.	44
Figure 3-2 The Glenn Rd bridge crossing over Ellerbe Creek in Durham, NC, USA viewed from upstream (a) and downstream (b). The channel-bed material is characterized as medium sand with less than 5% fines (c).	45
Figure 3-3 The NC-50 bridge crossing over Middle Creek in Johnston County, NC viewed from downstream.....	46
Figure 3-4 The US-401 bridge crossing over the Tar River in Louisburg, NC viewed from upstream.....	47

Figure 3-5 The US-258 bridge crossing over the Roanoke River close to Scotland Neck, NC viewed from downstream.....	49
Figure 3-6 Flowchart illustrating the general steps followed in the model development and modeling workflow.....	50
Figure 3-7 Plan view of the river terrain model in HEC-RAS 1D of Ellerbe Creek. The Cross-sections are in green, and the stream centerline is in blue. This image does include the interpolated cross sections. Flow direction is from left to right... ..	56
Figure 3-8 The mesh elements produced for Ellerbe Creek in SRH-2D. Flow direction is from left to right.....	56
Figure 3-9 The HEC-RAS 1D river terrain model for Middle Creek. The cross sections are in green, and the stream centerline is in blue. This image does include the interpolated cross sections. Flow direction is from left to right.. ..	58
Figure 3-10 The mesh elements for Middle Creek in SRH-2D. Flow direction is from left to right.....	59
Figure 3-11 The ADCP being pulled by ropes across the Tar River.	60
Figure 3-12 A snapshot of the Tar River model in RAS Mapper. The cross sections are in green, and the stream centerline is in blue. This image does include the interpolated cross sections. Flow direction is from left to right.....	61
Figure 3-13 The mesh elements for the Tar River in SRH-2D. Flow direction is from left to right.....	62
Figure 3-14 The ADCP attached to the side of the motorboat.	63
Figure 3-15 A snapshot of the Roanoke River model in RAS Mapper. Flow direction is from left to right.....	64

Figure 3-16 The mesh elements for Roanoke River in SRH-2D. Flow direction is from left to right.....	65
Figure 3-17 The grain size distribution of the channel-bed sediment collected approximately 30 m upstream of the bridge.....	66
Figure 3-18 The grain size distribution of the channel-bed sediment collected at the bridge.	66
Figure 3-19 The grain size distribution of the channel-bed sediment collected immediately downstream of the bridge	67
Figure 3-20 The grain size distribution of the channel-bed sediment collected approximately 30 m downstream of the bridge.....	67
Figure 3-21 The comparison of both hydrodynamic models to the USGS gauge at Ellerbe Creek.	68
Figure 3-22 The normalized values of stage for the bankfull flow ($57 \text{ m}^3/\text{s}$) at Ellerbe Creek.....	70
Figure 3-23 A comparison of the maximum and median normalized depths at Ellerbe Creek.	72
Figure 3-24 The normalized values of velocity for the bankfull flow at Ellerbe Creek.....	73
Figure 3-25 A comparison of the maximum and median normalized velocities at Ellerbe Creek.	73
Figure 3-26 The normalized values of shear stress for the bankfull flow at Ellerbe Creek.	74
Figure 3-27. A comparison of the maximum and median normalized shear stresses at Ellerbe Creek.	75
Figure 3-28 The grain size distribution of the farthest upstream channel-bed sediment sample.	77
Figure 3-29 The grains size distribution of the channel-bed sediment sample taken	

immediately upstream of the bridge.....	77
Figure 3-30 The grain size distribution of the downstream channel-bed sediment sample at Middle Creek.....	78
Figure 3-31 The comparison between the USGS gauge, HEC-RAS 1D, and SRH-2D stages ..	79
Figure 3-32 The normalized stage results at bankfull flow at Middle Creek.	82
Figure 3-33 A comparison of the maximum and median normalized depths at Middle Creek.	82
Figure 3-34 The normalized velocity values for bankfull flow at Middle Creek.	83
Figure 3-35 A comparison of the maximum and median normalized velocities at Middle Creek.	84
Figure 3-36 The normalized shear stress values for bankfull conditions at Middle Creek.	85
Figure 3-37 A comparison of the maximum and median normalized shear stresses at Middle Creek.	85
Figure 3-38 The results of the grain size distribution from the Tar River.....	86
Figure 3-39 The comparison of the USGS gauge, HEC-RAS 1D, and SRH-2D stages.	88
Figure 3-40 The stage results at bankfull flow for the Tar River.	91
Figure 3-41 A comparison of normalized depths at the Tar River.	91
Figure 3-42 The velocity results at bankfull flow for the Tar River.....	92
Figure 3-43. A comparison of normalized velocities at the Tar River.	92
Figure 3-44 The results of shear stress for bankfull flow for the Tar River.	93
Figure 3-45 A comparison of normalized shear stresses at the Tar River.	93
Figure 3-46 The grain size distribution of the upstream channel-bed sediment sample at Roanoke River.....	94

Figure 3-47 The grain size distribution of the channel-bed sediment sample under the bridge at Roanoke River.....	94
Figure 3-48 The grain size distribution of the downstream channel-bed sediment sample at Roanoke River.....	95
Figure 3-49 The comparison of the USGS gauge, HEC-RAS 1D, and SRH-2D stages.	96
Figure 3-50 The normalized values of stage at the bankfull flow of Roanoke River.....	100
Figure 3-51 A comparison of the maximum and median normalized depths at Roanoke River.	100
Figure 3-52 The normalized values of velocity at the bankfull flow of Roanoke River.	101
Figure 3-53 A comparison of the maximum and median normalized velocities at Roanoke River.	101
Figure 3-54 The normalized values of shear stress at bankfull at the Roanoke River.....	102
Figure 3-55 A comparison of the maximum and median normalized shear stresses at the Roanoke River.	103
Figure 3-56 All four plots of stage maximum and median values for the bridge crossings.	105
Figure 3-57 All four plots of velocity maximum and median values for the bridge crossings.	106
Figure 3-58 All four plots of shear stress maximum and median values for the bridge crossings.	107
Figure 3-59 Comparison of normalized scour depth predictions for each bridge crossing.	108

CHAPTER 1: INTRODUCTION

1.1 Motivation

Scour refers to the removal of channel-bed or streambank material due to the erosive action of flowing water (Arneson et al., 2012). In the case of bridge crossings, scour is generated by the reduction of the channel cross-sectional area as water flows under the bridge and by changes imposed to the flow field by the presence of bridge foundations (e.g., piers and abutments). An accurate prediction of the scour hole dimensions is of paramount importance for bridge design and assessment. Such prediction is used to guide, for example, the selection of an adequate foundation depth to guarantee that the bridge structure is not compromised during major flood events.

Despite major advances in predicting the spatial and temporal scales of scour phenomena at bridge crossings, bridge failure due to hydraulically induced scour still represents a major technical, economical, and societal challenge. Approximately 60% of bridge failures in the U.S. between 1960 and 1990 were caused by scour-related issues, resulting in an average of \$30 million of damage each year (Deng and Cai, 2009). Likewise, the Bridge Scour Evaluation Program reported in 2011 that 4.7% or approximately 23,000 bridges in the U.S. are scour critical, implying these bridges are more likely to fail when subjected to a severe hydrologic event (Arneson et al., 2012).

Albeit bridge scour phenomena have been studied for several decades, currently used equations used tend to significantly overpredict the amount of scour (Landers and Mueller, 1996). Overpredicting scour results in a safer design but is less cost effective due to required deeper foundation depths and/or expensive countermeasures. One reason for the inaccuracies exhibited by scour predictive equations is the lack of data with adequate spatial and temporal

resolution for validation and verification purposes. In most cases, for example, scour data are collected immediately following flood events because of the difficulties associated with using and deploying conventional collection methods in real time. Scour holes typically form and reach maximum depth during flood events, but on the falling side of the hydrograph, the hole might start to fill in again. This means that post-event most measurements are not likely to capture maximum scour depths, but rather net values caused by both erosional and depositional processes.

Typically, applying scour-predictive equations involves developing one-dimensional (1D) or two-dimensional (2D) process-based numerical models to resolve hydraulic processes in the stream (e.g., USACE HEC-RAS (1D) and USBR SRH-2D). In recent years, the application of 2D hydrodynamic models have become more frequent due to the availability of high-resolution digital elevation models and improved flow measurement devices. However, the accuracy of these higher-dimensional models remains constrained by the quality of input data and the reliability of needed empirical equations (e.g., sediment transport functions) (Lai and Greimann, 2008)

Input data for bridge scour modeling include information on the channel cross-sectional geometry, channel-bed sediment properties, and bridge substructure geometry. Part of these data are collected by each state's Department of Transportation (DOT), which is responsible for the periodical inspection of its bridge crossings. During the inspections, information regarding changes in channel-bed elevation or cross-sectional shape (including the presence of scour holes), damage to riprap or other countermeasures, and the state of the bridge substructure is collected. Characterizing the channel-bed sediment properties is not typically included, and

because of the frequency of these inspections (which is typically every other year), measurements of channel-bed elevation changes are not likely to capture maximum scour depths.

If scour is detected at a bridge crossing, or if the likelihood of scour deemed high, there are two main types of devices that can be deployed to monitor channel-bed elevation changes. The first type is portable devices, which includes rods or sonic fathometers. Portable devices require someone to be there to read and record the data, reducing the temporal resolution of scour measurements. These devices are commonly used to measure the distance from the bridge deck to the channel bed (Arneson et al., 2012). While sonic fathometers have been found to accurately measure scour depths from 0.23 m to 1.2 m (Fisher et al., 2013) high suspended sediment concentrations, large amount of debris, and temperature variations can greatly impact the device's accuracy. The second type is a fixed monitoring device, which collects and records data on its own without requiring supervision, increasing the temporal resolution of scour measurements. A common fixed monitoring device is time domain reflectometry (TDR). This device sends out electromagnetic waves to determine where channel-bed sediment and water interact, providing a high spatial resolution of scour measurements. However, TDR is prone to the same issues that impact the accuracy of sonic fathometers.

Fiber-Optic Distributed Temperature Sensing (FO-DTS) provides an alternative and reliable method of address these limitations while providing high spatial and temporal resolution of scour measurements at bridge crossings. It has been reported that FO-DTS can record temperature changes every second and every 0.1 m for distances of up to 10,000 m (Chen et al. 2017) Moreover, a temperature resolution as low as 0.1 °C can be achieved with proper calibration and long averaging time (Hausner et al., 2011). For scour-monitoring, temperature is used as a tracer to reveal the location of the interface between the channel-bed sediment and

water, as they are expected to dissipate heat at different rates, thereby producing different thermal responses to heat perturbation along a FO-DTS sensor embedded in both materials.

1.2 Thesis Overarching Goals and Specific Objectives

The overarching goal of this thesis was to evaluate the contribution of FO-DTS and process-based hydrodynamic numerical models toward improving scour predictions at bridge crossings. To accomplish this goal, the specific objectives of this thesis are: (1) to develop and test a FO-DTS scour monitoring device capable of tracking changes in the sediment-water interface at high spatial and temporal resolutions (Chapter 2); and (2) to compare the performance of 1D and 2D process-based numerical models when resolving the flow field and predicting maximum scour depths at bridge crossings (Chapter 3).

1.3 Technical Background

1.3.1 Predictive Equations for Bridge Scour

Under guidelines from the FHWA in Hydraulic Engineering Circular No. 18 (HEC-18), most states' department of transportation (DOT) engineers use the HEC-18 pier scour equation (Equation 2.1) (Arneson et al., 2012). This equation was recommended for both live-bed and clear-water scour and is given as:

$$\frac{y_s}{y_1} = 2K_1 K_2 K_3 \left(\frac{a}{y_1}\right)^{0.65} Fr_1^{0.43} \quad (1.1)$$

where y_s is the scour depth (ft or m), y_1 is the flow depth directly upstream of the pier (ft or m), K_1 is a correction factor for the shape of the pier nose, K_2 is a correction factor for the flow's angle of attack, K_3 is a correction factor for the bed condition, a is the pier width (ft or m), and Fr_1 is the Froude number upstream of the pier. This equation has been adjusted to fit wide and complex piers as well as for cohesive bed materials, but those adaptations are not presented in this review.

Contraction scour is often estimated by either Laursen's live-bed scour or clear-water scour equation (Arneson et al., 2012) (Equation 2.2). A modified version of Laursen's 1960 equation for live-bed scour is as follows:

$$\frac{y_2}{y_1} = \left(\frac{Q_2}{Q_1} \right)^{6/7} \left(\frac{W_1}{W_2} \right)^{K_1} \quad (1.2)$$

where y_2 is the average depth in the contracted section of the channel (ft or m), y_1 is the average depth upstream of the contracted section (ft or m), Q_1 is the flow in the upstream reach (ft^3/s or m^3/s), Q_2 is the flow in the contracted section (ft^3/s or m^3/s), W_1 is the bottom width in the upstream reach (ft or m), W_2 is the bottom width in the contracted section with the pier width subtracted from it (ft or m), and K_1 is a coefficient based on the shear velocity upstream. The scour depth is then given as:

$$y_s = y_2 - y_o \quad (1.3)$$

where y_s is the average contraction scour depth, and y_o is the depth in the contracted section before scour occurs (this value is approximately equal to y_1 in sand bed streams). This equation is known to often overestimate scour, but it is recommended by the FHWA (Arneson et al., 2012).

Laursen also developed a clear water contractual scour equation in 1963 (Arneson et al., 2012). The equation is as follows:

$$y_2 = \left[\frac{K_u Q^2}{D_m^{0.667} W^2} \right]^{3/7} \quad (1.4)$$

where y_2 is the average equilibrium depth in the contracted section after the scour takes place (ft or m), Q is the flow at width W (ft^3/s or m^3/s), D_m is the diameter of the smallest particle in the bed in the contracted section that will not be transported (typically estimated as $1.25 \cdot D_{50}$) (ft or m), D_{50} is the median diameter of the bed material (ft or m), W is the bottom width of the contracted section with the pier widths subtracted out (ft or m), y_o is the average depth before

scour (ft or m), K_u is a coefficient which in English units is 0.0077 and in SI units is 0.025. Scour depth can be calculated from Equation 4. This equation was found to overestimate scour if the D_{50} is less than 0.2 mm (Arneson et al., 2012).

Local scour is common along abutments and can cause bridges to fail. The three equations presented below are three commonly used equations recommended in HEC-18 by the FHWA. The first equation is the Froehlich abutment scour equation. Froehlich developed this equation from 170 live bed scour measurements in a lab (Arneson et al., 2012). The equation is as follows:

$$\frac{y_s}{y_a} = 2.27K_1K_2\left(\frac{L'}{y_a}\right)^{0.43}Fr^{0.61+L} \quad (1.5)$$

where y_a is the average depth of flow on the floodplain (ft or m), K_1 is a coefficient for abutment shape, K_2 is a coefficient for the angle of the embankment to the flow, L' is the length of the embankment that obstructs flow (ft or m), A_e is the cross-sectional area of the embankment that blocks active flow (ft^2 or m^2), Fr is the Froude number upstream of the abutment, L is the length of the embankment (ft or m).

The HIRE abutment scour equation was developed from field data on the Mississippi River and is only applicable when the ratio of embankment length to flow depth at abutment is greater than 25. The equation is as follows:

$$\frac{y_s}{y_1} = 4Fr^{0.33} \frac{K_1}{0.55K_2} \quad (1.6)$$

Where y_1 is the depth of flow at the abutment (ft or m), Fr is the Froude number adjacent to and upstream of the abutment, K_1 is a coefficient for the abutment shape, and K_2 is a coefficient for skew angle.

The third equation presented here for abutment scour is the National Cooperative Highway Research Program (NCHRP) 24-20 approach and is as follows:

$$y_s = y_{\max} - y_0 \quad (1.7)$$

$$y_{\max} = \alpha_A y_c \quad (1.8)$$

$$y_{\max} = \alpha_B y_c \quad (1.9)$$

where y_{\max} is the maximum flow depth caused by the abutment scour (ft or m), y_c is the flow depth that includes contraction scour depth (ft or m), y_s is the abutment scour depth (ft or m), y_0 is the flow depth prior to scour (ft or m), α_A is an amplification factor for live-bed conditions, and α_B is an amplification factor for clear water conditions. The advantage to this approach is that it calculates total scour from both local abutment scour and contractual scour. Whichever equation is used in design must be modified to reflect the conditions of the individual site by applying correction factors. For this reason, two dimensional models that can account for more data are needed for a more accurate estimation of pier scour depth.

1.3.2 Numerical Modeling of Bridge Scour

Bridge scour has been difficult to model due to challenges in taking measurements during flood events, the unsteady nature of scour-forming events, and variability of streams and bridges. The Federal Highway Administration (FHWA) suggested using two-dimensional models for all bridge crossings except for the simplest of cases (Arneson et al., 2012). In two-dimensional models some of these issues can be minimized because it is possible to have more inputs. For this reason, two-dimensional models are more complex than one-dimensional models or empirical equations and can be more accurate for scour modeling.

Scour typically occurs during storm events because discharge is greater and can move sediment more easily. North Carolina is prone to storm surges from tropical storms due to its protruding coastline. According to Froehlich and Fisher (2000), tropical storms and hurricanes make landfall in North Carolina once every four years on average; however, this number has

most likely increased in recent years. In the study by Froehlich and Fisher (2000), six bridges in Bogue Sound, North Carolina were input into the Finite Element Surface-Water Modeling System (FESWMS) to model the effect of a past hurricane. The primary cause of flooding was determined to be a wind-driven tidal surge. The results of the study concluded that unsteady flow, i.e. tidal surges, need to be considered when modeling bridge scour (Froehlich and Fisher, 2000).

When simulating scour, it is common to use one peak flow from the storm to estimate the maximum scour depth. Chang et al. (2004) argued that using a single peak flow discharge overestimated the maximum scour depth. Instead, they recommended using a stepwise hydrograph to represent unsteady flow during storms. This approach could be applied when modeling bridge scour in any stream, but it is especially a concern in coastal settings.

HEC-RAS

The Hydrologic Engineering Center River Analysis System (HEC-RAS) was developed by the US Army Corps of Engineers (USACE). The two-dimensional version of HEC-RAS, Version 5.0, was released in 2016 (Brunner, 2016). This version, and subsequent versions, allowed the user to perform one-dimensional, two-dimensional, or a combined approach to any modeling case. In two-dimensional analysis, the study area is divided into polygons that make up a mesh. Each polygon can be characterized individually with such properties as the Manning's roughness or land use (Brunner, 2016). This model can use either the Saint Venant or Diffusion Wave equations to analyze two-dimensional flow. The main limitations to HEC-RAS in the context of bridge scour are that the two-dimensional versions do not have sediment transport or bridge modeling capabilities currently (Brunner, 2016). These functions can be run in the one-

dimensional version, but many studies suggest that for such a complex issue a two-dimensional model has the ability of being more accurate.

SRH-2D

The US Bureau of Reclamation developed the Sedimentation and River Hydraulics two-dimensional model (SRH-2D). The latest version (SRH-2D v3) released in 2019 includes mobile-bed sediment transport capabilities (U.S. Bureau of Reclamation, 2019). Like HEC-RAS 2D, this model uses the St. Venant equations to perform flow analysis. SRH-2D has many of the same capabilities as HEC-RAS 2D, but one difference is SRH-2D allows for a more detailed mesh to be drawn with the addition of quadrilateral mesh elements as well as triangular elements. The sediment transport in two dimensions is also a key difference, especially for a scour study. This feature allows the user to model non-uniform sediment, variable loads, bedrock erosion, and cohesive versus non-cohesive sediments (U.S. Bureau of Reclamation, 2019).

1.3.3 Distributed Temperature Sensing Background

The main advantage of using fiber optics Distributed Temperature Sensing is that real time scour data can be collected, so the maximum scour depth can be determined rather than the equilibrium scour. Unlike TDR, they are small and lightweight, they have high temperature resistance, and they are flexible and stable even in harsh environments (Lin et al., 2005). DTS have been used in several hydrologic experiments, but there are many considerations to account for when deciding if it is acceptable for certain applications.

The Raman scattering method was chosen as the ideal FO-DTS method for this thesis. The measurement principles of this method are based on quantifying, at two specific frequencies, the intensity of Raman based scattered light from which, in combination with the use of optical

time domain reflectometry principles, temperatures can be determined at different positions along the fiber (Sayde et al., 2010).

The ratio between the amount of light that travels above the original frequency and the amount that travels below the original is exponentially dependent on temperature (Selker et al., 2006). To calculate temperature, the backscattered light's return period is recorded by the DTS, and Raman scattering principles are applied (Dakin et al., 1985). The position along the cable can then be inferred by knowing the travel time and the speed of light (Tyler et al., 2009).

There are two common methods for collecting temperature data using a DTS system, the single ended and the double ended methods. The single ended method calculates temperature from light transmitting in only one direction along the cable (Tyler et al., 2009). The advantage is that it is easier to implement as access to only one end of the FO cable is needed. In this method, the highest temperature precision is achievable near the measuring device. The precision decreases exponentially as the measurement location along the cable gets further from the device. In the second method, double-ended measurement, both ends of the FO cable are connected to the DTS instrument and measurements are collected from both ends (Tyler et al., 2009). The advantage to this method is that it is easier to calibrate as scattered light losses along the cable can be accounted for in the calibration. The disadvantage of this method is that it adds complexity to the system configuration as access to both ends of the cable is needed. It also reduces the measurements temporal resolutions by half as each double ended temperature product is inferred from two single ended measurements. The double-ended method is preferred when the same level of precision is needed along the cable or when step-loss light attenuation is observed at discreet locations along the FO cable. Note that, calibration of each FO cable is also

typically needed before any data collection begins because the DTS and FO sensing cable performance characteristics can differ from what the manufacturers listed (Tyler et al., 2009).

1.3.4 FO-DTS Applications in Environmental Research

The use of FO-DTS in environmental research has been growing in the past two decades. This is mainly due to the high spatial resolution measurements that FO-DTS provides compared to other methods where data are collected at the point scale. DTS can record temperatures with 0.01 °C resolution every 0.125 m for distances of up to 10,000 m (Cheng et al., 2017). For instance, Sayde et al. (2015) used an energy balance approach to calculate fluid velocity from DTS data of a heated FO sensing cable. The FO-DTS system was able to report wind velocity every 0.25 m, every 5 s, at three elevations along a 240 m transect.

Sebok et al. (2015) were interested in locating areas where groundwater discharged into streams using the thermal signal of groundwater inflow. One challenge they faced was that in fast-moving streams the heat inflow with groundwater dissipated quickly over short distances. Their solution was to use a looped DTS system to increase the measurements' spatial resolution to monitor the heat flux. Scouring was difficult to determine based on temperature readings alone because the anomalies were only consistent in December when there was maximum scour. After discarding the established sedimentation sites, high-discharge sites were identified using the warm temperature anomalies. The location of high-discharge zones migrated downstream over time (Sebok et al., 2015).

Zhang and Zhao (2018) conducted an experiment with Raman scattering FO-DTS to evaluate the accuracy of measuring underwater pipeline scour. In their experiments, a large bucket was filled with sand and water at known depths then an armored FO cable was placed in the bucket.

The main difference between their study and the lab study presented in this thesis was that the water in their tests was not flowing.

Dong et al. (2016) measured soil moisture with FO-DTS. They concluded that soil water content can be inferred at high spatial resolution from DTS passive measurements. In their application, soil water content was inferred by observing the propagation of the diurnal temperature signal through the soil profile. Sayde et al. (2010) also measured soil moisture. The conclusion of Sayde et al. (2010) was that soil moisture content can be inferred from actively heated DTS measurements. In this application, the thermal conductivity of the soil is inferred by observing the heat dissipation from electrically heated FO cable. Then soil water content was calculated from the measured thermal conductivity by employing soil specific relationships relating thermal conductivity to soil water content.

CHAPTER 2: FO-DTS EXPERIMENTS

2.1 Introduction

Bridge scour is the leading cause of bridge failure in the United States (Deng and Cai, 2009). Better understanding of scour formation will require monitoring accurate tracking of scour formation in real-time. To date, there is a lack of scour monitoring techniques that allow to monitor scour formation at high temporal and spatial resolution. Most techniques currently being used are either deployed before and after a scour event rather than during the storm or are not very durable. Because of these limitations, a durable new device to measure and monitor scour in real time has been developed. The specific objective of this chapter is to develop and test a FO-DTS scour monitoring device capable of tracking changes in the sediment-water interface at high spatial and temporal resolutions.

Fiber-optics distributed temperature sensing (FO-DTS) has the potential of measuring scour with high temporal and spatial resolution. FO-DTS can record temperatures of 0.01 °C resolution every meter for distances of up to 10,000 m (Cheng et al., 2017). By examining the changes in temperature, the sediment to water interface i.e., bed location can be determined because the rate of the processes controlling heat exchanges between the FO cable and its surroundings are different in the sediment than it is in running water due to conductive versus convective cooling. The water to air interfaces i.e., water depth can also be measured by this method. This innovative monitoring technique may lead to a better understanding of scour hole dynamics and processes that will then allow for a safer design of bridges.

2.2 Methods

2.2.1 Flume Description

In order to test the performance of the FO-DTS scour monitoring devices under varying flow and sediment depth conditions, an experimental flume was constructed. The 2.4 m long by 0.2 m wide by 0.6 m tall flume was used for all laboratory testing of the device in this research (Figure 2-1). The flume's design was inspired by a small stratification flume (Rouhnia, 2016). Water was pumped out of a reservoir and into the inlet chamber of the flume through a series of PVC pipes and valves. Water then filled the inlet box before flowing over an L-shaped divider into the testing section of the flume. Dividers that were 7.6 cm tall were stacked on top of each other to adjust the height of sediment in the testing section. Water then flowed through the testing section and to the outlet chamber. The water drained through a hose to a small pool and was pumped back to the reservoir to recirculate water. A flow meter was installed in the PVC pipes coming into the inlet box, so a stage-discharge relationship could be made for the flume. Stage was measured by recording the depth of water over the L-shaped divider flowing into the testing section.



Figure 2-1. Photograph of the flume used to test the FO-DTS prototype performance.

2.2.2 FO Device Description

Two prototypes of the FO-DTS scour monitoring device was constructed to test the FO-DTS's ability to locate and track the sediment-water interface. The first prototype (Prototype 1) has a diameter of 50.8 mm and a height of 0.6 m. The prototype was constructed by wrapping a FO cable around a 5 cm diameter PVC pipe. A 20 AWG heating cable sheathed in silver plated copper, with an outer diameter of 0.058 in, was wrapped on top of the FO cable (Remington Industries, USA) (Figure 2-2). The FO cable chosen for this device had an outer diameter of 0.9 mm and contained a multi-mode optical fiber without a heating element. To be able to perform an active heating test, the heating cable was then wrapped on top of the FO cable.



Figure 2-2. Prototype 1 was constructed by wrapping a FO cable around a 5 cm diameter pipe.

The total length of the wrapped section is 60 cm.

The second device (Prototype 2) (Figure 2-3) was constructed by wrapping a FO cable around a 5 cm diameter PVC pipe. The cable chosen was the BRUsens® (Brugg cables,

Switzerland) FO cable which consists of an inner multimode FO filament as well as stainless steel wires that can act as a heating element (Figure 2-4). The wrapped section of cable was 30 cm tall, along the PVC pipe. The second device was placed in the sand in the same manner as the first device and the calibration bath temperatures were also the same.

In each test of the device, it was placed vertically in the flume, so that part of it was buried under sand (D_{50} of 0.15 mm), part of it was exposed directly to water, and another section was only exposed to the air. The FO cable that was wrapped around the device was also connected to a DTS machine and coiled in two calibration baths. One calibration bath was kept at room temperature water and the other had a 0°C ice-water slurry mix. Two different DTS machines were used for these experiments. The Silixa Ultima ® (Silixa Ltd, UK) with a sampling resolution of 0.125 m every 1 second and a spatial resolution of 0.25 m was used in the testing of prototype 1. Prototype 1 had a vertical resolution of 1.92 m for every 1 cm vertically along the device. The Silixa XT ® (Silixa Ltd, UK) with a sampling resolution of 0.25 m every 5 seconds, a spatial resolution of 0.5 m every 5 seconds was used for prototype 2. Prototype 2 had a vertical resolution of 0.54 m for every 1 cm vertically along the device.

To achieve active heating of the FO cable, a copper wire attached to the BK Precision 9205 600W DC power supply was spliced to the device at both ends (B&K Precision Corp., USA). For each test, the power supply heated the cable with approximately 60 V and 7 A for two to five minutes. These values were the maximum power that could be supplied in the experimental setup without tripping the power supply or pumps in the flume.

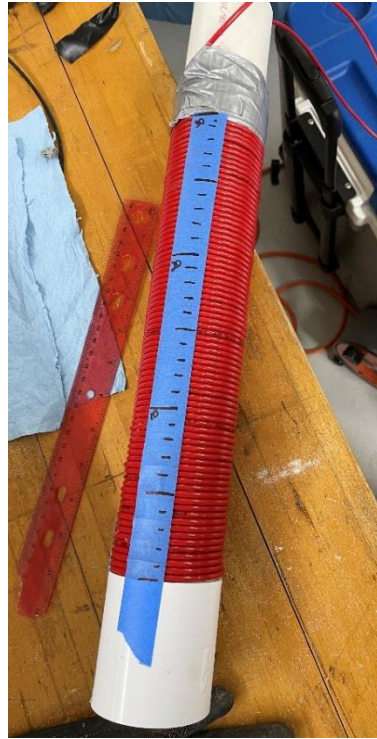


Figure 2-3. Prototype 2 was constructed by wrapping a FO cable around a 5 cm diameter pipe.

The total length of the wrapped section is 30 cm.

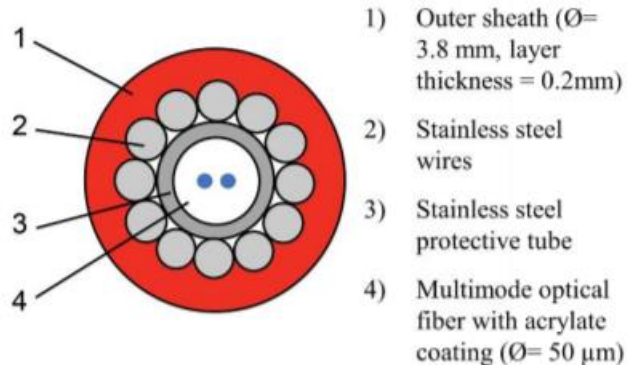


Figure 2-4. A cross-sectional view of the BRUsens FO cable. Adapted from DeBell, 2021.

2.2.3 Experiment Design

During the first tests of Prototype 1, no scour was created, and the prototype was used to capture the static sand-water interface at three different flow velocities. The average velocities

were 2.7 cm/s (hereafter high flow), 0.59 cm/s (hereafter low flow), and standing water (hereafter zero flow). In the subsequent tests, scour was simulated by pulling the device out of the sand bed. The latter tests were performed to track changes in the location of the sediment-water interface and to determine if these changes could be captured by the device.

Prototype 2 was tested under various conditions in the flume ranging from zero to high flow and static and dynamic scour. Flow was adjusted using the series of valves controlling the flow into the flume. In the static scour tests, the initial flow of water coming into the flume created erosion around the device, but the bed level stayed relatively constant during the remainder of the experiment. During the dynamic scour tests, scour was created by reducing the height of the flume's downstream barrier to reduce stage thus increasing the water velocity in the flume. Before the start of each experiment, the bed was smoothed and leveled to be the same in each run and the water was run through the flume for at least 30 minutes to reach thermal and hydraulic equilibrium.

An algorithm created in Matlab (MathWorks, 2020) to automatically identify the change of location of the air-water and sediment-water interface was developed to facilitate laboratory and field data processing from the FO-DTS scour monitoring devices. The code uses the recorded temperature gradient along the FO-DTS device to detect the interfaces as follows: (a) calculate the gradient of the observed temperature profile; (b) find the locations of the maximum and minimum temperature gradients; (c) find the extents of the search zones, which are bounded by the location of the maximum/minimum temperature gradients and the first surrounding location at which the temperature gradient returned to its original pattern observed in the sediment; (d) return to which corresponds to a gradient of unity (similar to that observed in the

air); and (e) identify the interfaces as the locations within the search zones that have a temperature gradient similar to the average temperature gradient in the search zones.

2.2.4 Field Installation

A field setup at the bridge crossing of Glenn Rd over Ellerbe Creek in Durham, NC was installed in late November 2021. The field devices have the same design and material as prototype 2 but with a larger sensing length of 90 cm. In the setup, the devices were connected to another PVC pipe that did not have any cable wrapped around it and that pipe was secured to the pier using super struts and ratchet straps (Figure 2-5). Just like in the lab setup, the device was partially buried in the sediment and the rest was under water on the day of the installation. Ideally, one device would be on each pier, but due to the large amount of debris on the upstream pier both devices were placed on the downstream pier. The devices were electrically connected in parallel and both the FO cable and a 12-gauge 150 ft electric cable were suspended over the stream and attached to a metal rod on the left bank.



Figure 2-5. The field setup of the two devices at Ellerbe Creek in Durham, NC.

2.3 Results and Discussion

2.3.1 Prototype 1 Results

A total of four experiments were conducted to evaluate prototype 1. The high, low, and zero flow tests were all static scour tests i.e., the bed level remained constant throughout each test and there was no visible sediment transport taking place around the prototype itself. In the scour-inducing test, the bed level itself did not change, but the placement of the prototype in the sediment did change, so that the bed was at a different location along the device. Because it was assumed that the bed level remained constant throughout the experiments, the sand-water interface was only measured once during the first three tests and then measured once after the prototype was pulled out of the sand. Unfortunately, the water-air interface was never measured during these experiments, so those comparisons cannot be made.

In the no flow test, water was ponded in the flume while the cable was heated to determine if even under no flow conditions the sediment-water interface could be accurately detected FO-DTS. The results after five minutes of heating can be seen in Figure 2-6.

The error of the interfaces at various heating times were also analyzed to determine if heating time had an impact on the result and to identify the minimum heating time needed to accurately detect the location of the interface (Figure 2-7). The analysis results showed that error in locating the interface decreased as time progressed and stabilized between 500 and 800 seconds after the heating started..

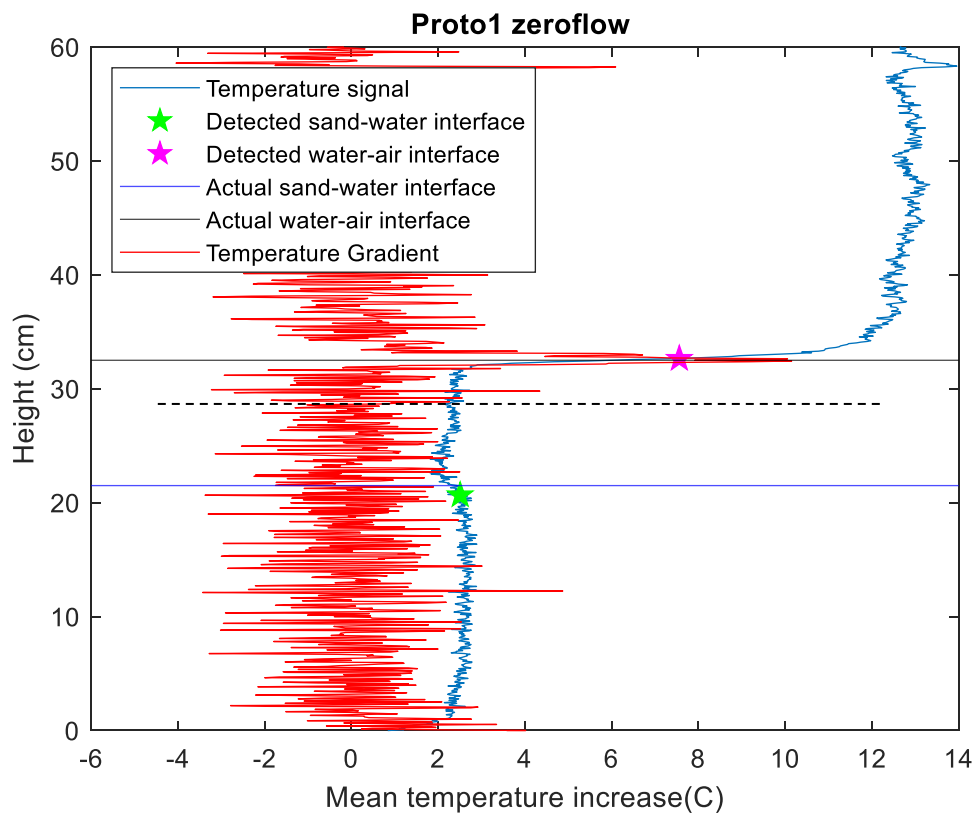


Figure 2-6. The results of the zero-flow condition for prototype 1. The x-axis represents both the mean temperature increase (blue line) and the temperature gradient (red line) observed along the cable while the y-axis is the vertical distance along the prototype. The vertical distance of zero represents the bottom of the prototype which was fully buried under sediment. The green star represents the calculated sediment-water interface, and the pink star marks the calculated water-air interface. The horizontal blue and black lines represent the location of the independently measured sand-water and water-air interfaces respectively.

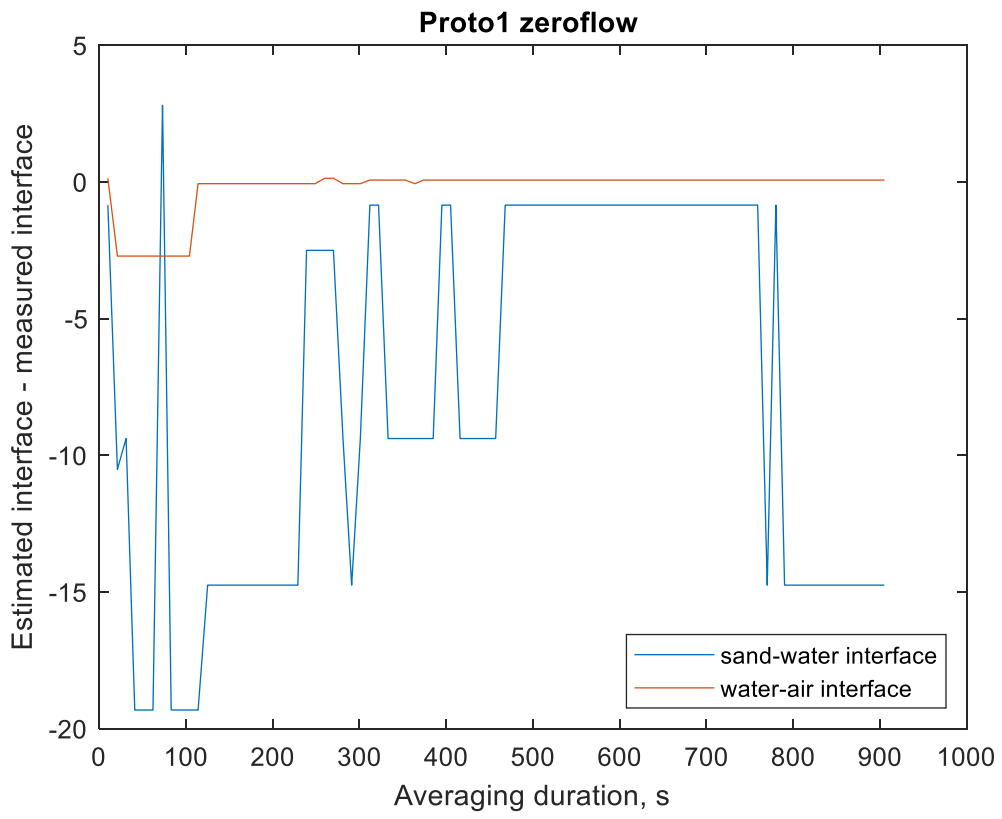


Figure 2-7. Error of interface locations versus heating duration under zero flow for prototype 1.

Figure 2-8 contains the results after five minutes of heating for the low flow condition for prototype 1. In this condition, water flowed through the flume, but no scour was observed near the device. Similar to the zero-flow condition, the error in locating the interface decreased as heating time increased (Figure 2-9) and stabilized after 300 seconds.

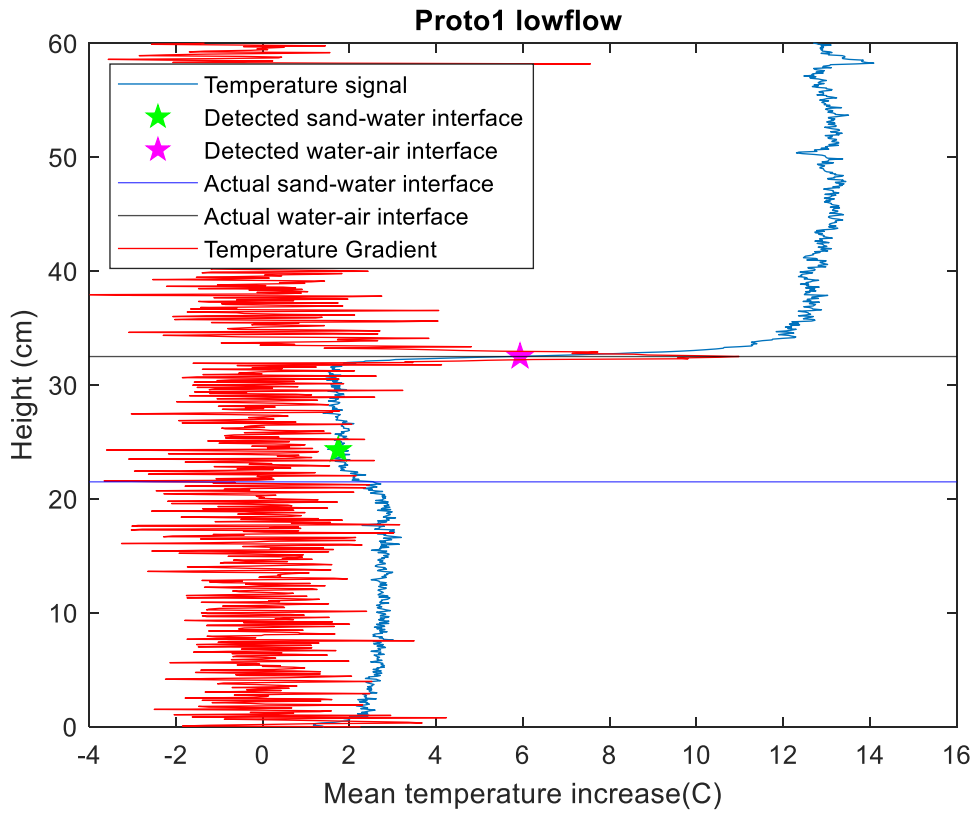


Figure 2-8. The results of the low flow condition for prototype 1. The x-axis represents both the mean temperature increase (blue line) and the temperature gradient (red line) observed along the cable while the y-axis is the vertical distance along the prototype. The vertical distance of zero represents the bottom of the prototype which was fully buried under sediment. The green star represents the calculated sediment-water interface, and the pink star marks the calculated water-air interface. The horizontal blue and black lines represent the location of the independently measured sand-water and water-air interfaces respectively.

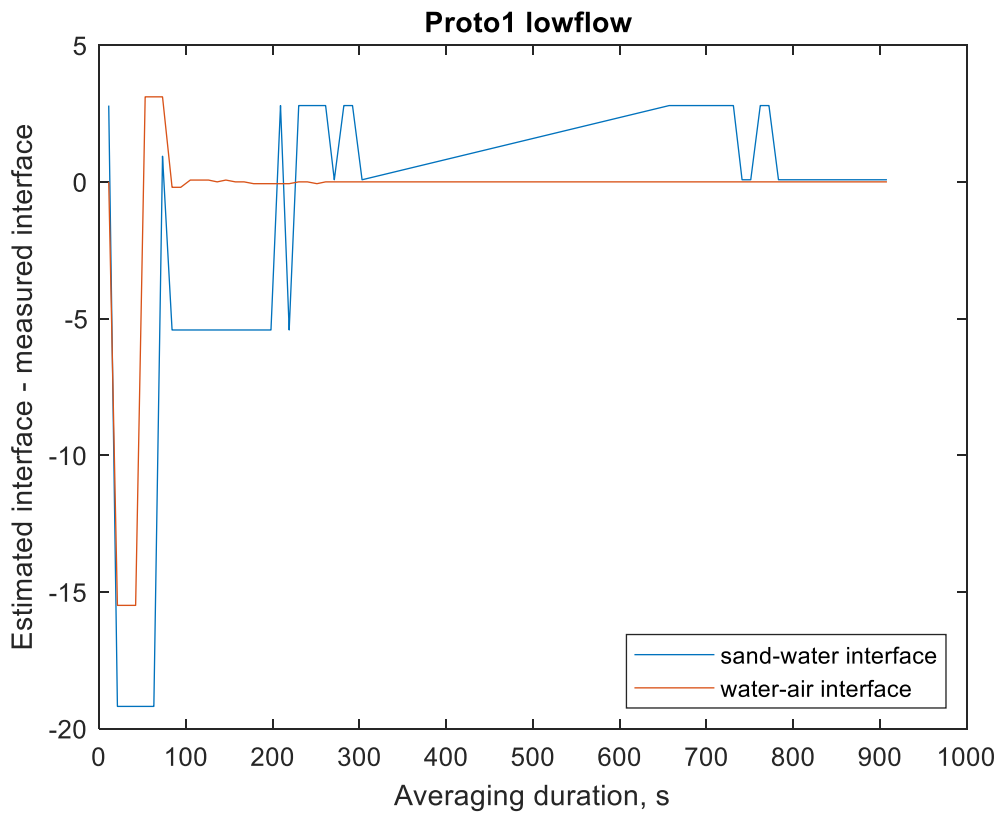


Figure 2-9. The error of interface locations versus heating time under low flow for prototype 1.

In the high flow condition, once again no scour was created around the device. The results after five minutes of heating can be seen in figure 2-10. The error over heating duration was also evaluated (Figure 2-11). The error stabilized around 300 seconds after the start of heating.

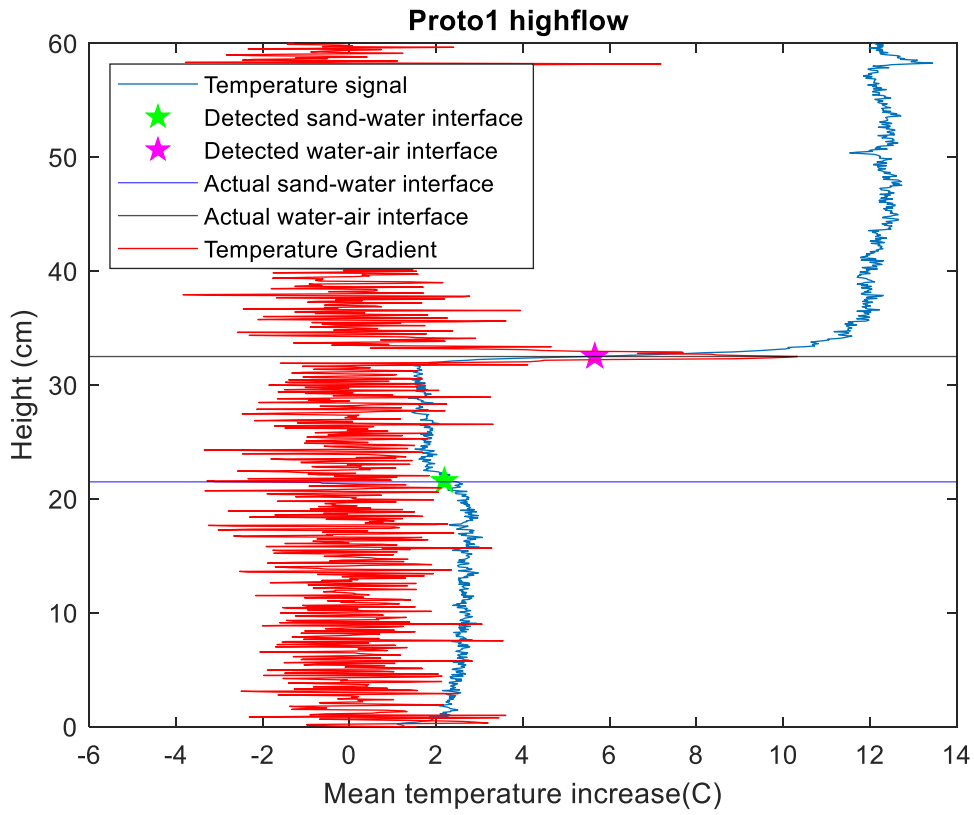


Figure 2-10. The results of the high flow condition for prototype 1. The x-axis represents both the mean temperature increase (blue line) and the temperature gradient (red line) observed along the cable while the y-axis is the vertical distance along the prototype. The vertical distance of zero represents the bottom of the prototype which was fully buried under sediment. The green star represents the calculated sediment-water interface, and the pink star marks the calculated water-air interface. The horizontal blue and black lines represent the location of the independently measured sand-water and water-air interfaces respectively.

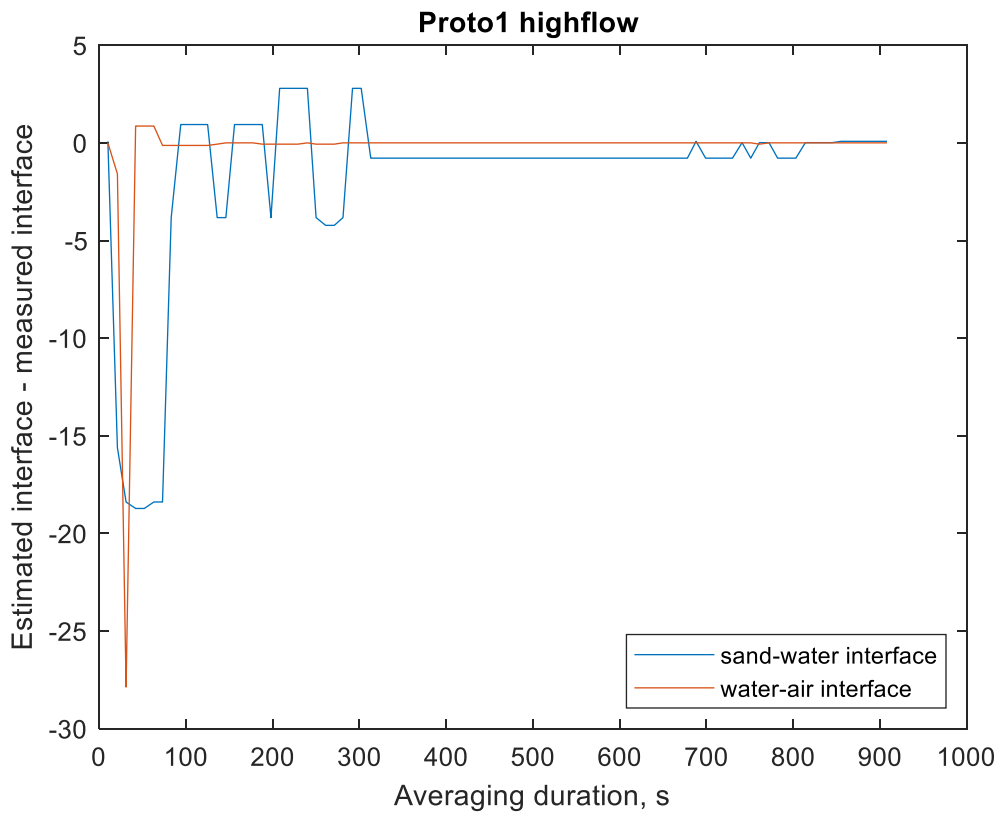


Figure 2-11. The error of interface locations versus heating duration under high flow for prototype 1.

The last test of prototype 1 was a scour-inducing experiment in which the prototype was vertically raised 5 cm to represent scour taking place around the device. Figure 2-12 contains the interfaces calculated before the device was pulled out of the sediment (top) and after the “scour” was simulated (bottom). Note that the sediment-water interface in the before image was located at 21 cm and after the device was raised 5 cm the interface was located at 16 cm, a difference of 5 cm. The error of sediment interface location versus heating time could not be calculated for in this experiment because of the way the device was pulled out of the sediment.

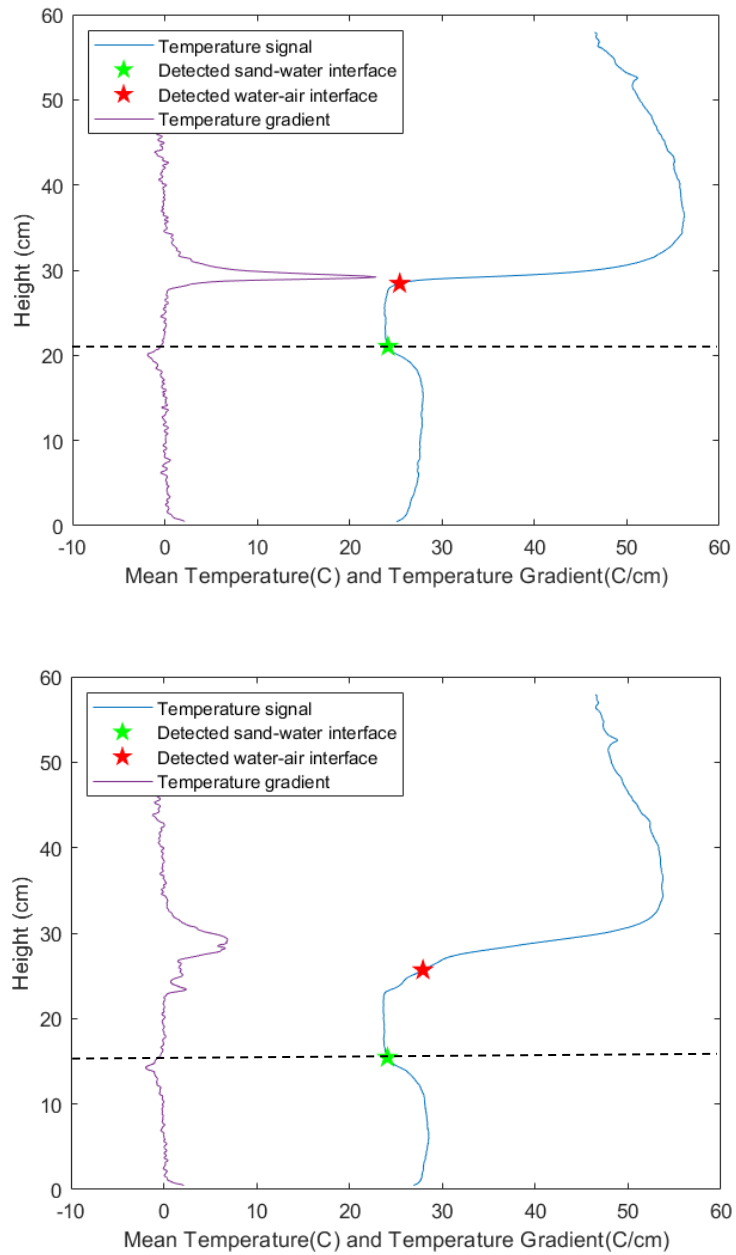


Figure 2-12. The before and after plots of the sediment-water and water-air interfaces in the scour-inducing experiment.

The average error across all tests in identifying the sediment-water interface was 1 cm and the average time needed to accurately locate the interface was about 340 seconds.

2.3.2 Prototype 2 Results

A series of nine total tests were performed to evaluate prototype 2 with three tests being from each condition (no flow, medium flow, and maximum flow). Water temperature was recorded in each of the tests and remained constant at 21°C. Both the no flow and medium flow conditions were static scour tests. Meaning that once scour was initially created around the device, there was no following evolution of the scour hole. In the maximum flow tests, however; the height of the downstream barrier was removed as mentioned previously to increase velocity thus creating dynamic scour.

In the no flow tests, water was ponded at a depth of 9 cm above the sand (Figure 2-13). Error can be explained by two factors: (a) measurement errors; (b) the vertical resolution of the prototype. Note that the algorithm used to detect the location of the interfaces has not been calibrated. Further refinement and calibration of the algorithm is expected to reduce this error. As with prototype 1, the error over heating time was analyzed for all tests of prototype 2. The error stabilized around 100 seconds of heating time (figure 2-14).

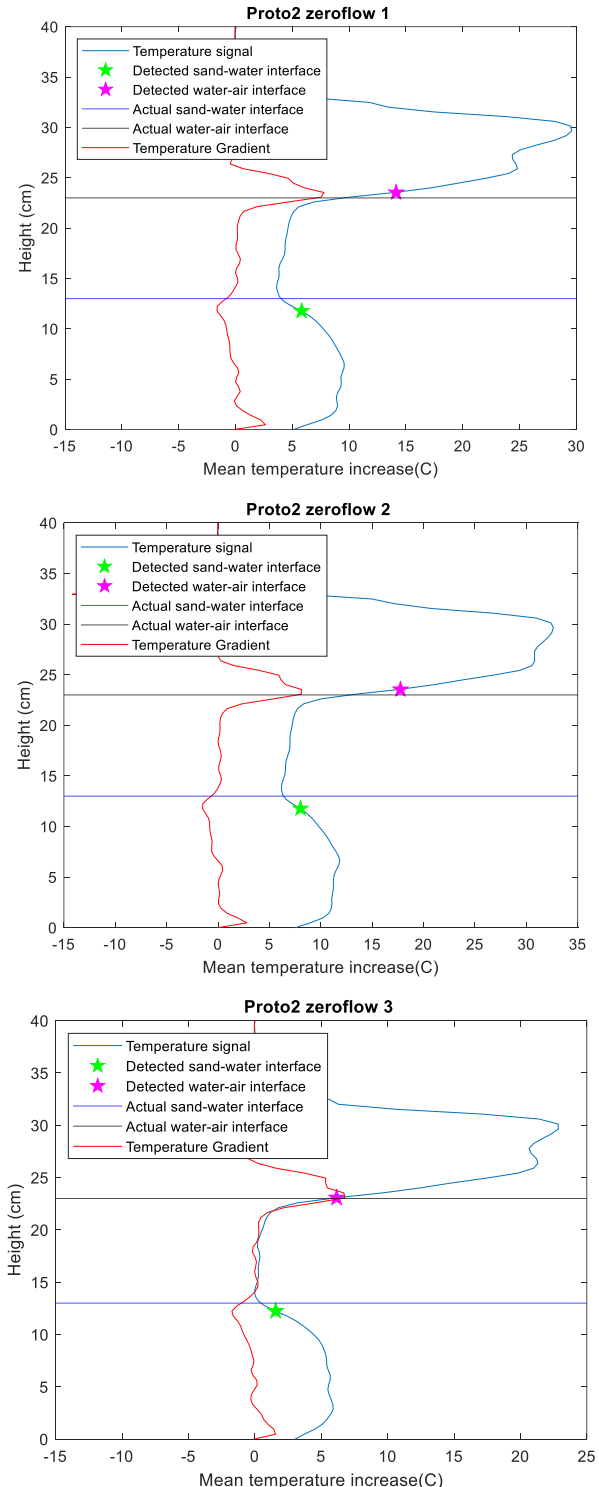


Figure 2-13. The results from the no flow tests. The x-axis is the mean temperature increase and the temperature gradient, and the y-axis is the height of the device in centimeters. The green star represents the sand and water interface. The pink star represented the water-air interface, and the difference between the two stars was the water depth.

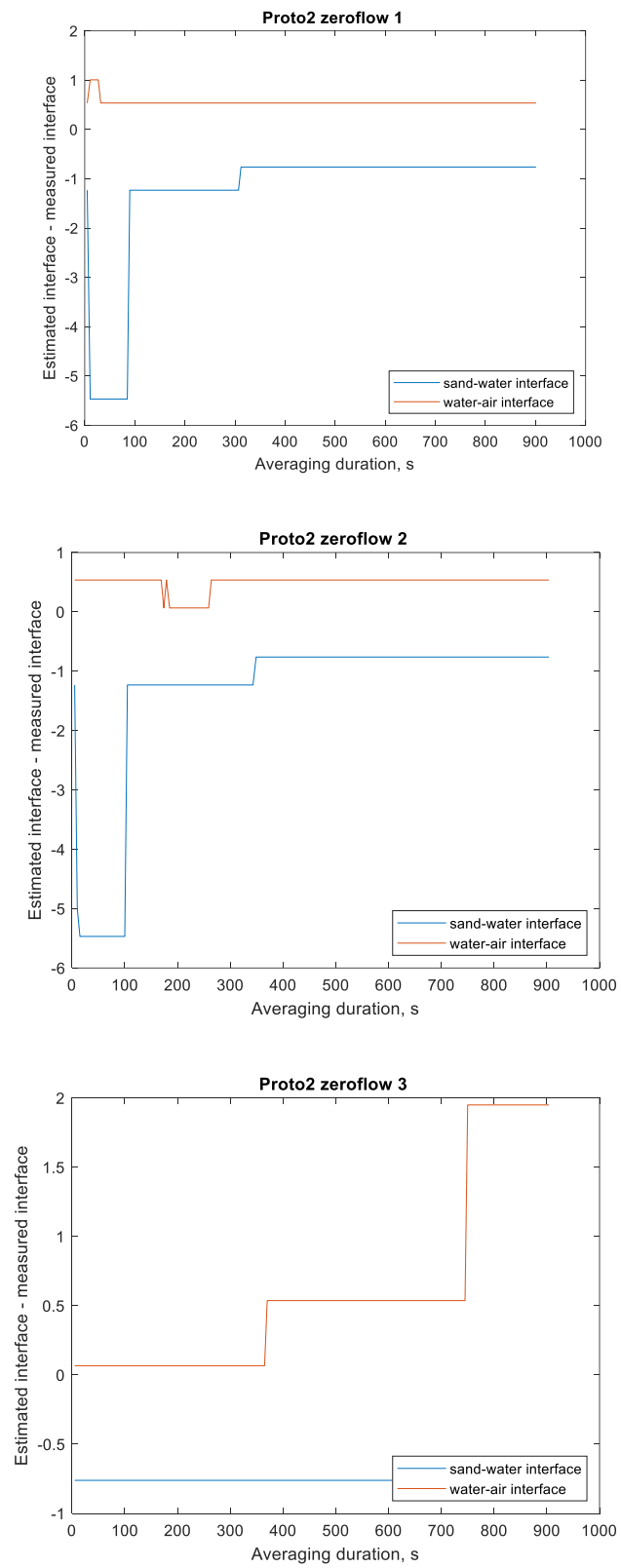


Figure 2-14. The error versus heating time increments for the no flow tests.

The results of the medium flow tests can be seen in Figure 2-15. During these experiments, the velocity ranged from 2.36 cm/s to 3.15 cm/s. These results are similar to the no flow condition in regard to location of the interfaces. The sand-water interface was more clearly defined in this figure because of the greater temperature difference. The error in each test seemed to converge after 100 seconds of heating time (Figure 2-16).

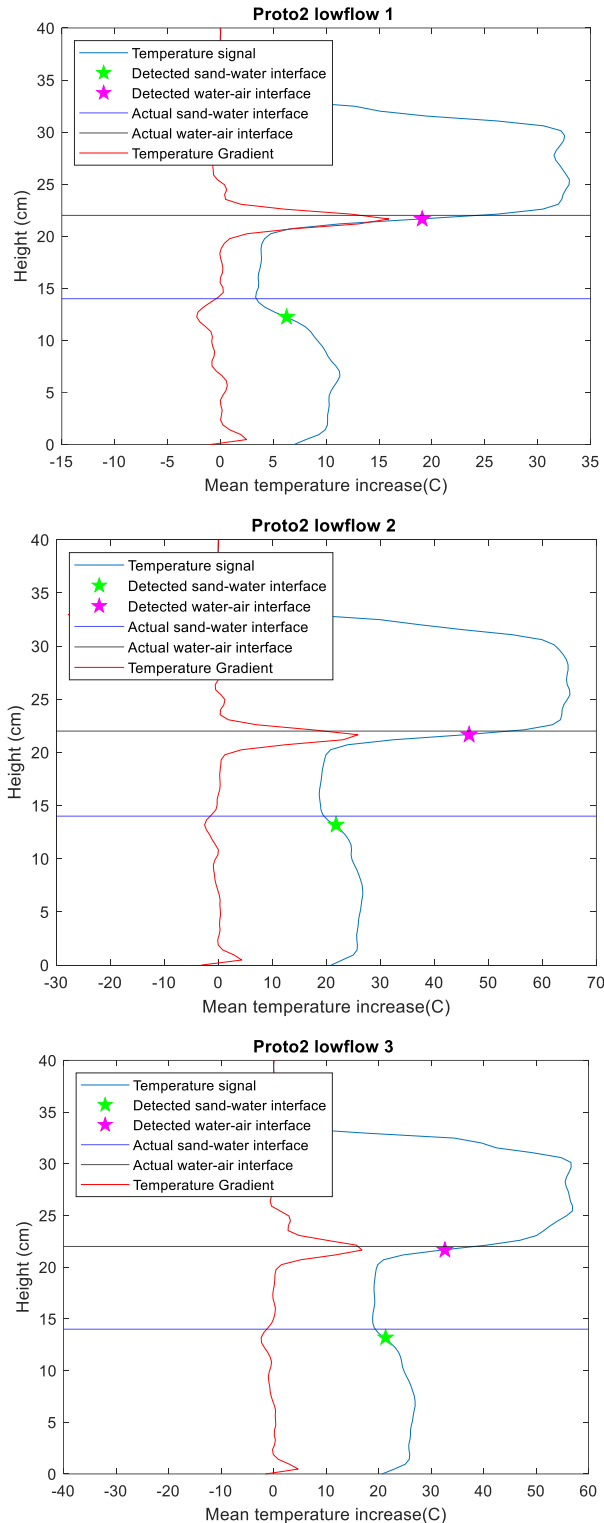


Figure 2-15. The results from the medium flow tests. The x-axis is the mean temperature increase and the temperature gradient, and the y-axis is the height of the device in centimeters. The green star represents the sand and water interface. The pink star represented the water-air interface, and the difference between the two stars was the water depth.

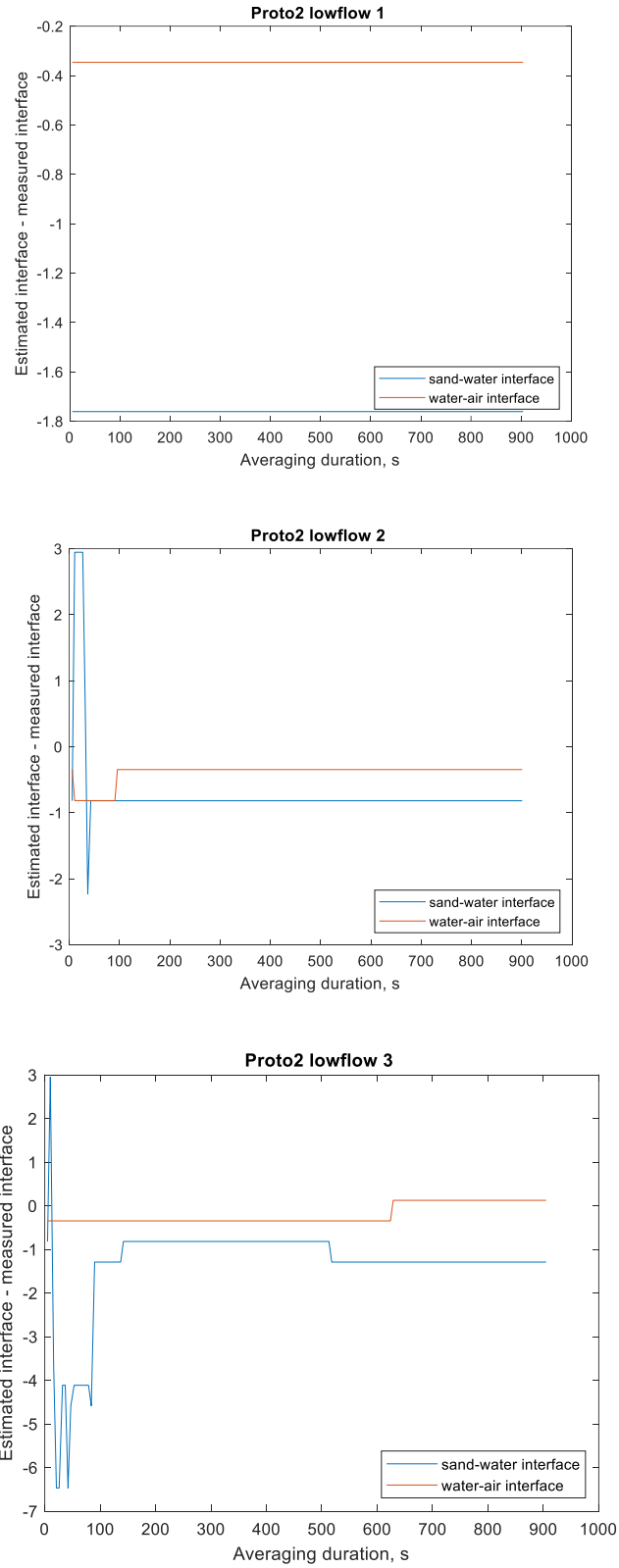


Figure 2-16. The error versus heating time duration for the medium flow tests.

The results of the maximum flow test can be seen in Figure 2-17. During these experiments, the velocity ranged from 8.85 cm/s to 15.92 cm/s. These results vary from the other conditions in that the scour hole did grow with respect to time and the water depth was much shallower.

These tests most likely had the most variables changing between tests, resulting in greater differences between the observed and measured interfaces, e.g., the flow was producing scour around the device during the test, and this scour formation could have been different in each test. Additionally, between each test the bed was smoothed, but it might have still had irregularities which could have impacted the measurements. The greater error occurred at the time intervals less than one minute. This indicates that a heating time of less than one minute is not adequate for capturing the sand-water interface.

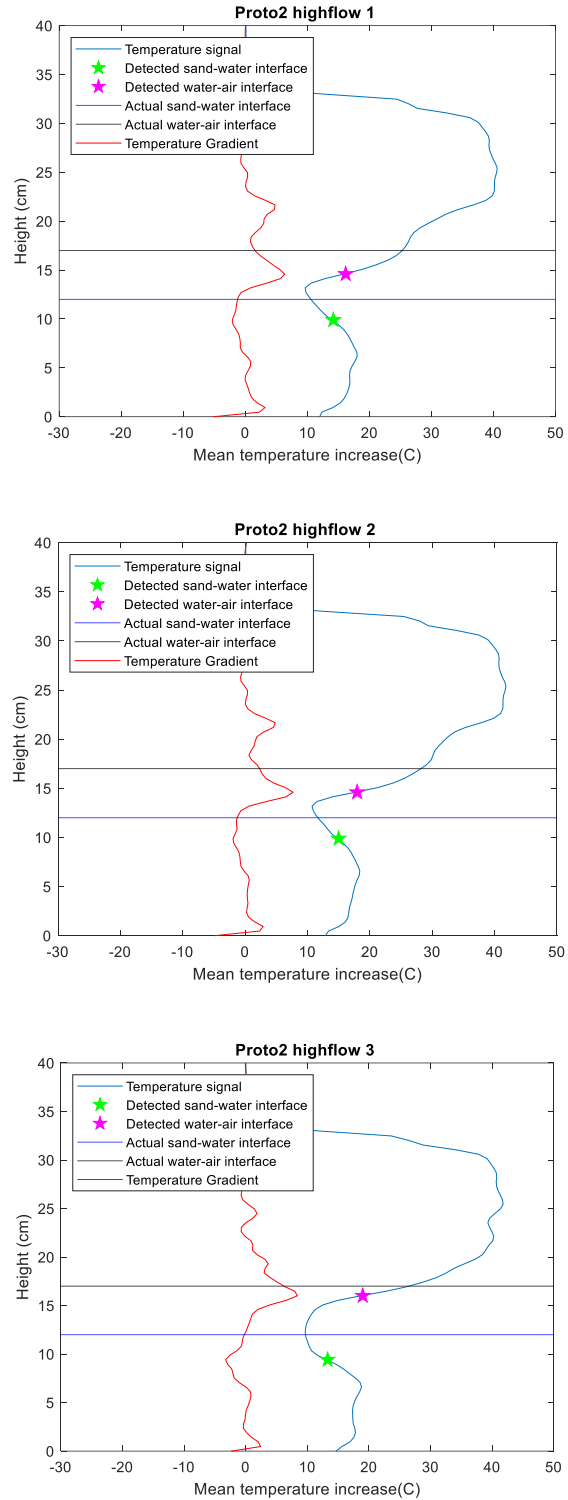


Figure 2-17. The results from the maximum flow tests. The x-axis is the mean temperature increase and the temperature gradient, and the y-axis is the height of the device in centimeters. The green star represents the sand and water interface. The pink star represented the water-air interface, and the difference between the two stars was the water depth.

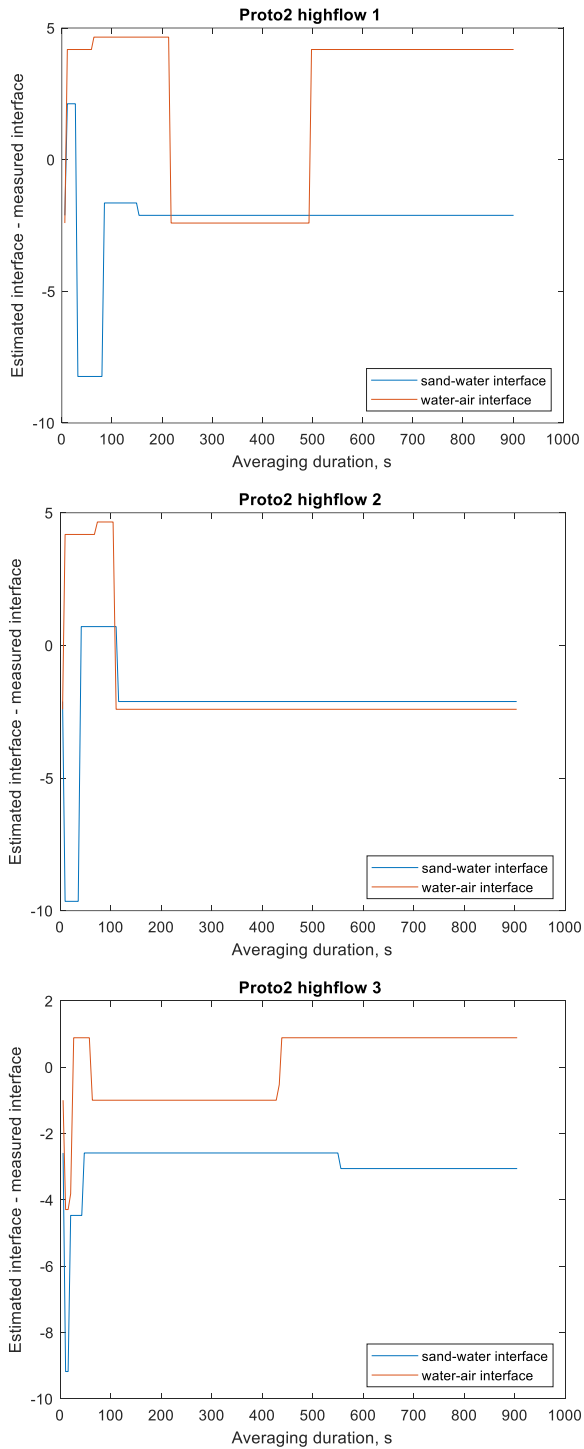


Figure 2-18. The error versus heating time increments for the maximum flow tests.

The two major differences between Prototype 1 and Prototype 2 design are the density of vertical measurements and how heating was applied relatively to the location of the sensing cable. Those two major differences can explain the difference in performance observed between

the two prototypes, i.e., the lower error value in detecting the water-sand interface location for prototype 1 and the faster response time in detecting the interface for prototype 2. In prototype 1, the combination of a higher resolution DTS unit and the use of a thinner FO cable, that can be more densely wrapped around the PVC core structure of the prototype, has resulted in higher vertical resolution of temperature measurements along the prototype i.e. 0.126 cm for prototype 1 compared to the 1 cm resolution for prototype 2. From the other hand, the temperature sensing optical fiber in the FO cable of prototype 2 was in quasi direct contact and incased in the heating element. In contrast, the optical fiber in prototype 2 was separated by layers of thermally insulated material which created attenuation in the magnitude and lag in the arrival of the heating signal which resulted in a longer heating duration requirement to accurately locate the interfaces.

2.3.3 Field Installation Results

Preliminary results from the field tests performed on November 30, 2021, at Ellerbe Creek have been analyzed. The time of active heating for each test was 5 minutes and the total amount of current was 10 amps, and the devices were connected in parallel.

Results have been gathered from both device 1 and device 2. Device 1 was on the left side of the pier while device 2 was directly on the downstream side of the pier. The water-air interface was not calculated because both devices were entirely submerged in water.

Figure 2-19 shows the results of device 1. The blue line is the temperature signal, the yellow line is the temperature gradient, the dashed black line is the field-measured sand-water interface, and the green star is the algorithm-calculated sand-water interface. The error between these two values ranged from 1-2 cm, which is consistent with the laboratory experiments for prototype 2.

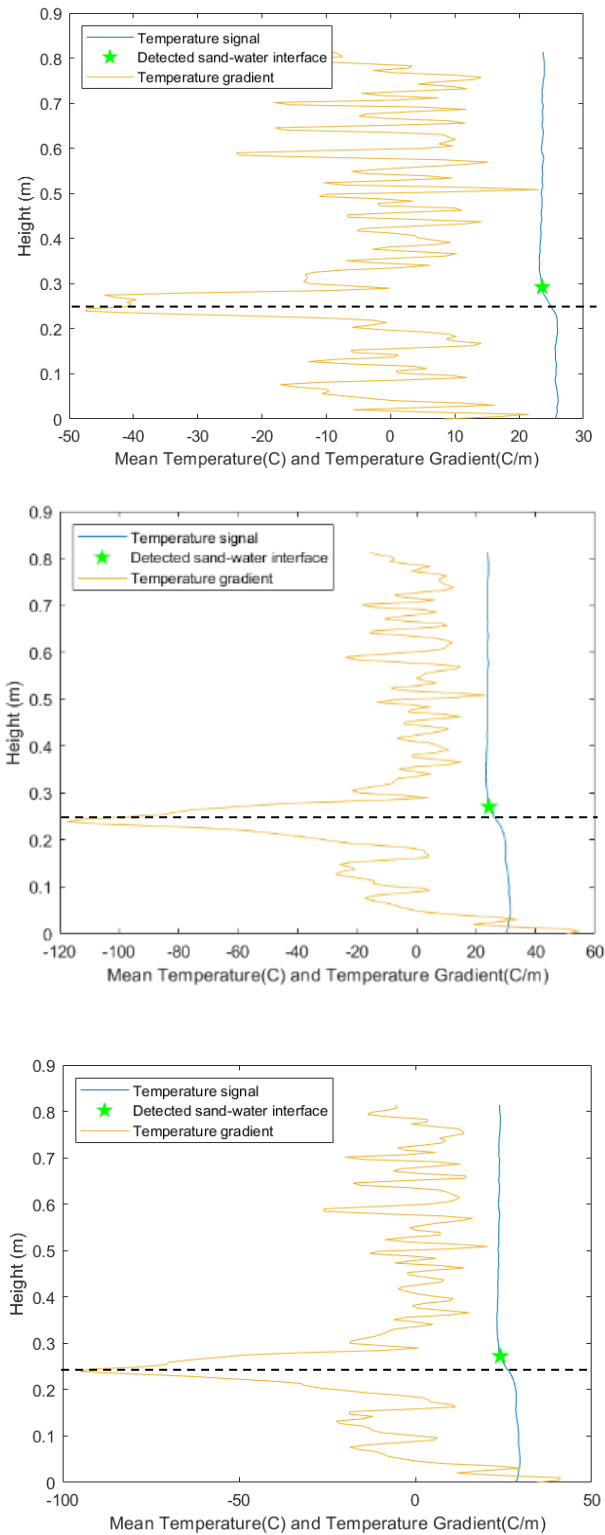


Figure 2-19. The results from the first device in the field installation. The green star represents the detected sediment-water interface while the red represents the water-air interface.

The results of the second device from the same time are in figure 2-20. Only two of the three heat pulses are shown below due to an incomplete dataset for the first test on device 2. This meant that the algorithm was not able to solve for the selected interfaces. However, between the remaining two tests the results are consistent. The error was 1 cm for these tests, which again is consistent with the laboratory experiments of prototype 2.

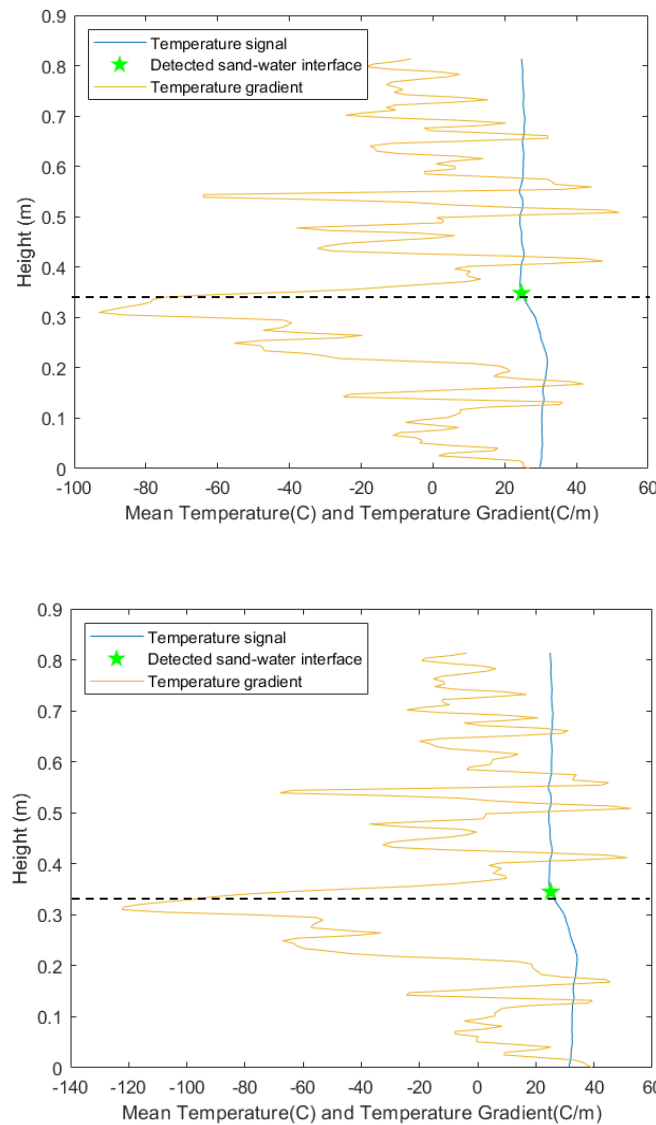


Figure 2-20. The results from the second device in the field installation.

2.4 Conclusions

In this thesis, two prototypes were tested in the lab and eventually one of those was tested in the field. The advantage of prototype 1 when compared to prototype 2 was that it had increased vertical resolution in detecting the water-sediment interface. The construction of the device was more laboring and because the heating cable was wrapped on top of the FO cable there is more chance of the FO-cable being distorted. Additionally, because the heating cable was wrapped above the FO-cable, the response time of heating was longer. For this reason, more frequent measurements can be achieved with prototype 2 than prototype 1, which can be critical to accurately characterize a rapidly changing interface location in dynamic scouring. Furthermore, a practical advantage of prototype 2 was the robustness of the FO cable used when compared to the more fragile cable used in prototype 1. Such an advantage can be deemed to be critical in long-term deployment in river systems with flow charged with debris that can damage the prototype.

The error in detecting the sand-water interface for prototype 1 converged around zero, however, for prototype 2 this error most often converged around 1 cm. This error magnitude for both prototypes reflect the combination of vertical resolutions of each of the prototypes and the DTS units resolution used in the experiment. Because only one experiment of each condition was performed for prototype 1, the consistency within the tests cannot be determined, but for prototype 2 the results were consistent within each testing condition. The most range in error occurred during the high flow test. This could have been a result of the scour that was taking place around the device. The measured scour depth was approximately 1.5 cm according to the pictures taken during the experiments. The scour hole could have affected the temperature signal thus influencing the algorithm that was used to solve for the interface.

By analyzing the error over heating time duration for both prototypes, the ideal heating time was determined. Around 100 seconds in each test of prototype 2 and 300 seconds for prototype 1, the sand-water interface error stabilized or was the minimum. This means that for future work, a 100 second heat pulse could be applied instead of a 300 second heat pulse, and this would save time to run more experiments in one sitting.

After each test was completed, it was decided that the field device should be constructed using the same materials as that of prototype 2. The FO cable used for the field device had to be very durable against floating debris and animals. The device was tested in the field with promising results so far. The error was 1 to 2 cm which was similar to the error in the lab tests.

Each of the experiments proved that the sand-water interface and air-water interface could be discerned using the developed algorithm, however there is some error in this measurement. This measurement error is mostly due to the observed gradient in the interface around the device. This research should be seen as a proof of concept that the FO-DTS method can indeed detect scour under ranges of flow, with different device construction, under laboratory and field conditions. FO-DTS has the potential of being a better way to measure bridge pier scour because of its superior durability and proven accuracy. This research expands on current monitoring techniques of bridge pier scour in hopes of learning how to better predict and prevent scour.

CHAPTER 3: ONE-DIMENSIONAL (1D) AND TWO-DIMENSIONAL (2D) BRIDGE SCOUR MODELING

3.1 Introduction

The most common approach for analyzing bridge pier scour phenomena is that listed in HEC-18 (Arneson et al., 2012). This approach is popular because the equation does not need many input parameters (see *Section 1.3.1*), and it has been proven to rarely underestimate pier scour depths (Landers and Mueller, 1996). Both, 1D and 2D process-based numerical models can be used to obtain the flow variables that are used as input for predicting scour depths using the HEC-18 equation. However, these predictions are impacted by the resolution of the flow field characterization at the bridge crossing (Yu and Yu, 2008).

In 1D numerical models, flow variables are calculated at discrete locations in the streamwise direction and represent cross-sectionally averaged values. Therefore, 1D numerical models (e.g., SRH-2D) can account for such variability, having the potential to improve the flow field characterization, and thereby scour predictions, at bridge crossings.

The objective of this chapter was to compare the relative performance of 1D and 2D process-based numerical models when resolving the flow variables were solved using three different approaches: HEC-RAS 1D with hydrodynamic module only (i.e., 1D fixed-bed approach); SRH-2D with hydrodynamic module only (i.e., 2D fixed-bed approach); and SRH-2D with both hydrodynamic and morphodynamic modules (i.e., 2D mobile-bed approach). These approaches were applied to four different bridge crossings in North Carolina for evaluating the models' relative performance as a function of river properties and bridge crossing characteristics.

3.2 Study Area and Selected Bridge Crossings

Four bridge crossings were selected for comparing the relative performance of 1D and 2D numerical models when resolving the flow variables that are used as input for the application of the HEC-18 equation. Three of the bridge crossings were located in the Piedmont region of North Carolina and the remaining bridge crossing was located in the Coastal Plains region of North Carolina (Figure 3-1). Streams in the Piedmont region are characterized by having moderate slopes determined by bedrock outcrops (Doll et al., 2002). The Coastal Plain region is characterized by flat land and rolling hills and rainfall ranges from 45 to 60 inches per year (Doll et al., 2003). The bridge crossings were chosen to include a variety of channel sizes, water discharges, flow regimes, bridge geometric characteristics, and varying channel bed sediment properties. Additionally, each crossing has a USGS gauge either on the bridge or immediately upstream of the bridge. A full description of each bridge crossing is provided in the ensuing sections.

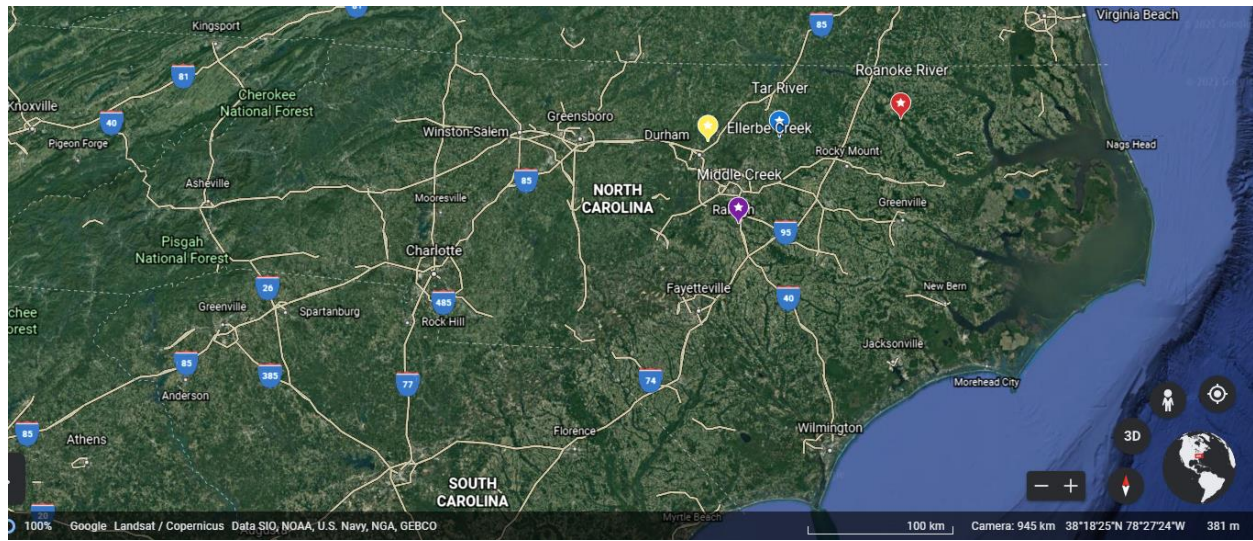


Figure 3-1. A map of the selected bridge crossings. Ellerbe Creek is marked in yellow, Middle Creek in purple, Tar River in blue, and the Roanoke River in red.

3.2.1 Ellerbe Creek

The Glenn Rd bridge crossing over Ellerbe Creek in Durham, NC ($36^{\circ}03'34.6''N$, $78^{\circ}49'56.7''W$) is located within the Neuse River basin (USGS Hydrologic Unit 03020201) in the Triassic Basins ecoregion of the Piedmont physiographic region of North Carolina. At the bridge crossing site (Figure 3-2), Ellerbe Creek is a sand-bed stream with a median grain size (D_{50}) of 0.37 mm with less than 5% fines (< 0.075 mm), a channel width of nearly 18 m, and a drainage area of 56.7 km^2 . The Glenn Rd bridge structure is 7.3 m wide and spans approximately 30 m across the stream, which flows into Falls Lake just 2.1 km downstream of the site. At its thalweg, the channel bed is approximately 6 m below the bridge deck. According to the USGS gauge station located at the site (USGS 02086849), the mean annual flow depth is about 0.5 m, and the mean daily discharge is nearly $2.8 \text{ m}^3/\text{s}$ with a median value of $0.6 \text{ m}^3/\text{s}$ and a peak value of $21.2 \text{ m}^3/\text{s}$.



Figure 3-2. The Glenn Rd bridge crossing over Ellerbe Creek in Durham, NC, USA viewed from upstream (a) and downstream (b). The channel-bed material is characterized as medium sand with less than 5% fines (c).

3.2.2 Middle Creek

The NC-50 bridge crossing over Middle Creek in Johnston County, NC ($35^{\circ}34'15.0''N$ $78^{\circ}35'26.0''W$) is located within the Neuse River basin (USGS Hydrologic Unit 03020201) in the Northern Outer Piedmont ecoregion of the Piedmont physiographic region of North Carolina. The bridge deck is 11 m wide. At the bridge crossing (Figure 3-3), Middle Creek is a sand bed stream with a D_{50} of 0.39 mm with less than 10% fines (< 0.075 mm), a channel width of 18 m, and a drainage area of 216 km^2 . According to the USGS gauge station located at the site (USGS 02088000), the mean annual flow depth is about 0.6 m, and the mean daily discharge is nearly $1.4\text{ m}^3/\text{s}$.



Figure 3-3. The NC-50 bridge crossing over Middle Creek in Johnston County, NC viewed from downstream.

3.2.3 Tar River

The Tar River site is located where the Tar River flows below the US-401 (Louisburg Rd) bridge ($36^{\circ}5'40.0''N$, $-78^{\circ}17'51.6''W$). The bridge crossing is located within the Tar River basin (USGS Hydrologic Unit 03020101) in the Northern Outer Piedmont ecoregion of the Piedmont physiographic region of North Carolina. The bridge deck is 26.8 m wide. At the bridge crossing (Figure 3-4), the Tar River is a sand-bed stream with a D_{50} of 0.39 mm with less than 10% fines (< 0.075 mm), a channel width of 30 m, and a drainage area of 1127 km^2 . According to the USGS gauge station located at the site (USGS 02081747), the mean annual flow depth is about 1.8 m, and the mean daily discharge is nearly $5.6\text{ m}^3/\text{s}$.



Figure 3-4. The US-401 bridge crossing over the Tar River in Louisburg, NC viewed from upstream.

3.2.4 Roanoke River

The Roanoke River site is located at the US-258 bridge crossing over the Roanoke River near Scotland Neck, NC ($36^{\circ}12'33.3''N$, $-77^{\circ}22'60.0''W$). The bridge crossing is located within the Roanoke River basin (USGS Hydrologic Unit 03010107) in the Mid-Atlantic Floodplains and Low Terraces ecoregion of the Coastal Plains physiographic region of North Carolina. The bridge deck is 13.7 m wide. At the bridge crossing (figure 3-5), the Roanoke River is a sand-bed stream with a D_{50} of 0.23 mm with less than 5% fines (< 0.075 mm), a channel width of 75.8 m, and a drainage area of 22688 km^2 . According to the USGS gauge located on the downstream side of the bridge, (USGS 02081000), the mean annual flow depth is about 13 m. The mean daily discharge could not be calculated from the gauge on the bridge because this gauge stopped recording discharge in 1979; however, the USGS gauge at the Roanoke Rapids Dam approximately 54 km upstream of the bridge crossing was used to estimate discharge values because this dam controls the downstream flow. According to the Roanoke Rapid Dams USGS gauge station (USGS 02080500), the mean daily discharge is nearly $328\text{ m}^3/\text{s}$.



Figure 3-5. The US-258 bridge crossing over the Roanoke River close to Scotland Neck, NC viewed from downstream.

3.3 Methods

3.3.1 Overview of Model Development and Modeling Workflow

A consistent methodology for developing the numerical models and performing the numerical simulations was applied at the four bridge crossings (Figure 3-6). First, data were collected from publicly available sources such as North Carolina Spatial Data Download (sdd.nc.gov). These data included aerial imagery as well as LiDAR data files for each bridge crossing. Field data such as water depths, water discharges, and channel bed material were also obtained. The Acoustic Doppler Current Profiler (ADCP) was used to gather information about water depths and discharges when possible, and the channel-bed material was characterized via volumetric samples and collected either with a shovel or a bottom dredge sampler. At each site where the ADCP was deployed, a combination of transects and longitudinal profiles were

recorded to obtain a two-dimensional rendering of elevation along the channel (i.e., bathymetry data).

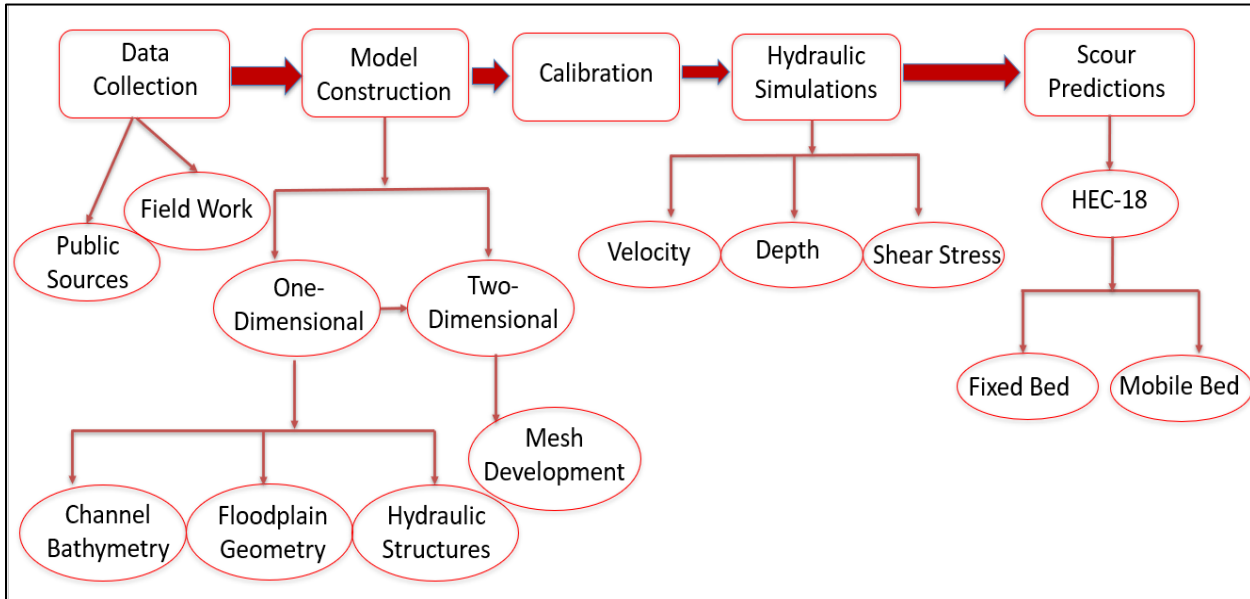


Figure 3-6. Flowchart illustrating an overview of the model development and modeling workflow.

The construction of the HEC-RAS 1D models included analyzing bathymetry data collected from the ADCP and correlating elevations of the transects to the longitudinal profiles. Then, cross-sections were drawn in RAS Mapper to match the location of the measured ADCP transects as well as two cross-sections marking the domain boundaries. The cross-sections were adjusted according to the shape and elevation of the ADCP measured transects, so that it was the most accurate representation of the channel bathymetry. The average slope measured by the ADCP was extended in either direction past the ADCP reach. The bridge was added to the river terrain model using the measurements and characteristics provided in the NCDOT inspection reports and aerial imagery to obtain the correct station. The last step in creating the river terrain model was to calculate the Manning's roughness coefficient to start the calibration process with.

This was computed using the Brownlie (1983) equations. Manning's roughness coefficient for flows in the lower regime were calculated using Equation 3.1 and coefficients for flows in the upper regime were calculated using Equation 3.2.

$$n = 1.694 * \left(\frac{R}{D_{50}} \right)^{0.1374} * S^{0.1112} * 0.5 \left(\frac{D_{84} + D_{50}}{D_{50} + D_{16}} \right)^{0.1605} * 0.034 D_{50}^{0.167} \quad (3.1)$$

$$n = 1.0213 * \left(\frac{R}{D_{50}} \right)^{0.0662} * S^{0.0395} * 0.5 \left(\frac{D_{84} + D_{50}}{D_{50} + D_{16}} \right)^{0.1282} * 0.034 D_{50}^{0.167} \quad (3.2)$$

Once the river terrain model was developed, the hydrodynamic model was calibrated using data from USGS gauges. The calibration focused on adjusting the Manning's roughness coefficients of the channel and floodplains over a range of water discharges to reduce the relative mean absolute error (RMAE) between modeling predictions and USGS gauge measurements. The criterion proposed by van Rijn et al. (2003) presented in Table 3.1 was applied to evaluate the performance of the HEC-RAS 1D models during the calibration process. The models were considered fully calibrated when the performance was dominantly good or excellent over a range of water discharges. Moreover, the calibration process also allowed for further refinement of the ADCP-based river terrain model.

Table 3.1. Relative Mean Absolute Error (RMAE) criteria from van Rijn et al. (2003) used for model calibration.

Qualification	RMAE
Excellent	<0.05
Good	0.05-0.1
Reasonable/Fair	0.1-0.2
Poor	0.2-0.3
Bad	>0.3

After completion of the calibration process for the HEC-RAS 1D models, channel cross-sectional data were imported into SRH-2D, where they were merged with LiDAR data for the floodplain geometry. The models were then developed in SRH-2D to contain features such as a mesh, boundary conditions, materials coverages, sediment materials coverages, and monitor coverages. After their development, the hydrodynamic module of the SRH-2D models were calibrated using data from in-situ USGS gages. The calibration process was two-fold. First, it focused on making sure that the size of the mesh did not impact modeling predictions. To ensure this, water depth predictions for a given discharge were computed using mesh sizes that were systematically reduced until the percent change between two consecutive mesh refinements was below than 10%. Second, like the HEC-RAS 1D models, the calibration focused on adjusting the Manning's roughness coefficients of the channel and the floodplains over a range of water discharges to reduce the RMAE between modeling predictions and USGS gage measurements.

Likewise, the models were considered fully calibrated when the performance was dominantly good or excellent (Table 3.1) over a range of water discharges. The last step in SRH-2D was to add sediment. For this, a new boundary condition had to be created as well as a sediment materials coverage. The boundary condition was altered to include sediment transport. For the upstream boundary condition, the capacity default setting was used to control the amount of sediment coming into the system. The materials coverage was created by copying the original materials layer and inputting sediment gradation and thickness values for the bed material. The floodplain was set to be non-erodible. After this was done, the model was ready for analysis.

After the SRH-2D models were fully calibrated, simulations could be run. First, hydraulic simulations were performed to compare numerical predictions of flow depth, flow velocity, and applied boundary shear stress from the 1-D and 2-D hydrodynamic models. The last step was to compare scour depth using the HEC-18 equation in each model. The flows selected for the analysis were the bankfull discharge and the discharge of the 10, 25, 50, and 100-year storm events to match the procedure outlined in HEC-18. The storm event discharges were calculated using the probability of exceedance method in which the peak flows on record were obtained from the gauge and then ranked in order of magnitude. Then the probability of exceedance was calculated at each discharge. Next, the discharges versus the probabilities were plotted to obtain a line of best fit. The equation of this line was used to calculate the 10, 25, 50, and 100-year storm events.

To compare pier scour depths using input flow variables from the SRH-2D models, the HEC-18 equation was applied first using a fixed-bed approach and then a mobile-bed approach. The mobile-bed approach simulations were performed until sediment transport conditions had reached a quasi-equilibrium state, which was determined by examining the channel-bed elevation

changes along the downstream edge of the bridge to determine at what simulation time the channel-bed approximately stopped moving. When computing scour depths in SRH-2D, the average flow depth and velocity from the approach cross section were used as well as geometry information from the NCDOT inspection reports about the bridge.

3.3.2 Ellerbe Creek

Data collection at Ellerbe Creek consisted of taking four channel-bed material volumetric samples for grain size analysis. The bed material samples were taken one about 30 m upstream of the bridge by the USGS gauge, one between the piers, one located immediately downstream of the piers, and one about 30 m downstream of the bridge.

The modeling procedure applied for the Ellerbe Creek varied the most from the procedure described previously because the ADCP was not utilized at this site due to shallow flow depths during normal flow conditions. This meant that the only source of bathymetry data available for Ellerbe Creek were the historical sounding measurements collected by the NCDOT in the bridge inspection reports and the publicly available LiDAR data for the area. When initially drawn in RAS Mapper, the cross sections all had the shape of the LiDAR data, which is inaccurate because it did not penetrate the water surface to capture bathymetry. To correct this, each cross section had to be manually altered. The four cross sections nearest the bridge (two upstream and two downstream) were created to have the same shape as what was represented by the most recent sounding measurements on August 5, 2019, while the rest of the cross sections were simplified to have a trapezoidal shape with approximately the same side slopes as the sounding measurement.

Because no survey data of the stream could be found, the bed slope was assumed to be the same as the bank slope for the reach. The bank slope was determined by plotting the

elevations of each bank at every cross section and fitting a trend line through them. The stream was divided into four segments based on bank slope and then the elevations of the cross sections were calculated based on the distance from the bridge and the calculated slope for that region. Once the elevations were determined for certain cross sections, the rest were interpolated to have a finer representation along the channel (Figure 3-7).

The procedure to develop the Ellerbe Creek SRH-2D model (Figure 3-8) was the same as described in Section 3.1.1 and shown in Figure 3-6.



Figure 3-7. Plan view of the river terrain model in HEC-RAS 1D of Ellerbe Creek. The cross-sections are in green, and the stream centerline is in blue. This image does include the interpolated cross sections. Flow direction is from left to right.

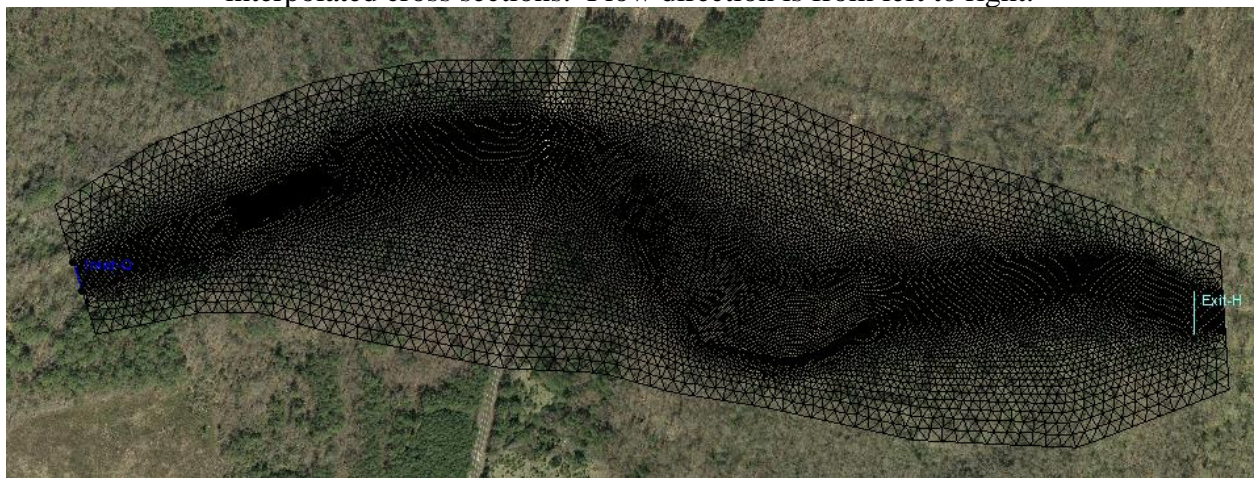


Figure 3-8. The mesh elements produced for Ellerbe Creek in SRH-2D. Flow direction is from left to right.

3.3.3 Middle Creek

Data collection at Middle Creek consisted of taking three channel-bed samples and measuring 24 transects with the ADCP. The first channel-bed material sample was taken approximately 45 m upstream of the bridge, the second was taken immediately upstream of the bridge, and the third was taken about 30 m downstream of the bridge. No samples were collected under the bridge because the sediment kept falling out of the dredge as it was being pulled up. For the ADCP setup, the ADCP's boat was tied to the kayak as to be pulled next to it. One person held the ADCP in place to prevent it from rotating while the other steered the kayak. In total 24 transects were measured using the ADCP at Middle Creek. Four transects were taken at each cross-section to increase the reliability of the ADCP measurements. This included four transects approximately 45 m upstream of the bridge, where the first sediment channel-bed material sample was collected; four transects on the upstream side of the bridge, four transects on the downstream side of the bridge; four transects about 15 m downstream of the bridge; four transects 30 m downstream of the bridge; where the farthest downstream channel-bed material sample was collected; and four longitudinal profiles along the stream.

The modeling procedure for Middle Creek differed slightly from the others because the bridge elevation was unknown. For the other sites, the bridge elevation and gauge datum were used in combination to obtain the channel bed elevation from the ADCP measured depths; however, for Middle Creek first the gauge datum was located on the ADCP transect that crossed that point in the stream and then the rest of the elevations were obtained by matching the shape of that transect to the gauge elevation. For the rest of the cross sections, the longitudinal profile measured by the ADCP that went along the centerline of the stream was considered to be the thalweg, so for each cross section that was considered the deepest point and the shape was then

calculated to match the nearest transect. After this was completed, it was noticed that the banks that were produced were too steep and tall and did not reflect the actual site. To correct this, a bankfull calculation using measured data from the USGS and regional curves (Doll et al., 2002) was executed to obtain a bankfull depth for the channel. This result seemed to be much more accurate of a physical representation, so all of the channel bed elevations were raised, with the shape held the same, to match the bankfull depth at the bridge. The final cross sections for the 1D river terrain model can be seen in Figure 3-9. The procedure to develop the Middle Creek SRH-2D model (Figure 3-10) was the same as described in Section 3.1.1 and shown in Figure 3-6.



Figure 3-9. The HEC-RAS 1D river terrain model for Middle Creek. The cross sections are in green, and the stream centerline is in blue. This image does include the interpolated cross sections. Flow direction is from left to right.



Figure 3-10. The mesh elements for Middle Creek in SRH-2D. Flow direction is from left to right.

3.3.4 Tar River

Data collection at the Tar River consisted of taking one volumetric channel-bed sediment sample under the bridge and taking four ADCP transects at one cross-section under the bridge and four longitudinal profiles along the stream. The channel-bed sediment sample was collected with a shovel near the downstream left pier. For the ADCP deployment, the ADCP boat was tied with four ropes and pulled back and forth across the channel for the transects under the bridge (figure 3-11). For the longitudinal profiles, the ADCP boat was pulled by the kayak similar to the deployment procedure followed at Middle Creek.



Figure 3-11. The ADCP being pulled by ropes across the Tar River.

For the Tar River, the water surface was assumed to be at a constant slope so by knowing the depth recorded at the gauge and the gauge datum, the water surface elevation was calculated. Then the elevations for all transects were calculated by subtracting the water surface elevation by the depth at that location. The shape of the transects upstream and downstream of the bridge were obtained from the NCDOT sounding reports. All other cross sections were interpolated to be an average spacing of 7.5 m apart (figure 3-12). The procedure to develop the Tar River SRH-2D model (Figure 3-13) was the same as described in Section 3.1.1 and shown in Figure 3-6.



Figure 3-12. A snapshot of the Tar River model in RAS Mapper. The cross sections are in green, and the stream centerline is in blue. This image does include the interpolated cross sections.

Flow direction is from left to right.

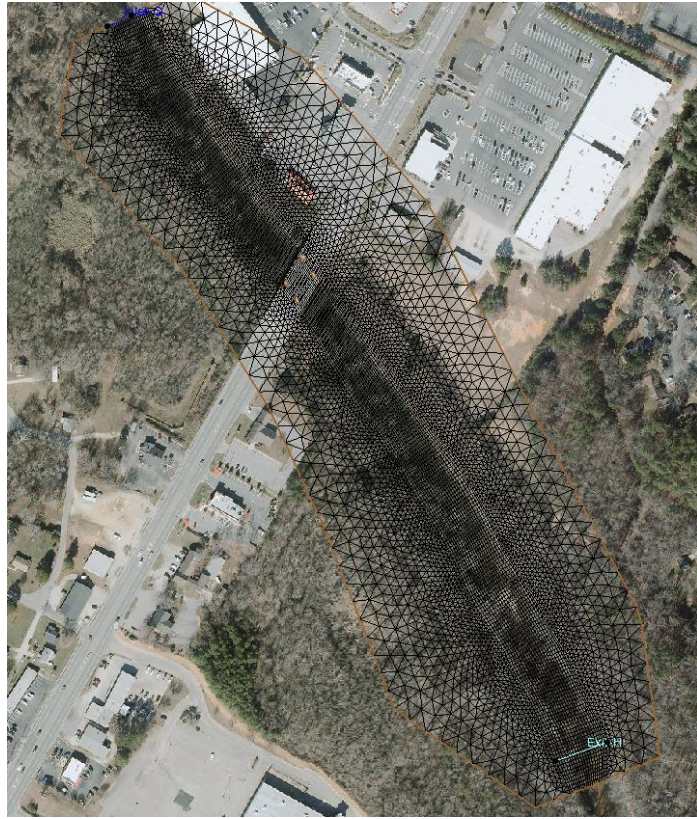


Figure 3-13. The mesh elements for the Tar River in SRH-2D. Flow direction is from left to right.

3.3.5 Roanoke River

Data collection at the Roanoke River consisted of taking two transects at four different cross-section locations as well as four longitudinal profiles up and down the stream with the ADCP. For the deployment, the ADCP was attached with a rope to the side of a motorized boat (figure 3-14). Channel-bed sediment samples were collected at the farthest upstream and downstream cross-sections as well as under the bridge.



Figure 3-14. The ADCP attached to the side of the motorboat.

Because a transect was measured that went right below the gauge, it was assumed that the gauge datum elevation was the deepest point in that transect. Once this elevation was found, the longitudinal profile depths were converted to elevations by matching the depth to that of the transect where the gauge was located. Then each following cross-sections were matched to a spot on the longitudinal profile, so that each cross-section had the original shape obtained from the ADCP measurements but had the elevation that was calculated from using the gauge as a reference point. Essentially, the slope of the model exactly matched that of the measured longitudinal profile over the reach where the ADCP was used.

Because there was only one bend in this reach, the channel was only divided into four main segments, excluding the small segments to represent the bridge piers for the SRH-2D model. After the polygons were drawn, each one was associated with the merged scatter set to have elevation data. Then the mesh was created (Figure 3-16).



Figure 3-15. A snapshot of the Roanoke River model in RAS Mapper. Flow direction is from left to right.



Figure 3-16. The mesh elements for Roanoke River in SRH-2D. Flow direction is from left to right.

3.4 Results and Discussion

3.4.1 Ellerbe Creek

Bed Material Characterization

The results of the grain size analysis can be seen in figures 3-17 through 3-20. The median grain sizes, coefficient of uniformity, coefficient of curvature, percent fines, and the UCSC classification for the four distributions are in table 3.2. The D_{50} values did not change significantly between samples, however; the farthest downstream sample has the largest percent of fines.

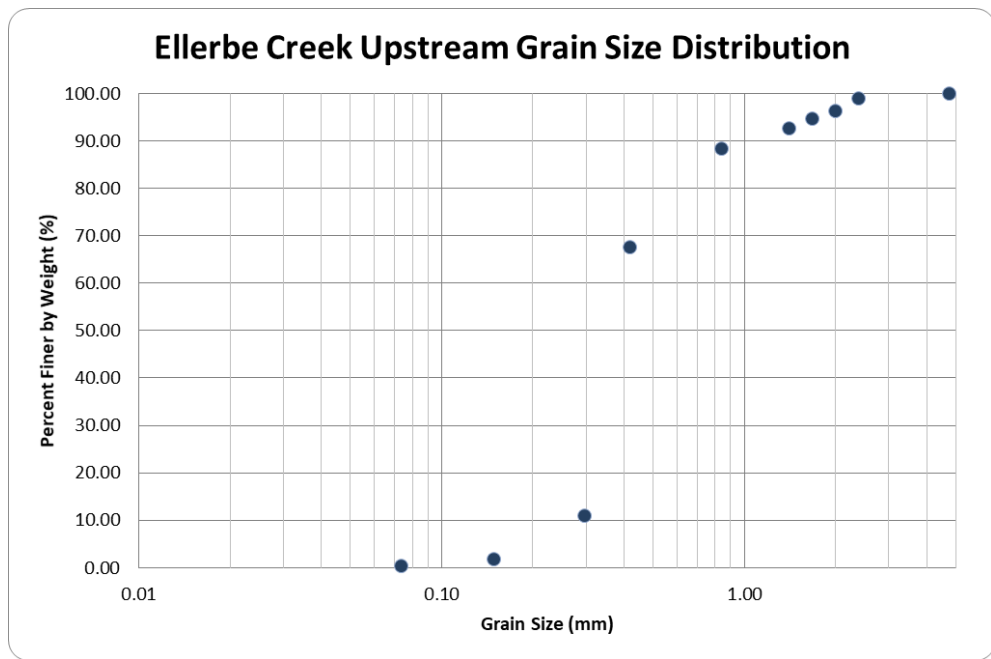


Figure 3-17. The grain size distribution of the channel-bed sediment collected approximately 30 m upstream of the bridge.

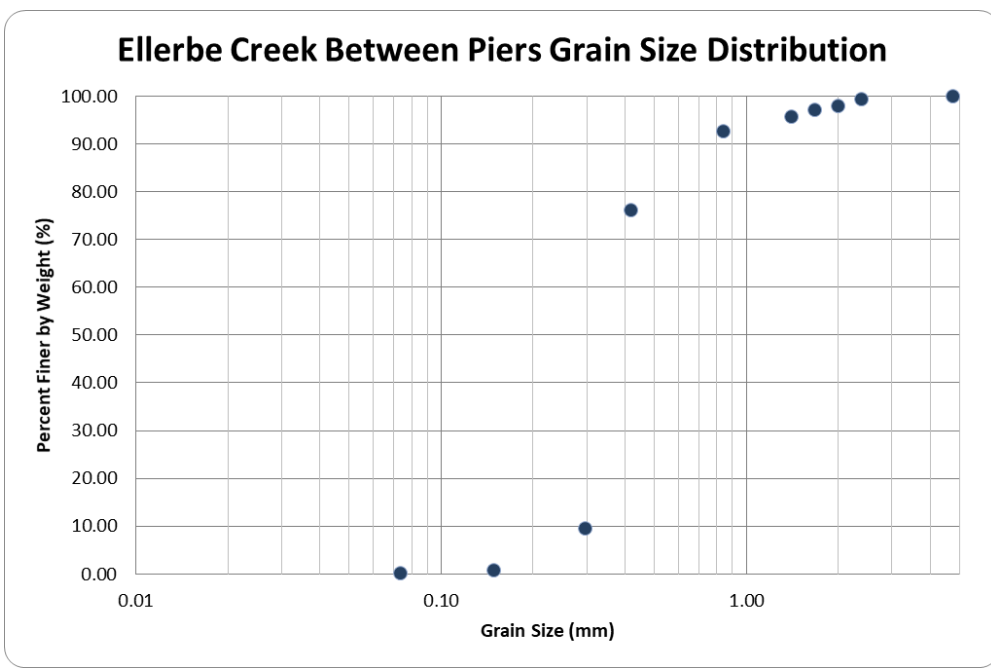


Figure 3-18. The grain size distribution of the channel-bed sediment collected at the bridge.

Ellerbe Creek Downstream of Piers Grain Size Distribution

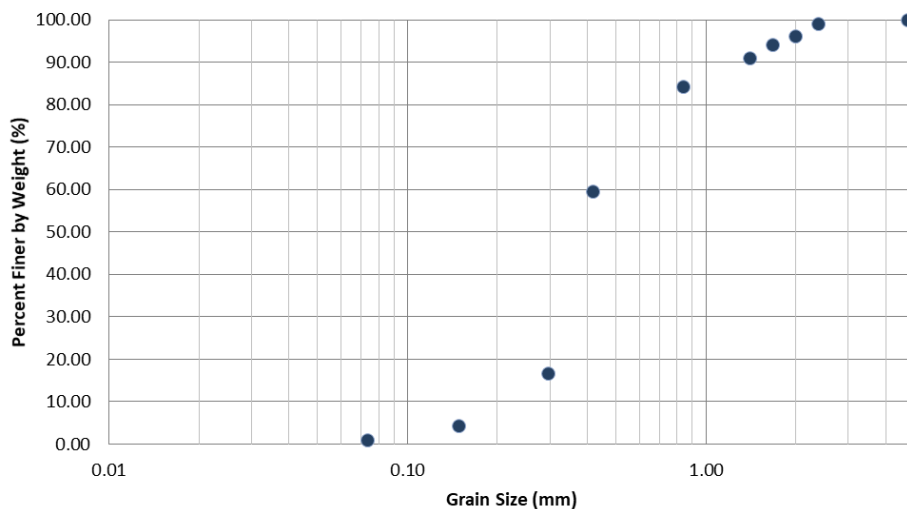


Figure 3-19. The grain size distribution of the channel-bed sediment collected immediately downstream of the bridge.

Ellerbe Creek Downstream Grain Size Distribution

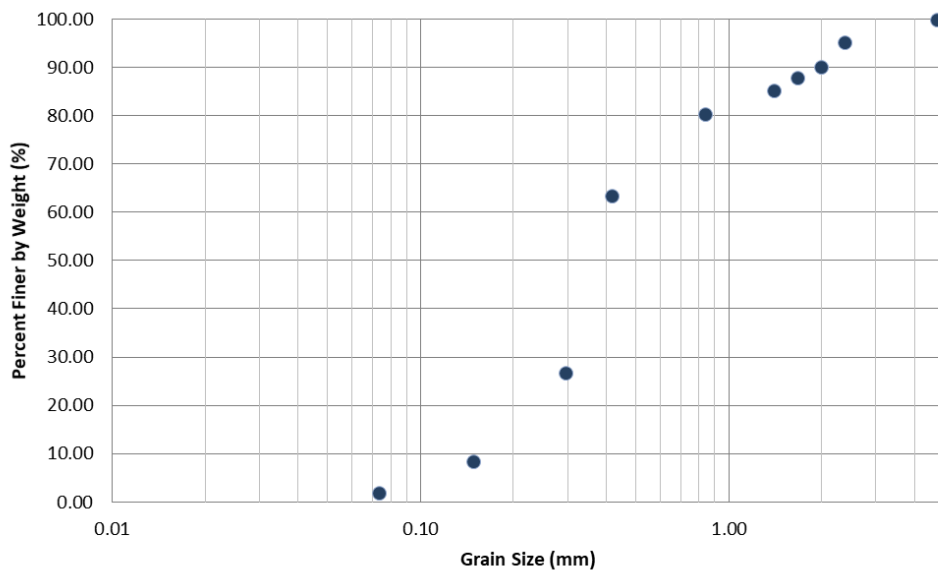


Figure 3-20. The grain size distribution of the channel-bed sediment collected approximately 30 m downstream of the bridge.

Table 3.2. A comparison of the four channel-bed sediment samples taken at Ellerbe Creek.

Sample	D50 (mm)	Coefficient of Uniformity	Coefficient of Curvature	Percentage of Fines (%)	UCSC Classification
Upstream	0.38	1.4	1.0	0.39	SP ¹
Between Piers	0.37	1.3	0.9	0.24	SP ¹
Downstream	0.39	2.0	1.2	1.05	SP ¹
Farthest Downstream	0.38	2.5	1.4	1.95	SP ¹

¹Poorly Graded Sand

Hydrodynamic Model Calibration

The HEC-RAS 1D Ellerbe Creek model was calibrated to the USGS gauge at ten flowrates (Figure 3-21). The RMAE values were mostly good and fair with the exception of a poor ranking for the 0.28 m³/s discharge (Table 3.3), which can be explained by the variability in the channel-bed form at such a low discharge (e.g., Figure 3-2).

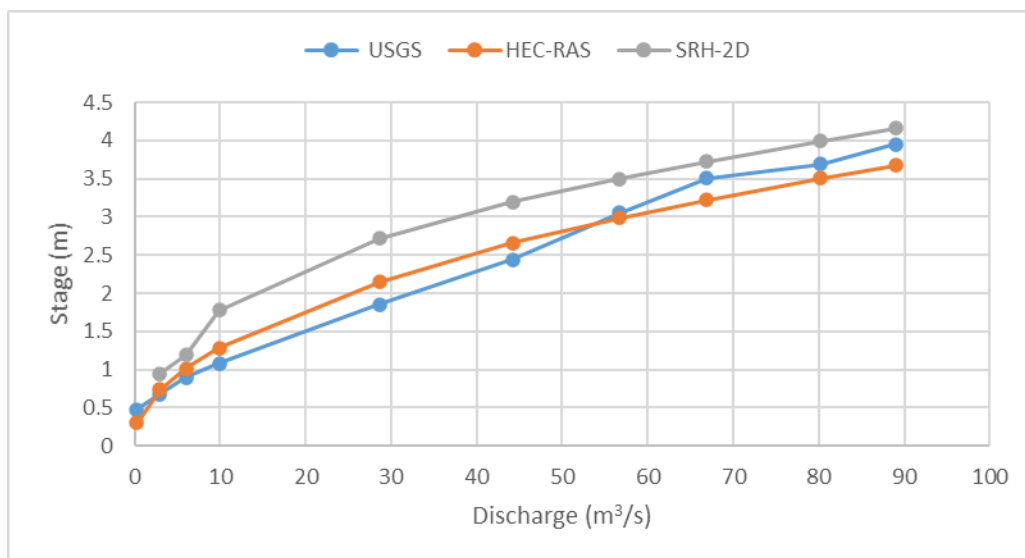


Figure 3-21. The comparison of both hydrodynamic models to the USGS gauge at Ellerbe Creek.

Table 3.3. The summary of the calibration results of both hydrodynamic models for Ellerbe Creek.

Discharge (m ³ /s)	HEC-RAS 1D			SRH-2D		
	Stage (m)	RMAE	Ranking	Stage (m)	RMAE	Ranking
0.28	0.30	0.37	Poor	N/A	N/A	N/A
2.92	0.74	0.09	Good	0.94	0.39	Poor
5.98	1.02	0.13	Fair	1.19	0.32	Poor
9.92	1.29	0.19	Fair	1.78	0.65	Poor
28.6	2.15	0.16	Fair	2.72	0.47	Poor
44.2	2.66	0.09	Good	3.19	0.31	Poor
56.7	2.98	0.02	Good	3.50	0.15	Fair
66.9	3.22	0.08	Good	3.72	0.06	Good
80.2	3.50	0.05	Good	3.99	0.08	Good
89.0	3.68	0.07	Good	4.16	0.05	Good

This calibration ended in the Manning's n value being 0.045 for the channel and 0.1 for the floodplains. These are the values that were used for the mesh size calibration in SRH-2D. The slope for the downstream boundary condition in SRH-2D was the slope of the entire reach in the HEC-RAS model 0.00137 m/m. Five different sized meshes were attempted. The boundary conditions were the same as mentioned previously and the input flow was 0.28 m³/s for all attempts. The stage near the USGS gauge was recorded for each mesh (Table 3.4). The percent change of stage between the coarser and finer mesh was then calculated. The mesh with 1.52 m spacing along the width of the channel was chosen as the mesh that would be used in the next calibration because it had less than 10% change from the previous mesh and it was more computationally efficient for the 0.91 m spaced mesh. For the hydraulic calibration in SRH-2D, the Manning's n was adjusted until the RMAEs in the testing range were classified as good. Nine flows were evaluated, and their stages compared to the USGS gauge results (Table 3.3). The calibration resulted in a Manning's n value of 0.01 for the channel and 0.2 for the floodplain.

Even though most of the RMAE values are poor or fair, the range of flows in which the model will be ultimately tested within were good, so this was deemed a successful calibration.

Table 3.4. The results of the mesh calibration for the Ellerbe Creek SRH-2D model.

Average Spacing (m)	Percent Change
7.62	N/A
3.66	-2.82
2.44	-22.6
1.52	-9.17
0.91	1.90

Hydraulic Characterization

After the calibrations were complete, Ellerbe Creek was evaluated at five discharges as mentioned in the description of the modeling workflow. First, a steady flow simulation was run for each discharge to calculate the stage, velocity, and shear stress at the bridge (Table 3.5).

Table 3.5. A summary of the HEC-RAS 1D results for the various discharges.

Discharge (m ³ /s)	Stage (m)	Velocity (m/s)	Shear Stress (N/m ²)
57	2.98	1.11	18.7
89	3.67	1.34	25.9
106	3.99	1.44	29.1
119	4.22	1.51	31.2
132	4.43	1.57	33.2

The SRH-2D model was run at the same discharges. The results of the 2D model were normalized against the 1D values so that if a value in the distribution was greater than one that means the 2D value was greater than the reported 1D value. The x-axis was also normalized to be the fraction of the distance along the water surface elevation where x equals the distance from the left side of the water surface elevation and B was the total distance. A value of 0.5 indicated a location that is in the middle of the distance covered by water. The banks and pier locations are also represented on the graphs. The graph of the results of stage at bankfull flow ($57 \text{ m}^3/\text{s}$) are shown in Figure 3-22. The graphs for the 10-year, 25-year, 50-year, and 100-year storm events are shown in Appendix A. These graphs all follow the same trend in which the maximum stage predicted by the 2D model approached the predicted 1D model but did not exceed this value. A comparison of the maximum and median normalized values across the range of discharges can be seen in Figure 3-23. The values were relatively constant with a slight decreasing trend as water discharge increased. The similarity between results implies that the discharge did not significantly impact water depth predictions between the 1D and 2D models. The fact that the values slightly decreased means that as water discharge increased, the 2D values decreased with respect to the 1D value. This could be justified by the 2D model better capturing the floodplain terrain and roughness which could mean that more water entered the floodplains and potentially dispersed farther than what the 1D model captured thus making the stage less in the 2D model.

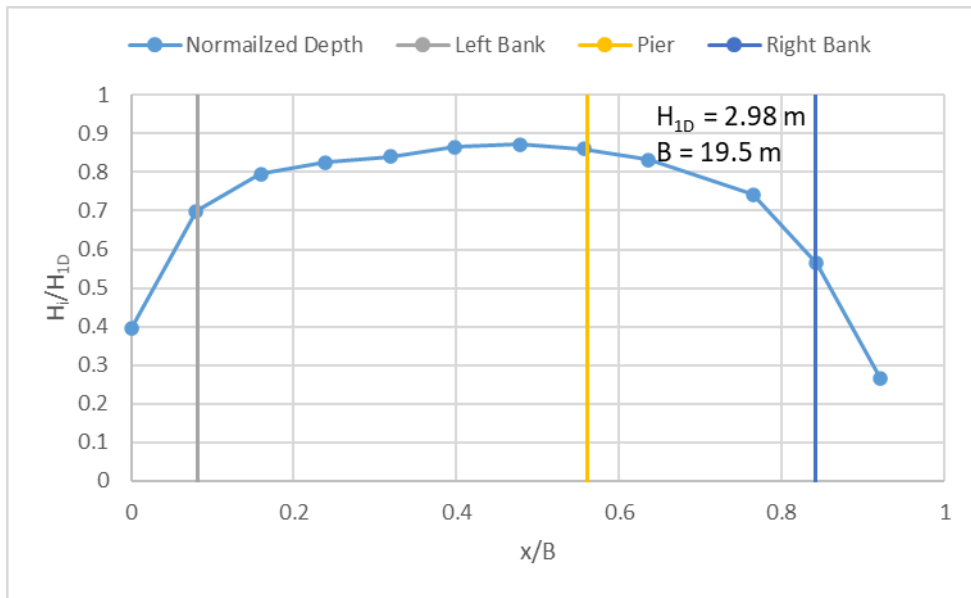


Figure 3-22. The normalized values of stage for the bankfull flow ($57 \text{ m}^3/\text{s}$) at Ellerbe Creek.

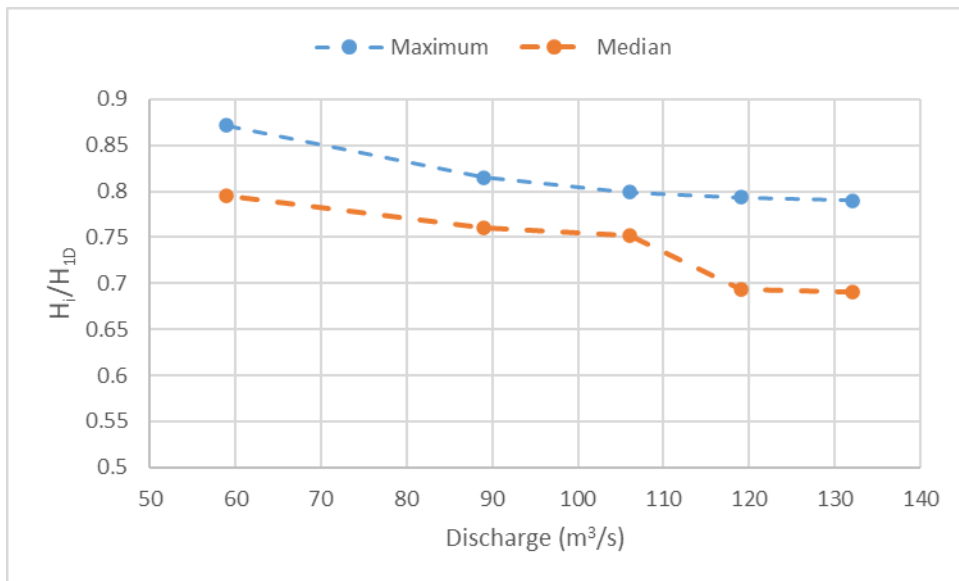


Figure 3-23. A comparison of the maximum and median normalized depths at Ellerbe Creek.

The graph of velocity at bankfull flow can be seen in figure 3-24. The rest of the graphs of velocity are presented in Appendix A. The common trend in each graph was that the velocity between the left bank and the pier is higher than the 1D value while the 2D values were lower or the same between the pier and the right bank. The normalized velocity value is close to one at the pier which implies that the 1D and 2D values are similar in that location. This is important when

considering pier scour depth using the HEC-18 equation. If the velocities and stage are similar, then the resulting scour depth would be similar. The maximum velocity predicted by the 2D model was along the right bank. A comparison of the maximum and median normalized values across the range of discharges can be seen in Figure 3-25. Like with depth, these values were held relatively constant at each discharge implying that the relationship between 1D and 2D was similar and not dependent on water discharge.

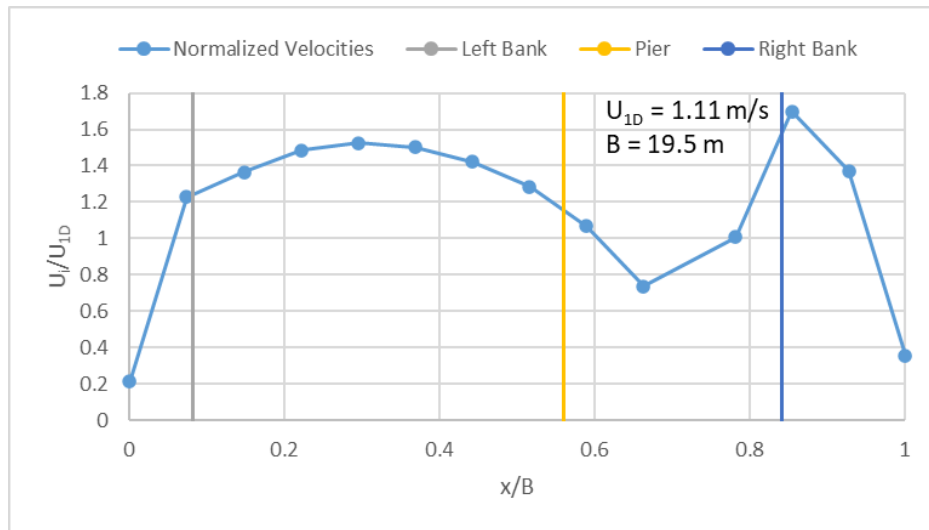


Figure 3-24. The normalized values of velocity for the bankfull flow at Ellerbe Creek.

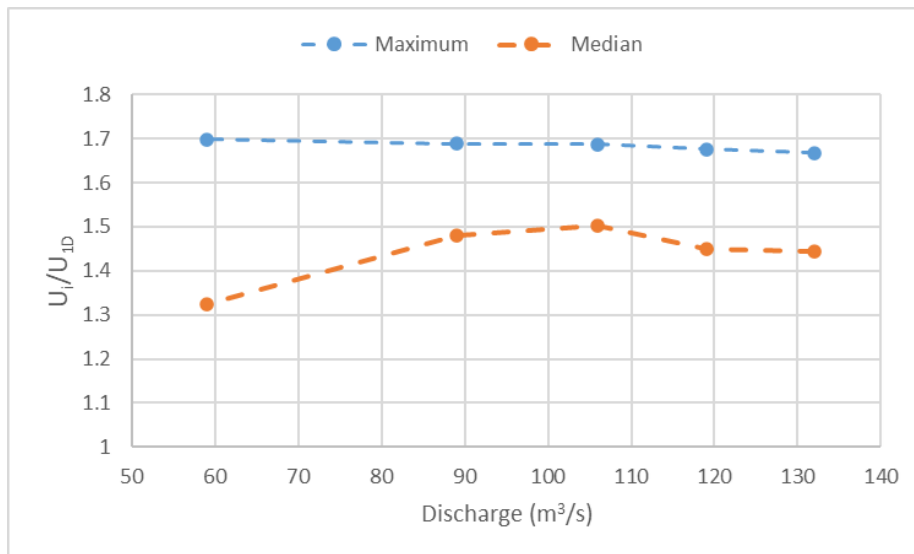


Figure 3-25. A comparison of the maximum and median normalized velocities at Ellerbe Creek.

The graph of shear stress at bankfull flow can be seen in figure 3-26. The rest of the graphs of shear stress are presented in Appendix A. The common trend in each graph was that all 2D predicted values were lower than the 1D predicted value at all flows and the lowest shear stress occurred near the pier. In the case of bankfull flow, the lowest shear stress is on the right side of the pier, but in the higher discharges it moved to the left side of the pier. A comparison of the maximum and median normalized values across the range of discharges can be seen in Figure 3-27. These values for normalized shear stress also have a slight decreasing trend which implied that as water discharge increases the 2D values of shear stress decrease with respect to the 1D value. This is because water was going into the floodplains.

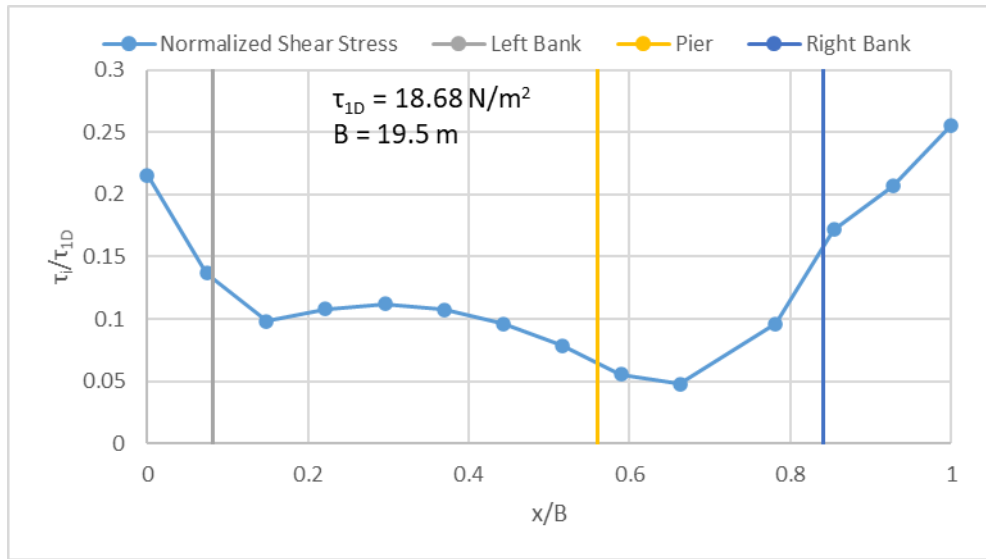


Figure 3-26. The normalized values of shear stress for the bankfull flow at Ellerbe Creek.

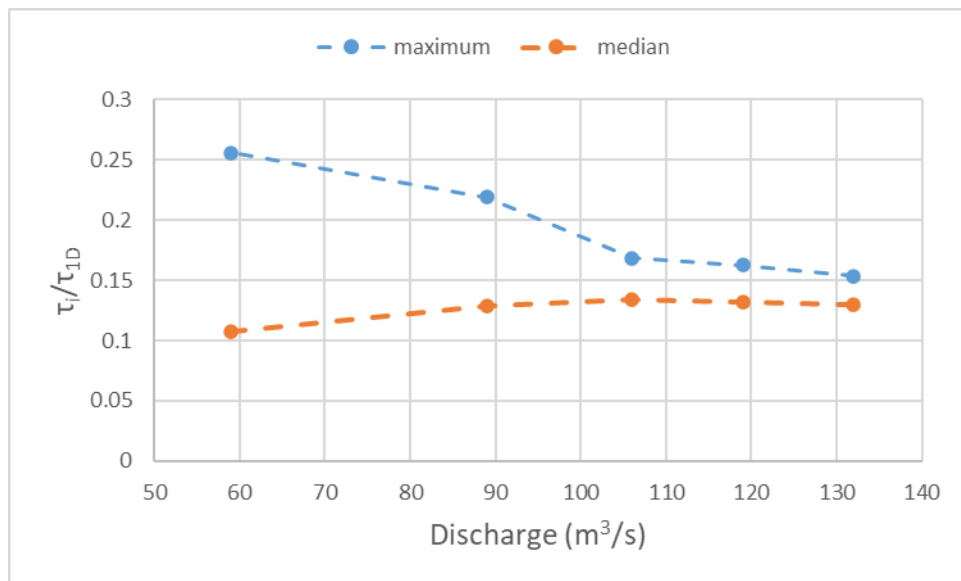


Figure 3-27. A comparison of the maximum and median normalized shear stresses at Ellerbe Creek.

Scour Depth Predictions

Scour was computed using the hydraulic design function in HEC-RAS 1D, which outputs pier scour, contraction scour, and abutment scour using the equations outlined in the HEC-18 procedure (Table 3.6). Abutment scour was negligible for this site.

The comparison of the fixed and mobile bed scour depths can be seen in table 3.6. The 1D predicted scour depth is consistently greater than both of the 2D values. This could be since 2D models produce a distribution of values and 1D just gives one value averaged over the entire cross section. This means that for 2D application of the HEC-18 equation, the modeler can choose which velocity and stage to select, whereas in 1D applications only the maximum values are outputs. It is then up to the modeler to choose to use the maximum value or choose the value directly upstream of the pier location. In this thesis the velocity near the pier was selected.

Table 3.6. The comparison of scour depths between 1D and 2D models at Ellerbe Creek.

Discharge (m ³ /s)	Pier Scour/Pier Width (y _s /a) 1D	y _{s/a} Fixed-Bed 2D	y _{s/a} Mobile-Bed 2D
57	1.68	1.40	1.49
89	1.88	1.52	1.58
106	1.96	1.60	1.62
119	1.97	1.69	1.65
132	2.01	1.65	1.68

3.4.2 Middle Creek

Bed Material Characterization

At Middle Creek, three channel-bed sediment samples were collected. Two were taken upstream of the bridge and one was downstream of the bridge. Figures 3-28 through 3-30 are the results of the grain size analysis of these samples. Other characteristics of the channel-bed sediment are reported in table 3.7. The two upstream samples were similar, but the downstream sample contained a significant amount of finer material in the silt and clay size range.

Middle Creek Upstream Sample 1 Grain Size Distribution

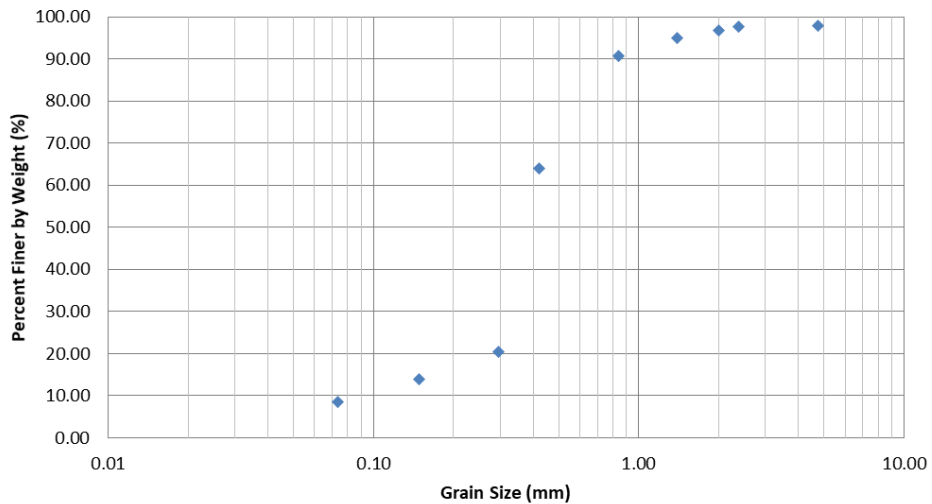


Figure 3-28. The grain size distribution of the farthest upstream channel-bed sediment sample.

Middle Creek Upstream Sample 2 Grain Size Distribution

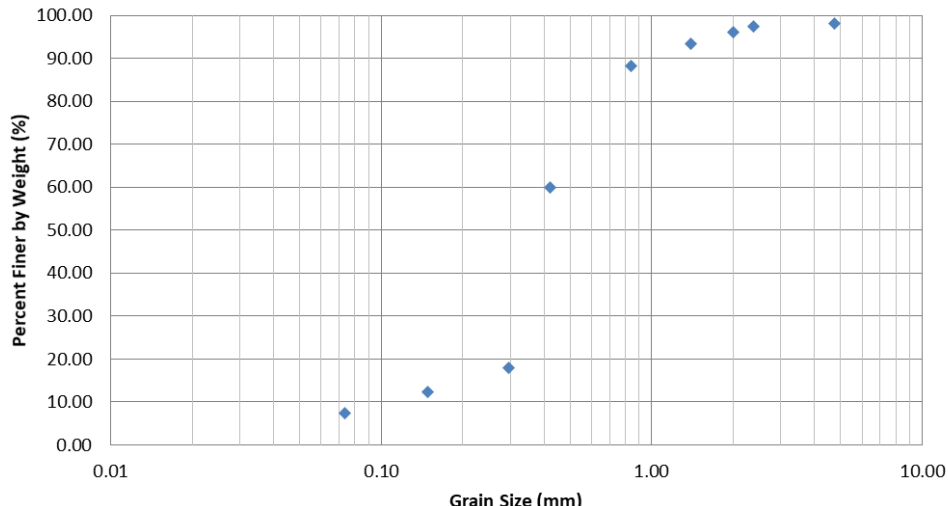


Figure 3-29. The grain size distribution of the channel-bed sediment sample taken immediately upstream of the bridge.

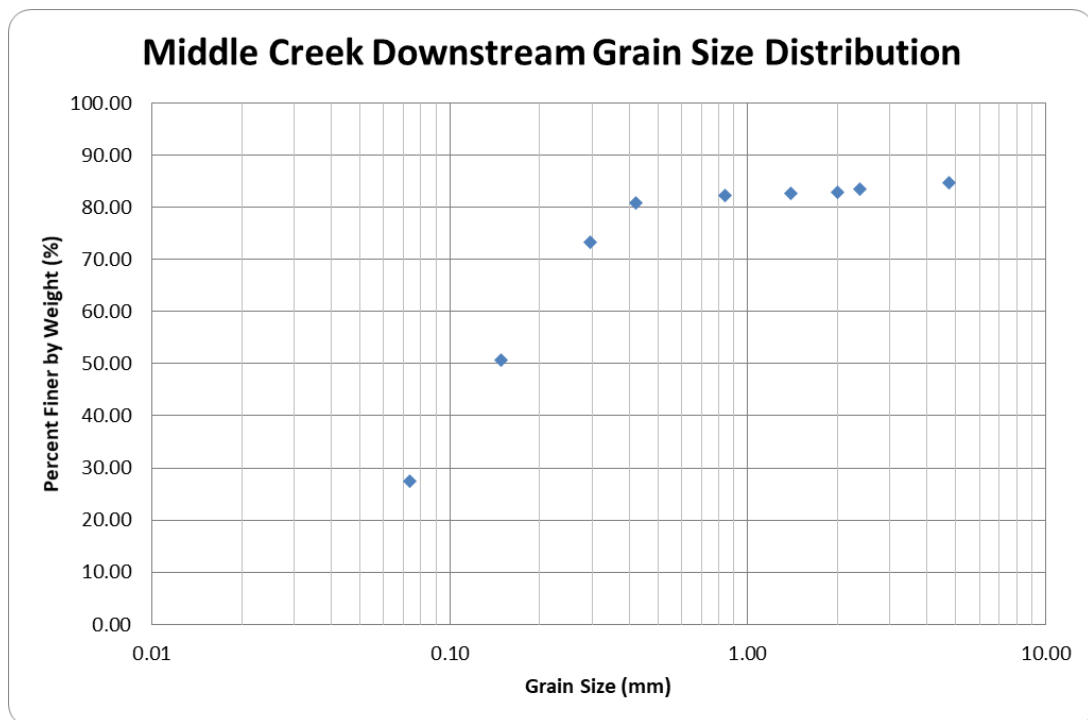


Figure 3-30. The grain size distribution of the downstream channel-bed sediment sample at Middle Creek.

Table 3.7. Summary of the characteristics of the channel-bed sediment at Middle Creek.

Sample	D ₅₀ (mm)	Coefficient of Uniformity	Coefficient of Curvature	Percent Fines (%)	UCSC Classification
Far Upstream	0.38	7.0	4.4	10	SM ¹
Upstream	0.39	4.7	2.9	9	SM ¹
Downstream	0.15	1.8	0.3	42	SC ²

SM= Silty Sand. SC= Clayey Sand

Model Calibration

The hydrodynamic model was first constructed in HEC-RAS 1D and then calibrated to the USGS gauge (figure 3-31). Eleven flows were tested at this site ranging from 0.85 m³/s to

575 m³/s (table 3.8). As with the other sites, the high and low flows were in the poor RMAE range, but this can be explained by variability in the channel-bed form or the gauge itself. Ten flows were evaluated in SRH-2D and their stage and RMAE values recorded (table 3.8). As with the 1D model there was some variability in the higher flows, but the calibration was generally deemed acceptable. The final Manning's *n* value for the SRH-2D model was 0.02.

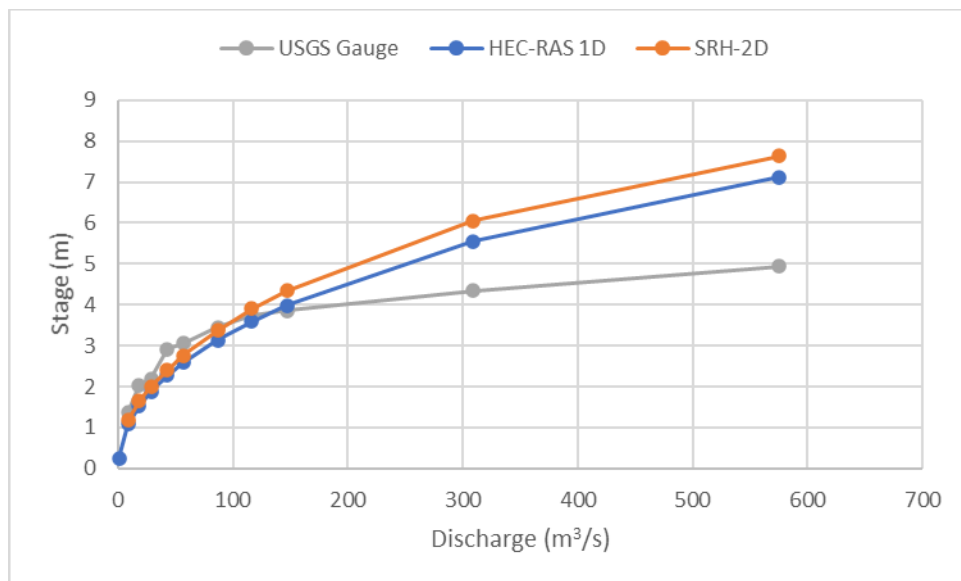


Figure 3-31. The comparison between the USGS gauge, HEC-RAS 1D, and SRH-2D stages.

Table 3.8. Summary of both the hydrodynamic model calibration results at Middle Creek.

Discharge (m ³ /s)	HEC-RAS 1D				SRH-2D		
	Stage (m)	RMAE	Ranking	Stage (m)	RMAE	Ranking	
0.85	0.26	0.53	Poor	N/A	N/A	N/A	
8.76	1.09	0.20	Poor	1.18	0.14	Fair	
18.1	1.52	0.26	Poor	1.65	0.19	Fair	
28.6	1.88	0.14	Fair	2.01	0.08	Good	
42.8	2.27	0.22	Poor	2.40	0.18	Fair	
56.7	2.58	0.16	Fair	2.75	0.10	Good	
87.0	3.14	0.09	Good	3.38	0.02	Good	
116	3.59	0.04	Good	3.91	0.04	Good	
147	3.99	0.03	Good	4.34	0.13	Fair	
309	5.55	0.28	Poor	6.05	0.39	Poor	
575	7.13	0.44	Poor	7.64	0.55	Poor	

The model was then imported into SRH-2D where first the mesh calibration took place (table 3.9). The spacing along the width was changed while the length spacing was held constant at 6 m. Only two sizes were compared because there was a very small percent change between the two meshes. The mesh with a width spacing of 4.6 m was chosen as the mesh for the hydraulic calibration.

Table 3.9. The results of the mesh calibration in SRH-2D at Middle Creek.

Average Spacing Width (m)	Percent Change
6.10	N/A
4.57	-1.62

Hydraulic Characterization

The model was first run under steady flow conditions in HEC-RAS 1D for the five discharges described in table 3.10. The stage, velocity, and shear stress were recorded for each flow (table 3.11).

Table 3.10. Description of each discharge evaluated for Middle Creek.

Discharge (m^3/s)	Description
135	Bankfull Discharge
173	10-year event
246	25-year event
301	50-year event
357	100-year event

Table 3.11. Summary of the HEC-RAS 1D results for Middle Creek.

Discharge (m ³ /s)	Stage (m)	Velocity (m/s)	Shear Stress (N/m ²)
135	3.84	1.23	26.7
173	4.31	1.37	31.7
246	5.04	1.59	40.7
301	5.51	1.74	47.0
357	5.92	1.88	53.1

Like with the other sites, the 2D values were normalized against the 1D value for that discharge and the distance was normalized against the water surface width. Figure 3-32 contains the normalized stage distribution at bankfull flow. The trend was that the maximum stage occurs at the right bank and this stage is similar to the 1D value. Because the maximum stage is slightly greater over the right bank at this flow, that means that the 2D model is predicting more flow over the banks than the 1D model. A comparison of the maximum and median normalized values for depth at the various discharges can be found in figure 3-33. The maximum values held constant near one across the different discharges which means that most of the 2D values along the cross-sections were less than the 1D value. The median values, however; decrease considerably at higher than bankfull flows. Because the roughness coefficient for the floodplains in the 2D model was less than that of the 1D model, there was a smaller height of water over the banks because of less friction.

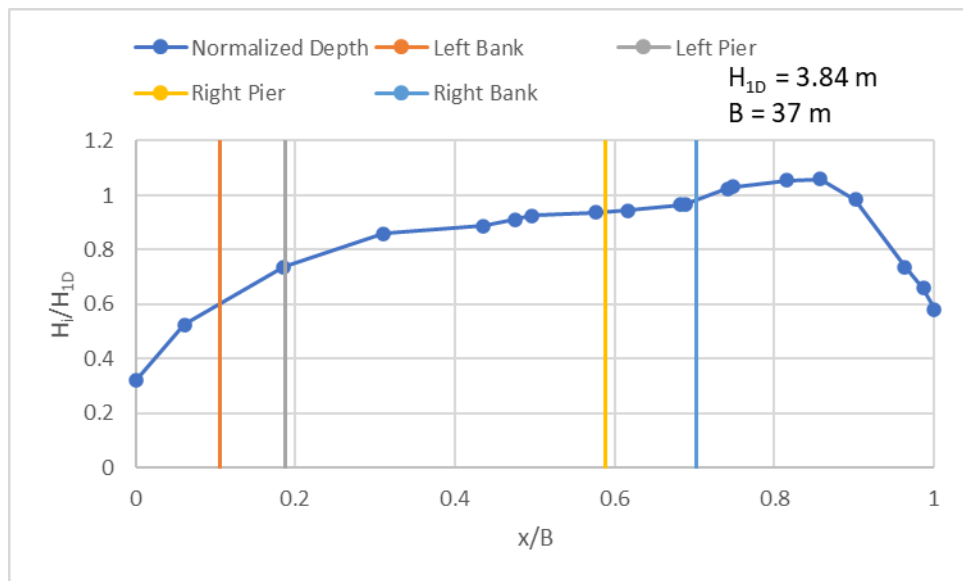


Figure 3-32. The normalized stage results at bankfull flow at Middle Creek.

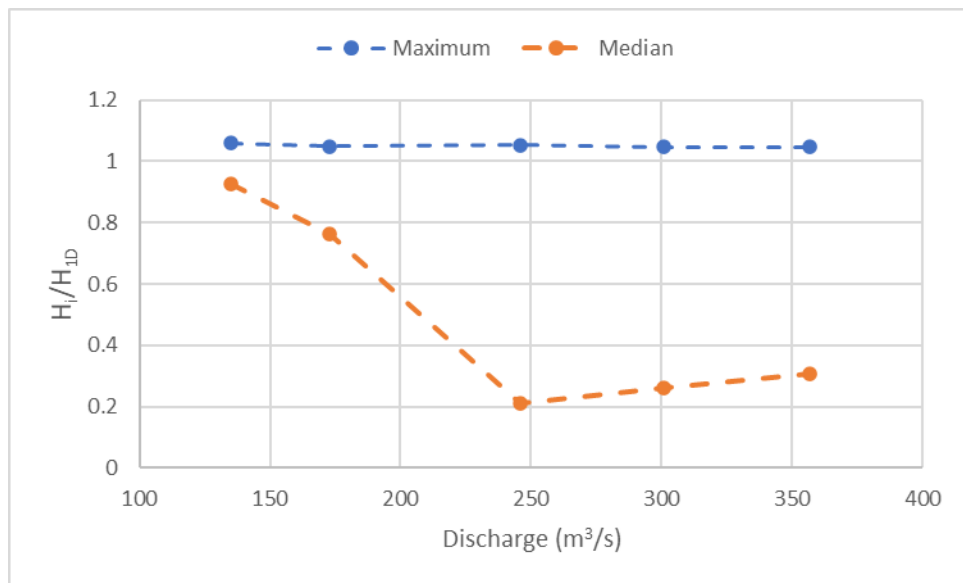


Figure 3-33. A comparison of the maximum and median normalized depths at Middle Creek.

The normalized velocity values for bankfull flow at Middle Creek can be seen in figure 3-34. This graph is representative of the other discharges. The overall trend is a significant decrease in velocity in between the piers and the maximum value which exceeds the 1D prediction is close to the right pier. This significant drop in velocity between the piers could be a result of the 2D model's ability to capture the horizontal variability of the flow field more

accurately. Because the piers act as an obstruction to flow, the water changes direction as it approaches them. This could cause a decrease in velocity as water changes course. A comparison of the maximum and median normalized values for velocity at the various discharges can be found in figure 3-35. Like the depth results, the maximum normalized velocities were held relatively constant, but for velocity it was greater than one. The median values for most discharges were low implying that the 2D values were much smaller than the 1D value. As described previously, now because in the 2D model water is overtopping the bank at this discharge, the median velocity is less due to the increased roughness compared to the channel bed.

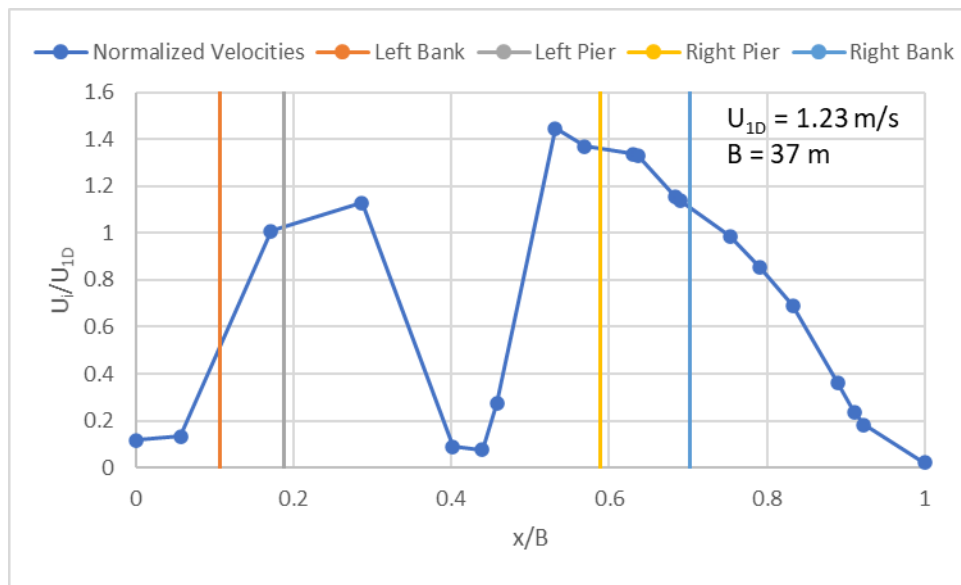


Figure 3-34. The normalized velocity values for bankfull flow at Middle Creek.

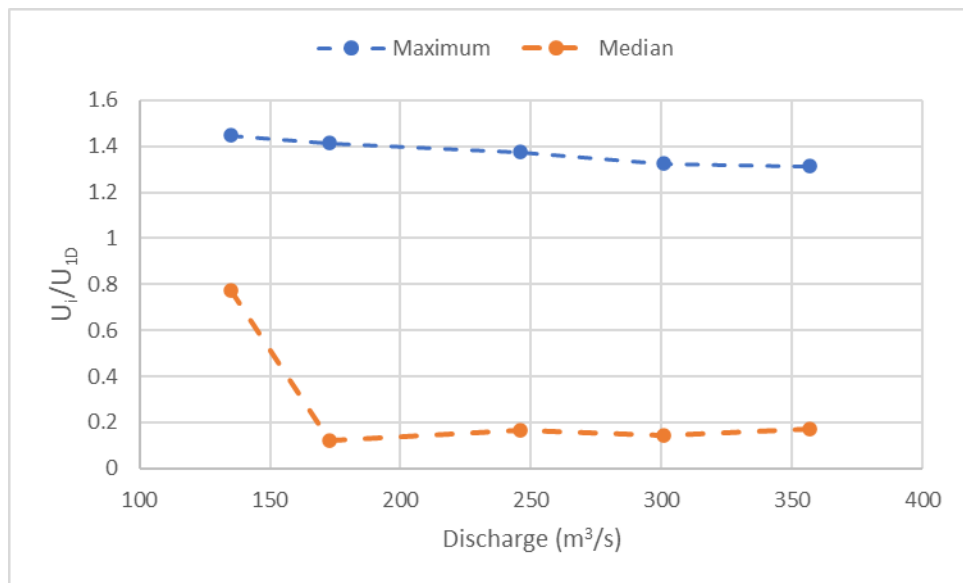


Figure 3-35. A comparison of the maximum and median normalized velocities at Middle Creek.

The shear stress values can be seen in figure 3-36. The general trend for these data are the maximum shear stress, which does not exceed the 1D value, is along the right bank. A comparison of the maximum and median normalized values for velocity at the various discharges can be found in figure 3-37. The maximum values are all less than one meaning that all of the 2D reported values are less than the HEC-RAS 1D values for each discharge. Additionally, there is a slight decreasing trend in the median values of shear stress implying that as water discharge increases the 2D values decrease with respect to the 1D value.

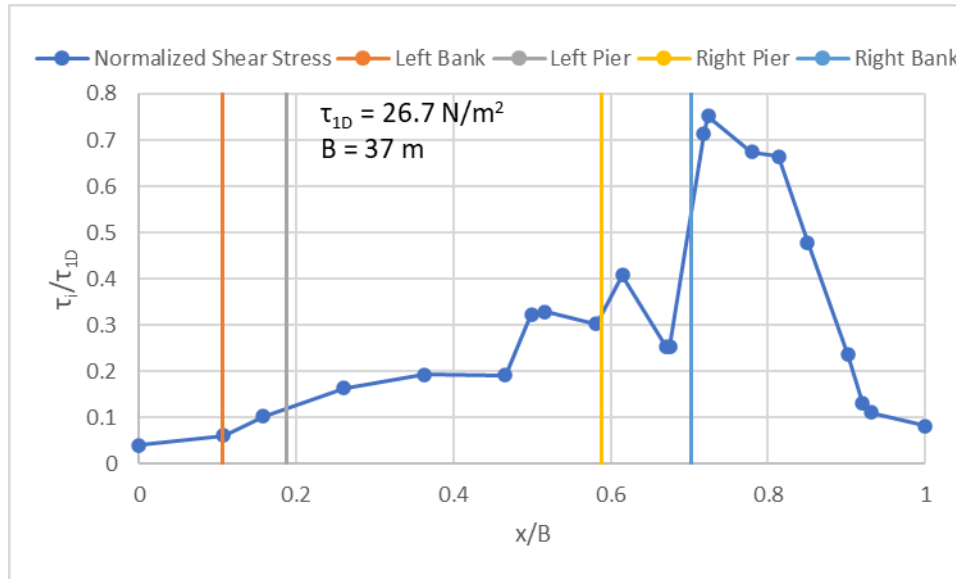


Figure 3-36. The normalized shear stress values for bankfull conditions at Middle Creek.

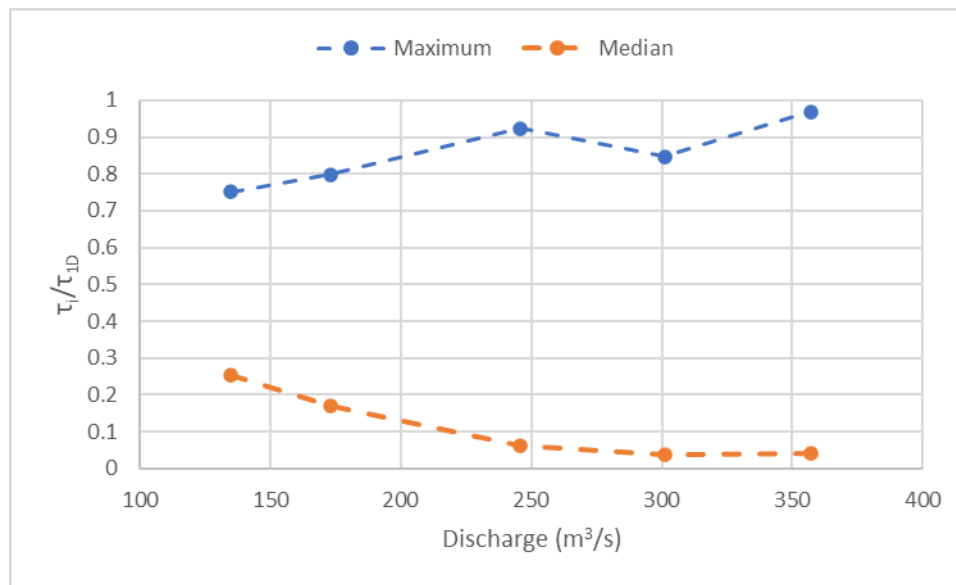


Figure 3-37. A comparison of the maximum and median normalized shear stresses at Middle Creek.

Scour Depth Predictions

Scour depths were then computed using the hydraulic design editor in HEC-RAS. Scour depths were computed again using HEC-18 on both the fixed- and mobile-bed approaches in SRH-2D (table 3.12). The 2D scour predictions were greater than the 1D for all discharges.

Table 3.12. Summary of the scour depth results in both 2D and 1D modeling approaches.

Discharge (m ³ /s)	Y _{s/a} HEC-RAS (1D)	Y _{s/a} Fixed-Bed (2D)	Y _{s/a} Mobile-Bed (2D)
135	1.91	2.16	2.43
246	2.19	2.43	2.62
301	2.27	2.52	2.52
357	1.88	2.56	2.74

3.4.3 Tar River

Bed Material Characterization

At the Tar River only one channel-bed sediment sample was collected between the left bank and the left downstream pier. The results of the grain size analysis can be found in figure 3-38. The median grain size was 0.39 mm which corresponds to a medium sand. Other characteristics of the channel-bed sediment can be found in table 3.13.

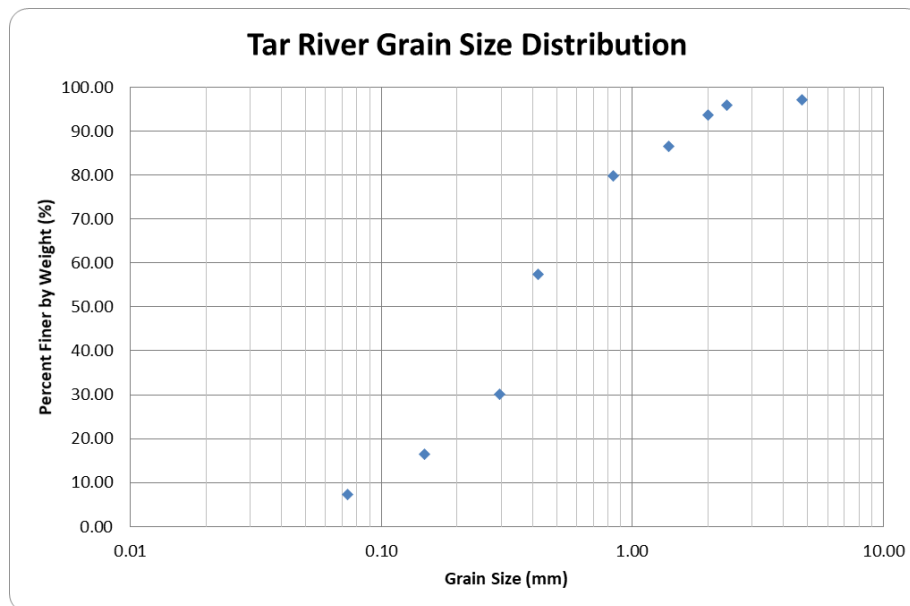


Figure 3-38. The results of the grain size distribution from the Tar River.

Table 3.13 Characteristics of the channel-bed material sample taken at Tar River.

Sample	D ₅₀ (mm)	Coefficient of Uniformity	Coefficient of Curvature	Percent Fines (%)	UCSC Classification
Tar River	0.39	5.4	2.6	10	SM ¹

SM = Silty Sand

Model Calibration

Following construction of the HEC-RAS 1D model, the model was calibrated against the USGS gauge at 16 discharges (figure 3-39). The stage and RMAE values from the model were recorded at each discharge (Table 3.14). There are some poor RMAE values for lower flows, but this can also be accounted for by high channel-bed form variability at low flows. Most of the values in the testing range are good or fair, so this was deemed a successful calibration. Nine flows were evaluated in SRH-2D and their stage and RMAE values recorded (table 3.14). Less flows were evaluated in 2D due to the computational time it took to run each model. The values are mostly good with some exceptions in the upper and lower ranges of flow. The poor RMAE at the 72 m³/s flow can be justified by channel-bed form variability as described previously; however, the poor values in the higher range could be explained if the flow exceeds the measuring range of the gauge, then often times either an estimate is recorded or a proxy from a similar site somewhere else is used in its place. The final Manning's *n* value for the SRH-2D model was 0.055.

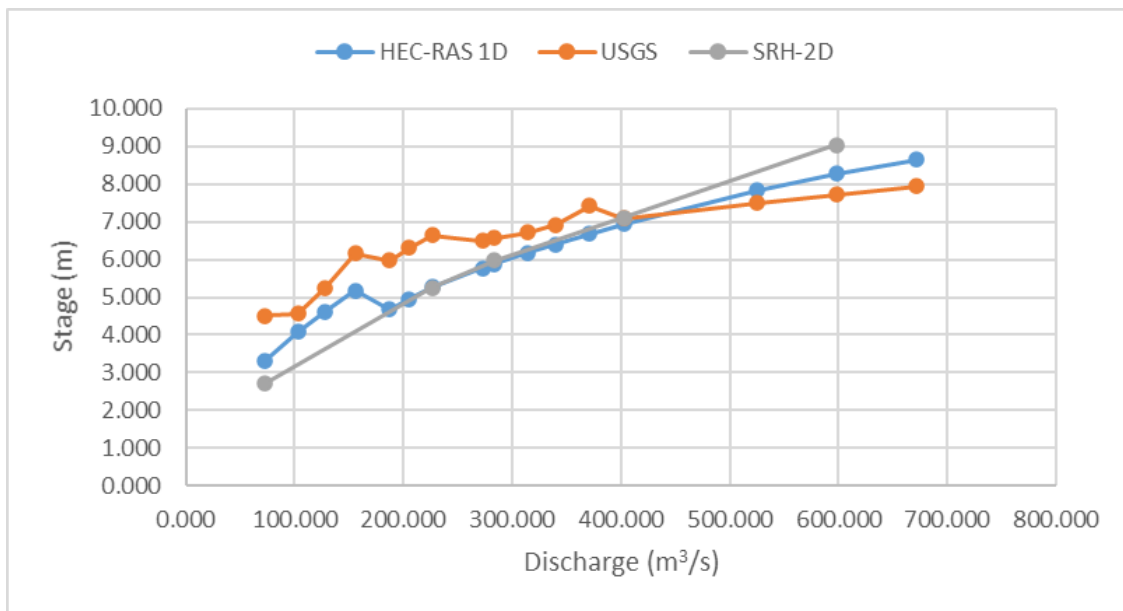


Figure 3-39. The comparison of the USGS gauge, HEC-RAS 1D, and SRH-2D stages.

Table 3.14. The summary of the hydrodynamic models' calibration results at Tar River.

Discharge (m^3/s)	HEC-RAS 1D			SRH-2D		
	Stage (m)	RMAE	Ranking	Stage (m)	RMAE	Ranking
72.3	3.30	0.27	Poor	2.88	0.36	Poor
103	4.09	0.11	Fair	N/A	N/A	N/A
128	4.62	0.12	Fair	N/A	N/A	N/A
156	5.17	0.16	Fair	N/A	N/A	N/A
187	4.67	0.22	Poor	N/A	N/A	N/A
205	4.96	0.21	Poor	N/A	N/A	N/A
227	5.28	0.20	Poor	5.44	0.18	Fair
273	5.78	0.11	Fair	5.99	0.08	Good
283	5.88	0.11	Fair	6.12	0.07	Good
315	6.17	0.08	Good	6.45	0.04	Good
340	6.40	0.07	Good	N/A	N/A	N/A
371	6.67	0.10	Fair	N/A	N/A	N/A
402	6.94	0.02	Good	7.42	0.05	Good
524	7.84	0.04	Good	N/A	N/A	N/A
598	8.27	0.07	Good	9.31	0.20	Poor
672	8.64	0.09	Good	9.72	0.22	Poor

After the model was calibrated in HEC-RAS, the bathymetry was imported into SRH-2D for calibration. First the mesh was calibrated (table 3.15). The mesh calibration resulted in selecting a mesh with spacing 3 m by 1.5 m. This mesh had a low percent change from the previous mesh and represented the channel adequately.

Table 3.15. The results of the mesh calibration of Tar River in SRH-2D.

Length Average Spacing (m)	Width Average Spacing (m)	% Change
6.10	6.10	N/A
4.60	4.60	-19.0
3.05	3.05	-1.23
3.05	1.50	-7.93

Hydraulic Characterization

After both models were calibrated, first the HEC-RAS model was run at the five flows listed in table 3.16. The model was run to obtain stage, velocity, and shear stress at each discharge under steady flow conditions (table 3.17).

Table 3.16. The discharges used to evaluate the Tar River.

Discharge (m^3/s)	Description
227	Bankfull Flow
390	10-year event
514	25-year event
609	50-year event
703	100-year event

Table 3.17. The summary of the 1D results for the steady flow simulations on Tar River.

Discharge (m ³ /s)	Stage (m)	Velocity (m/s)	Shear Stress (N/m ²)
227	5.32	1.60	41.7
390	6.71	1.95	57.2
514	7.48	2.18	68.4
609	7.99	2.35	76.8
703	8.45	2.49	84.4

The same five discharges were also run in SRH-2D to obtain the same outputs. Each value was normalized against the 1D produced value and the distance was normalized against the water surface width. The results of the stage comparison at the bankfull discharge can be seen in figure 3-40. The rest of the results can be found in Appendix A. The general trend was that between the piers the stage results produced by SRH-2D were very similar to the 1D value. A comparison of the maximum and median values of normalized depths across the various water discharges can be found in figure 3-41. Both the maximum and median normalized values of depth remained constant near one meaning that independent of the discharge the 1D and 2D results were similar.

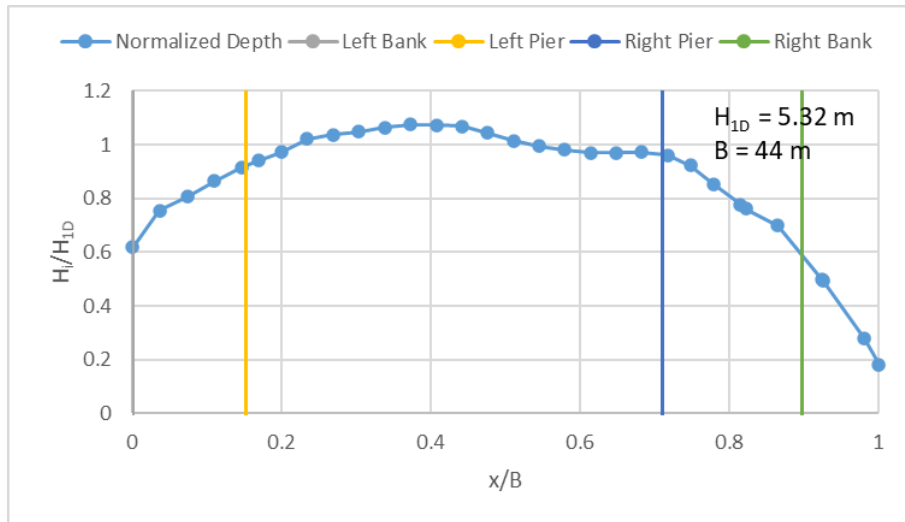


Figure 3-40. The stage results at bankfull flow for the Tar River.

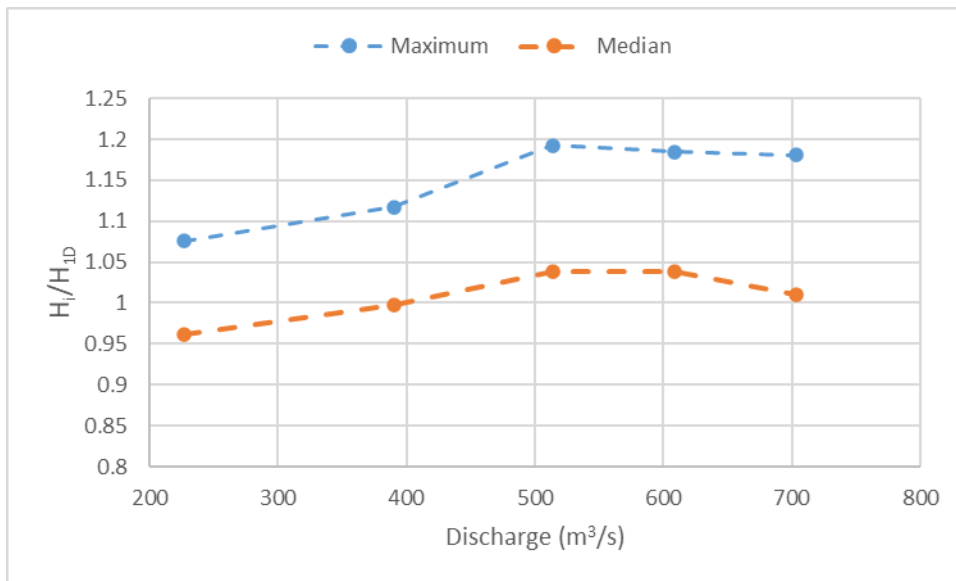


Figure 3-41. A comparison of normalized depths at the Tar River.

The results of the velocity distribution can be found in figure 3-42. The general trend was that the velocity was highest between the piers and even exceeded the 1D value in this location and was lowest near the piers and over the banks. A comparison of the maximum and median values of normalized velocities across the various water discharges can be found in figure 3-43. The maximum normalized velocities are all slightly greater than one which means that most of the 2D values along the cross-section are less than the 1D value.

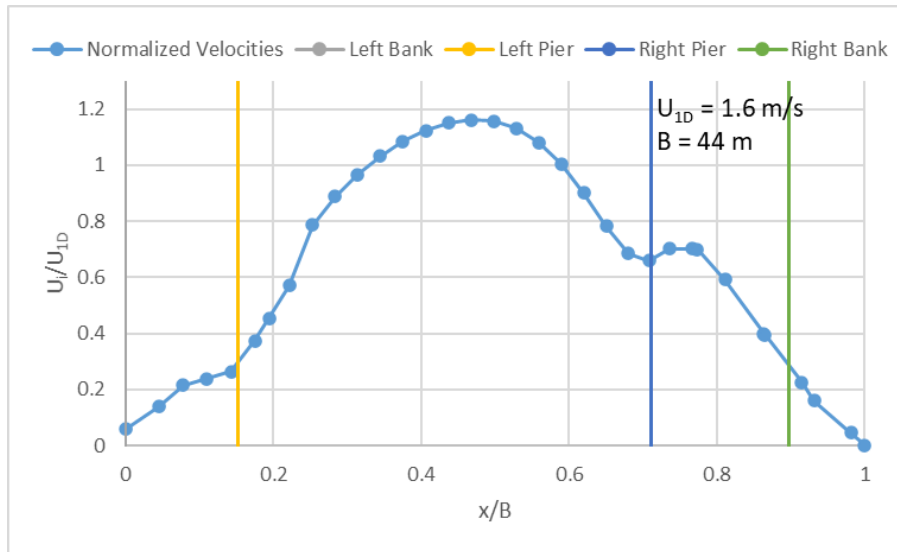


Figure 3-42. The velocity results at bankfull flow for the Tar River.

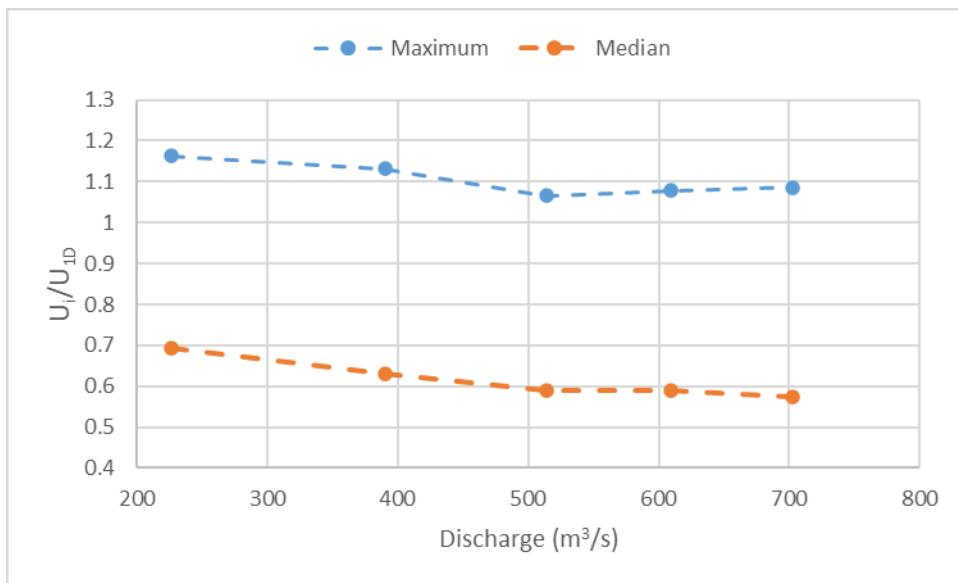


Figure 3-43. A comparison of normalized velocities at the Tar River.

The results for the normalized shear stress values can be found in figure 3-44. The trend was that the maximum shear stress occurred between the piers and exceeded the 1D shear stress. There was small decrease in shear stress as water approached the piers and banks. A comparison of the maximum and median values of normalized shear stresses across the various water discharges can be found in figure 3-45. As with the velocity, the maximum normalized shear stress

5values are all greater than one and fairly constant meaning that the relationship between the 1D and 2D results is independent of water discharge.

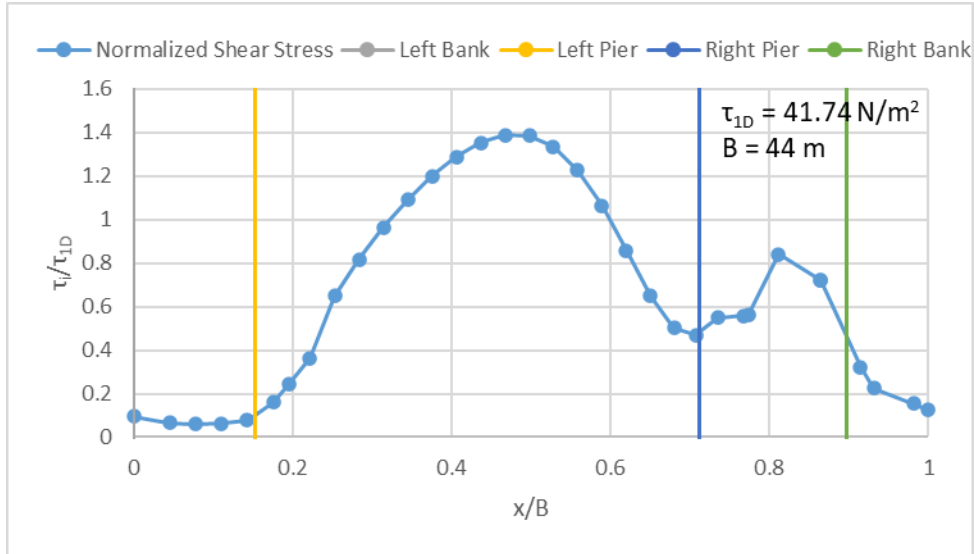


Figure 3-44. The results of shear stress for bankfull flow for the Tar River.

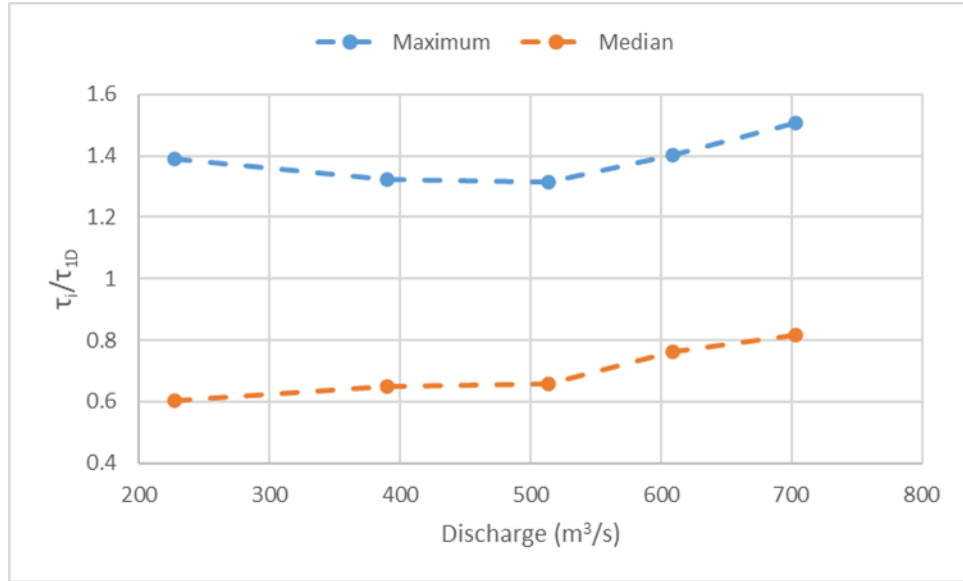


Figure 3-45. A comparison of normalized shear stresses at the Tar River.

Scour Depth Predictions

Scour depths were then computed in HEC-RAS 1D using the hydraulic design calculator. Pier scour was normalized against the width of the pier as is the standard described in HEC-18 (Arneson et al., 2012).

Scour depths were computed in SRH-2D using the procedure outlined previously. The results comparing the fixed and mobile bed simulations to the 1D computed scour can be found in table 3.18. For most of the discharges, the mobile bed scour depth was less than the fixed bed scour depth and all the 2D scour depths were less than the 1D computed scour depths.

Table 3.18. The comparison between the scour depths of the 1D and 2D modeling approaches at the Tar River.

Discharge (m ³ /s)	Pier Scour/Pier Width (Y _s /a) (1D)	Y _s /a Fixed-Bed (2D)	Y _s /a Mobile-Bed (2D)
227	1.75	1.55	1.46
390	1.94	1.63	1.58
514	2.01	1.62	1.62
609	2.05	1.68	1.65
703	2.08	1.72	1.68

3.4.4 Roanoke River

Bed Material Characterization

For the field data collection at Roanoke River, three channel-bed sediment samples were collected and analyzed to obtain grain size distributions. The results from the grain size distributions can be seen in figures 3-46 through 3-48. Characteristic values are also reported in

table 3.19. The upstream and between the piers channel-bed sediment samples were relatively similar, but the channel-bed sediment sample taken downstream was composed of significantly finer grain sizes.

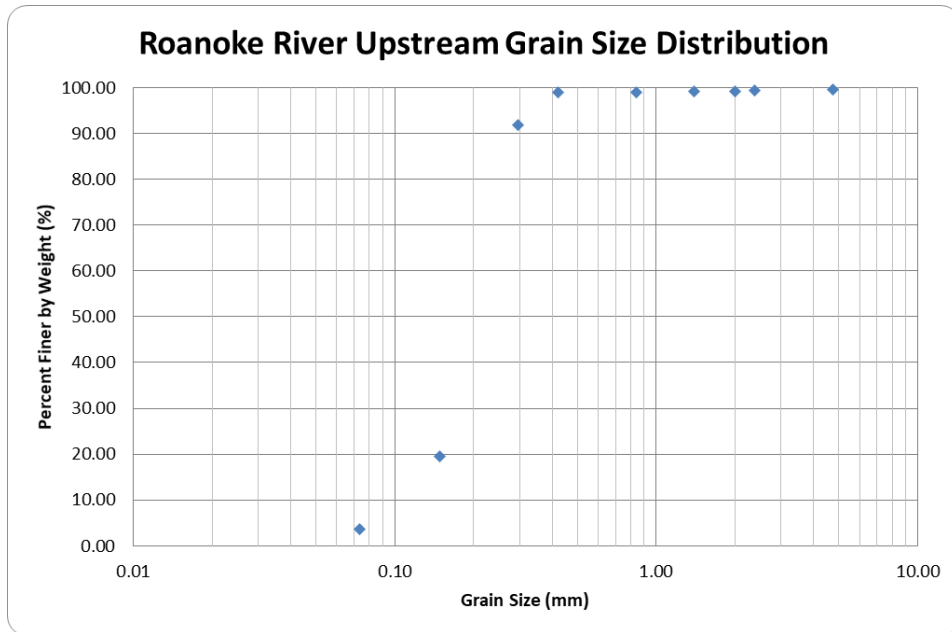


Figure 3-46. The grain size distribution of the upstream channel-bed sediment sample at Roanoke River.

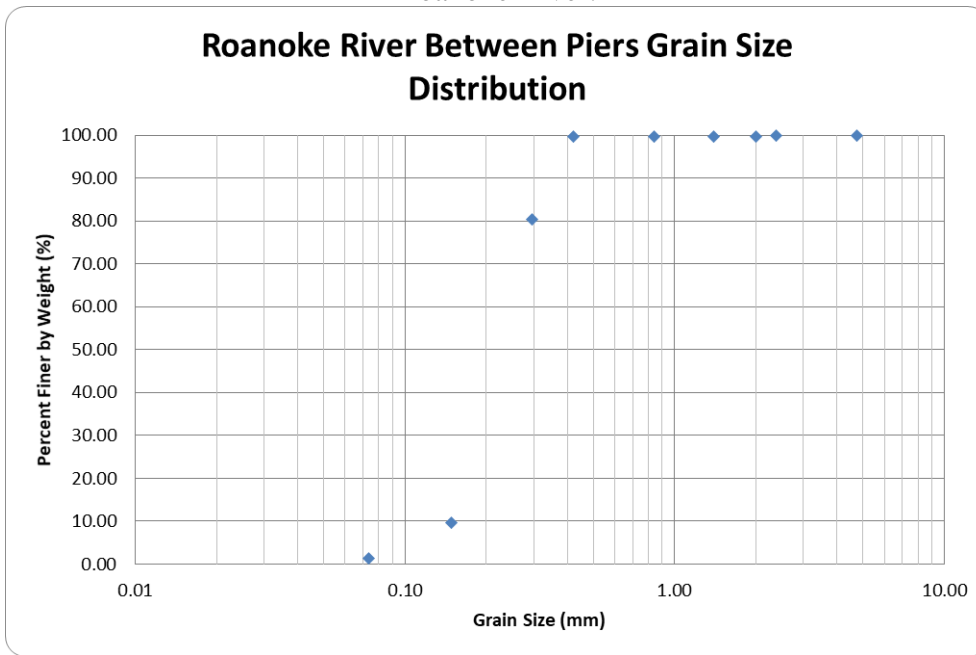


Figure 3-47. The grain size distribution of the channel-bed sediment sample under the bridge at Roanoke River.

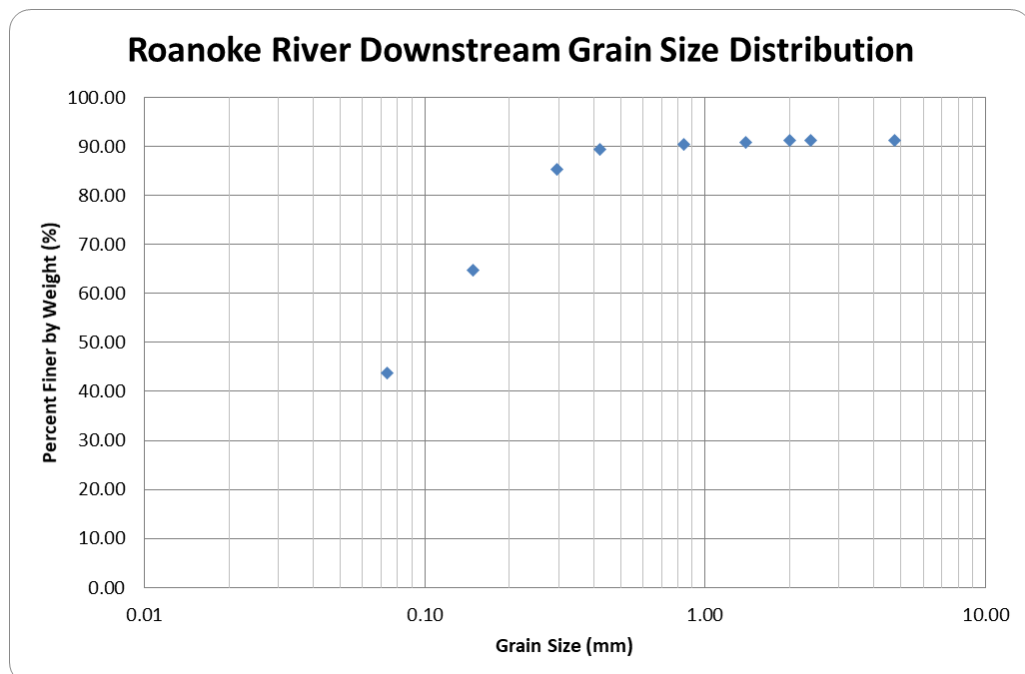


Figure 3-48. The grain size distribution of the downstream channel-bed sediment sample at Roanoke River.

Table 3.19. Characteristics of the channel-bed sediment samples taken at the Roanoke River.

Sample	D50 (mm)	Coefficient of Uniformity	Coefficient of Curvature	Percent of Fines (%)	UCSC Classification
Upstream	0.21	2.2	1.2	4.1	SP ¹
Between Piers	0.23	1.7	1.0	1.5	SP ¹
Downstream	0.1	2.8	0.1	50	ML ¹

SP = Poorly graded sand, ML = Silt

Model Calibration

After the models were built in HEC-RAS 1D following the procedure outlined previously, the Manning's roughness was solved for using equations 3.1 and 3.2. The Manning's roughness obtained was 0.0215 for the channel and 0.1 was assumed for the floodplain as an initial value. The 1D model was calibrated against 14 flows from the USGS gauge located on the bridge (figure 3-49). After modifying the roughness, the final RMAE values were either good or fair for all values (Table 3.20). The final Manning's n value for the SRH-2D model was 0.035.

The 2D model was next calibrated against the USGS gauge at the bridge. All the values are good or fair except for the $203 \text{ m}^3/\text{s}$ discharge. This was the flowrate obtained by the ADCP from the day data was collected in the field.

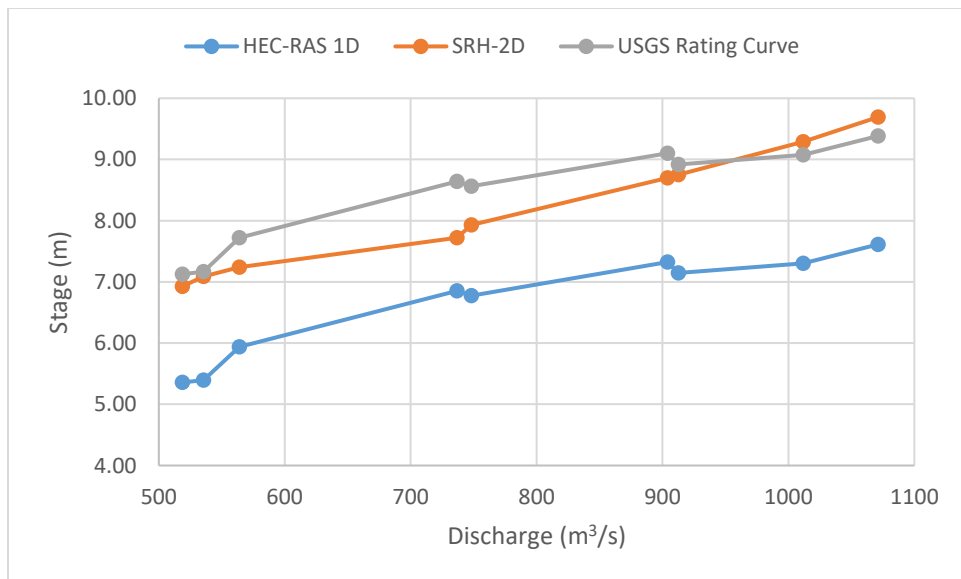


Figure 3-49. The comparison of the USGS gauge, HEC-RAS 1D, and SRH-2D stages.

Table 3.20. The hydrodynamic models' calibration results for the Roanoke River.

Discharge (m ³ /s)	HEC-RAS 1D			SRH-2D		
	Stage (m)	RMAE	Ranking	Stage (m)	RMAE	Ranking
203	N/A	N/A	N/A	6.59	0.66	Poor
519	5.36	0.11	Fair	6.93	0.03	Good
536	5.40	0.11	Fair	7.09	0.01	Good
564	5.94	0.10	Fair	7.24	0.06	Good
737	6.85	0.09	Good	7.72	0.11	Fair
748	6.78	0.09	Good	7.93	0.07	Good
904	7.32	0.09	Good	8.70	0.04	Good
913	7.15	0.09	Good	8.75	0.02	Good
1012	7.30	0.08	Good	9.29	0.02	Good
1071	7.61	0.08	Good	9.69	0.03	Good
1100	7.52	0.08	Good	N/A	N/A	N/A
1131	7.82	0.08	Good	N/A	N/A	N/A
1148	7.80	0.08	Good	N/A	N/A	N/A
1570	8.40	0.07	Good	N/A	N/A	N/A
3372	9.75	0.04	Good	N/A	N/A	N/A

Following a successful calibration in HEC-RAS 1D, the model's bathymetry was input in SRH-2D and the 2D model was constructed. The mesh size was calibrated so that the average node spacing along the lengths of the polygons were held constant at 5 m while the width was adjusted (table 3.21). The 1.5 m width spaced mesh was selected to move on to the next calibration because there was a less than 10% change from it to the next mesh and the 0.91 mesh required too much computational power.

Table 3.21. The mesh calibration results of the 2D model of the Roanoke River.

Average Spacing Width (m)	Percent Change
6.10	N/A
4.57	-41.7
3.05	20.7
1.52	-19.9
0.91	-2.62

Hydraulic Characterization

Roanoke River was evaluated at six different flow rates in both 1D and 2D models (table 3.22). The storm events were calculated using a flood frequency analysis as described above, but the only flows that were used were after 1950 when the Roanoke Rapids dam was built upstream. The presence of the dam could explain why the 100-year event is less than bankfull discharge. The HEC-RAS 1D values from the flow only simulations are reported in table 3.23.

Table 3.22. The discharges used to evaluate the Roanoke River.

Discharge (m ³ /s)	Description
203	ADCP measured
997	10-year event
1051	25-year event
1070	50-year event
1079	100-year event
2494	Bankfull flow

Table 3.23. Summary of the HEC-RAS 1D results for steady flow simulations.

Discharge (m ³ /s)	Stage (m)	Velocity (m/s)	Shear Stress (N/m ²)
203	3.86	0.96	1.91
997	8.26	1.58	3.96
1051	8.49	1.6	4.03
1070	8.59	1.6	4.03
1079	8.56	1.62	4.14
2494	10.04	2.99	13.4

As with the other bridge crossings, the results from the SRH-2D model were normalized against the 1D value and the distance was normalized over the water surface elevation width.

Figure 3-50 illustrates the comparison of the 2D and 1D values of stage at the bankfull flow (2494 m³/s) for the Roanoke River. The other results can be found in Appendix A. The general trend for the stage results was that the 2D model over predicted compared to the 1D model for the in-channel depths and the maximum stage occurred near the left pier. A comparison of the median and maximum values of normalized depth versus discharge can be seen in figure 3-51. The normalized values approach one for the medium water discharges. This indicates that the 1D and 2D results for depth are most similar at this range of flows.

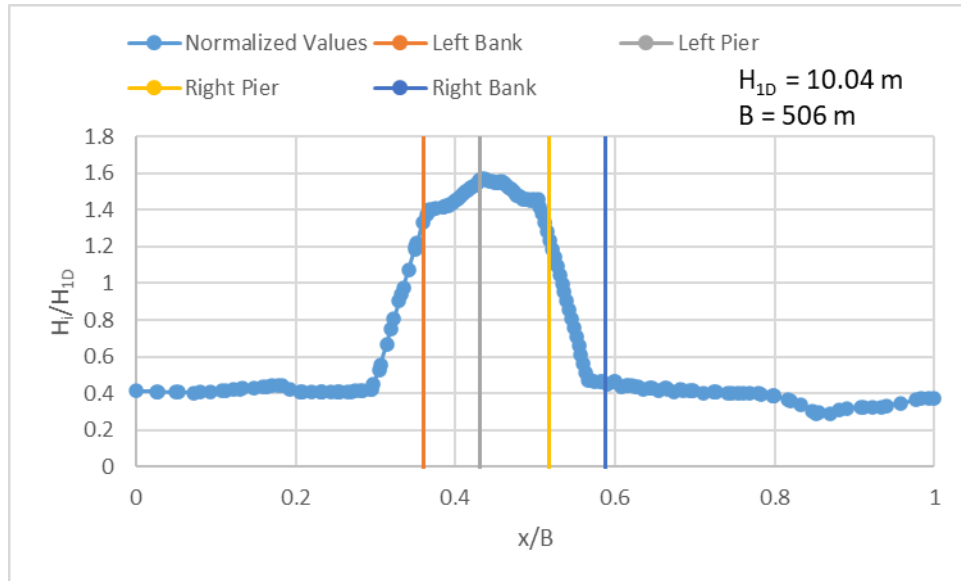


Figure 3-50. The normalized values of stage at the bankfull flow of Roanoke River.

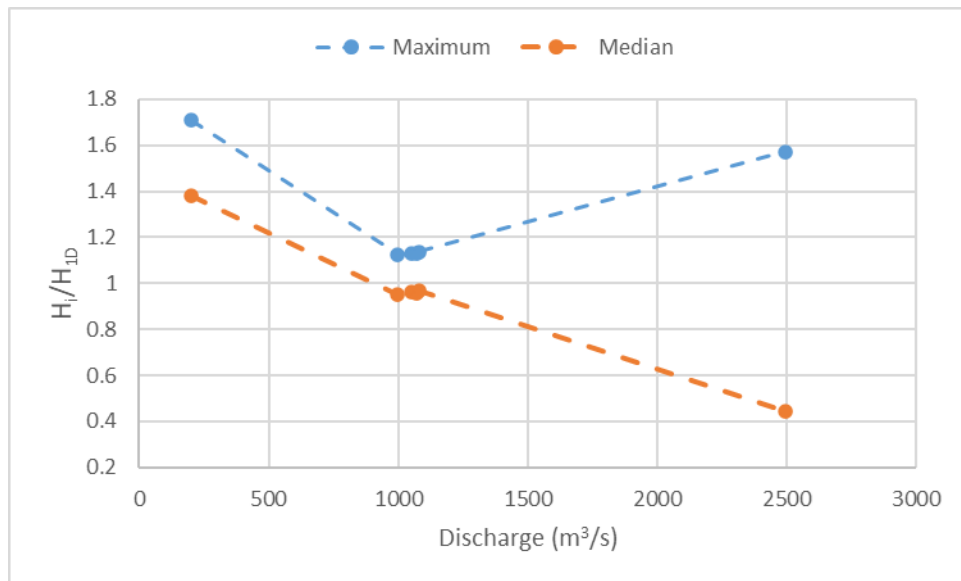


Figure 3-51. A comparison of the maximum and median normalized depths at Roanoke River.

Figure 3-52 shows the velocity distribution at the bankfull flow of the Roanoke River.

The trend across the six flows was that the velocity was lower at the piers than in the surrounding areas. A comparison of the median and maximum values of normalized velocities versus discharge can be seen in figure 3-53. Like with the depth, the values approach one at the middle

range of flows meaning that the 1D and 2D results were similar. At the lower and higher flows, however; most of the 2D values are less than half that of the 1D value of velocity.

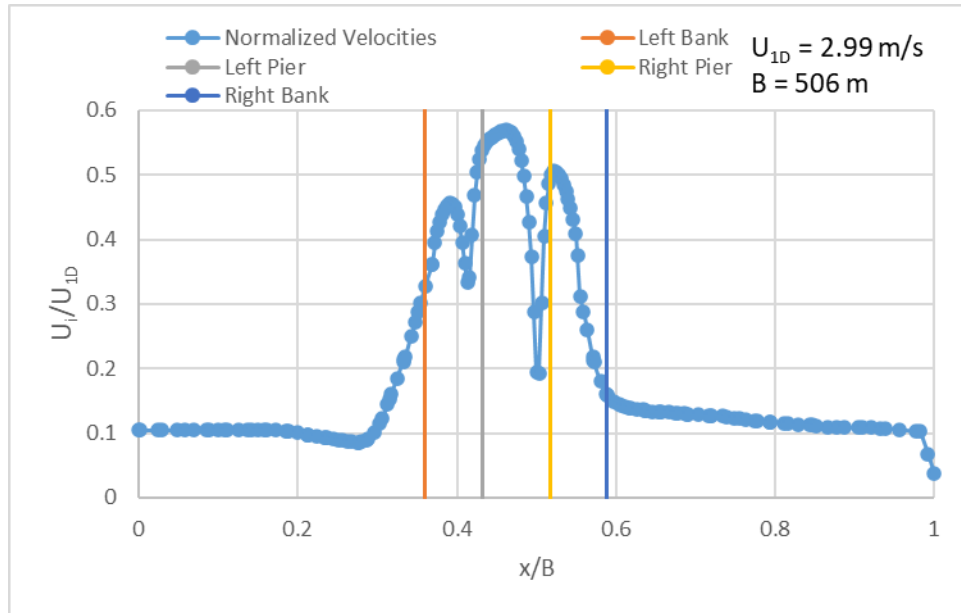


Figure 3-52. The normalized values of velocity at the bankfull flow of Roanoke River.

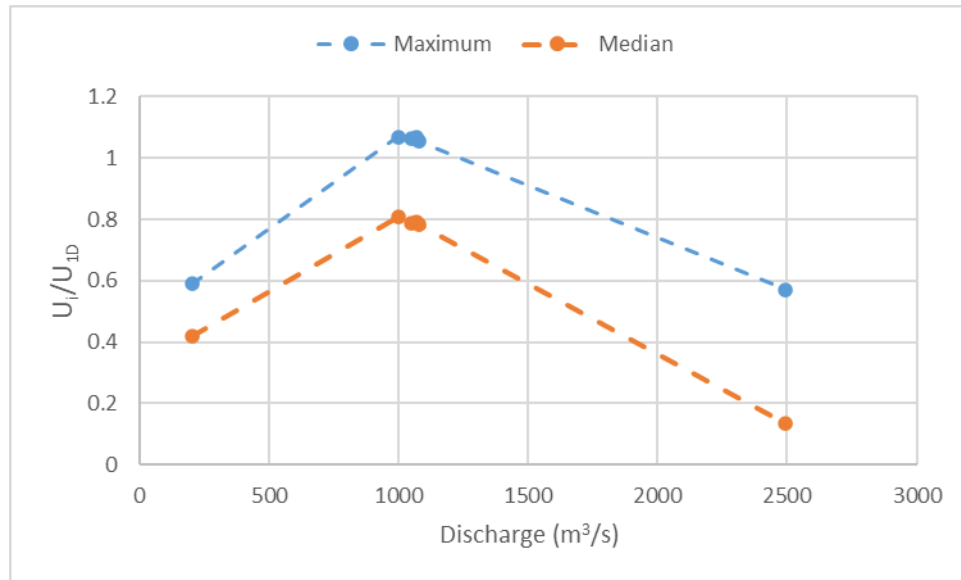


Figure 3-53. A comparison of the maximum and median normalized velocities at Roanoke River.

Figure 3-54 shows the normalized shear stress distribution at bankfull flow. The trend was that the maximum shear stress occurred along the left bank and the minimum values were

near the piers. Most of the values produced in SRH-2D were greater than the HEC-RAS 1D value. A comparison of the median and maximum values of normalized shear stresses versus discharge can be seen in figure 3-55. Unfortunately, due to technical issues with SRH-2D shear stress was only computed at two water discharges. Because of this, an accurate relationship cannot be inferred.

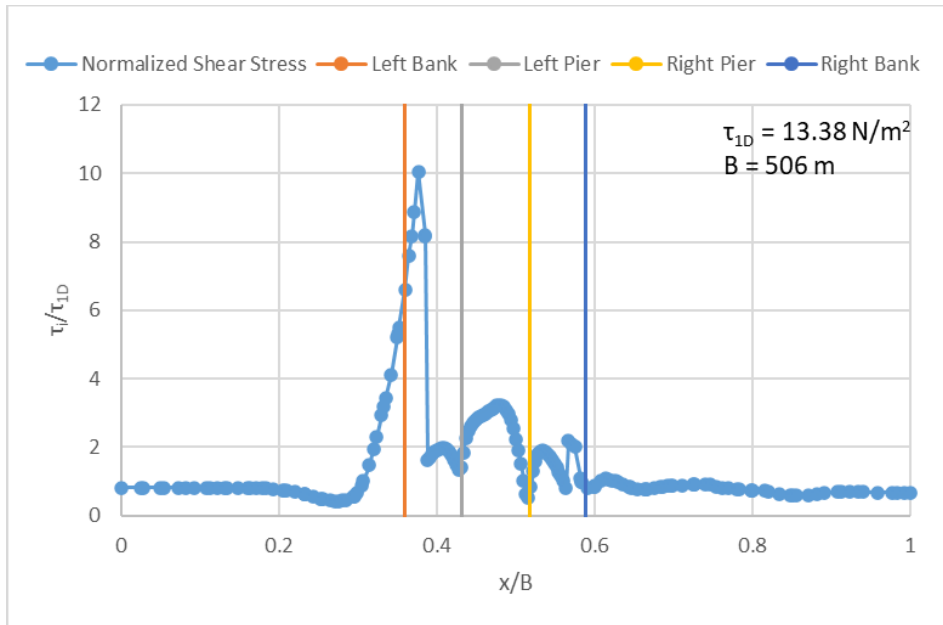


Figure 3-54. The normalized values of shear stress at bankfull at the Roanoke River.

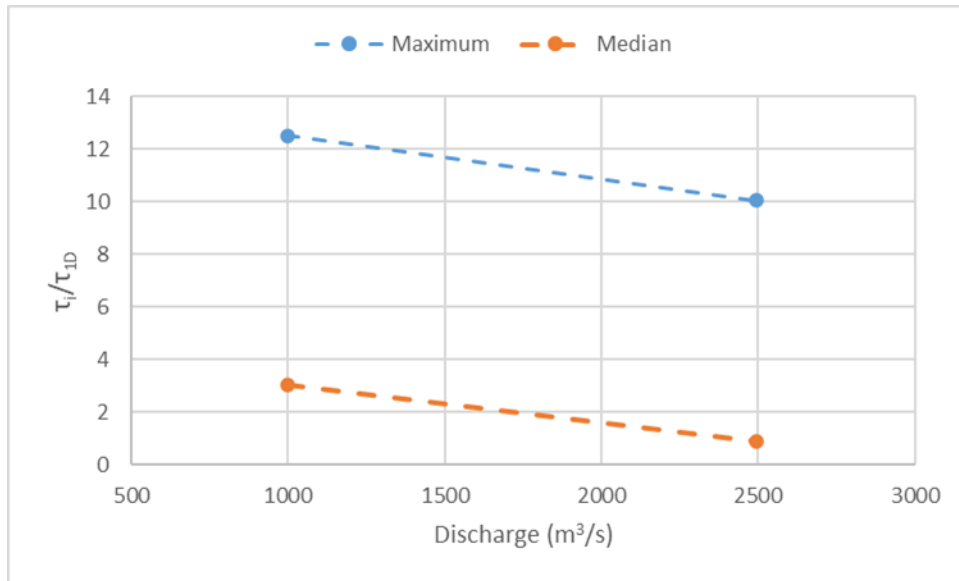


Figure 3-55. A comparison of the maximum and median normalized shear stresses at the Roanoke River.

Scour Depth Predictions

The same procedure from Ellerbe Creek was done at the Roanoke River to obtain scour depths in the 2D model. These results in comparison with the 1D pier scour depths can be seen in table 3.24. In contrast with the results from Ellerbe Creek, at Roanoke River the 1D scour depths were greater with respect to the pier diameter than the 2D values.

Table 3.24. Comparison of 1D and 2D pier scour estimates for the Roanoke River.

Discharge (m ³ /s)	Y _{s/a} HEC-RAS (1D)	Y _{s/a} Fixed-Bed (2D)	Y _{s/a} Mobile-Bed (2D)
203	0.92	1.14	1.77
997	1.14	1.93	2.24
1051	1.15	1.89	2.07
1070	1.15	1.88	2.24
1079	1.58	1.86	2.25
2494	1.53	1.84	1.98

3.4.5 Comparison of Bridge Crossings

Hydraulic Characterization

Because the data were normalized against the water surface widths, comparisons between the four bridge crossings can be drawn. For the stage, there is a trend that three of the sites rarely meet or exceed the HEC-RAS 1D value. The exception is the Roanoke River bridge crossing, which for most of the discharges the SRH-2D prediction was higher than the HEC-RAS 1D output (figure 3-56). For most bridge crossings, the normalized values have a slight decrease as water discharge increased. With the exception being the Tar River bridge crossing, which implies that the floodplain is narrow therefore stage does not decrease with increasing water discharge. This was supported by field observation of an urban area surrounding the river.

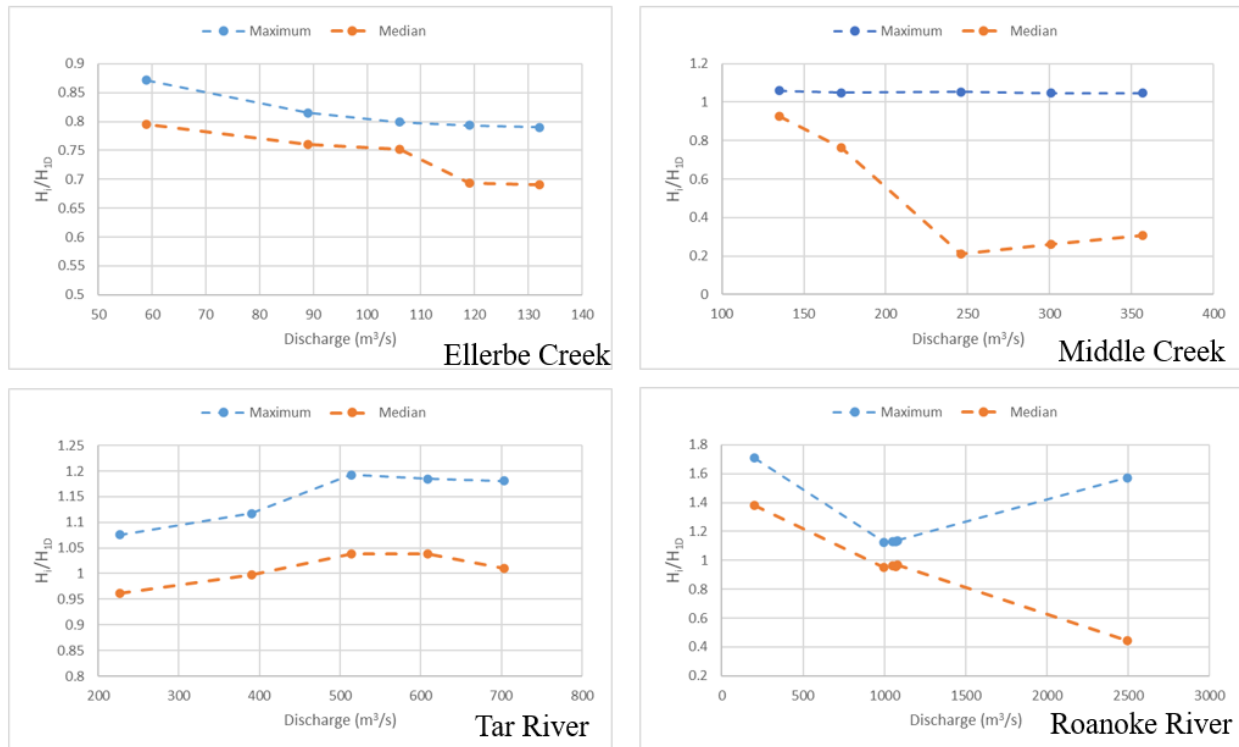


Figure 3-56. All four plots of stage maximum and median values for the bridge crossings.

A pattern can also be observed in the velocity data across the four sites (figure 3-57). At both Ellerbe Creek and Middle Creek, the maximum 2D computed velocities tend to be significantly greater than the 1D value, but in Tar River and Roanoke River the maximum 2D values are approximately one or less than one. The Ellerbe Creek model is the only one that consistently in which the 2D values were greater than the 1D for every evaluated discharge. In fact, all four bridge crossings have distinct patterns across the discharges. The Roanoke River has the largest range of values in the median and maximum. At the highest discharge, which for the Roanoke is the bankfull discharge, the 2D model was significantly less than the 1D model's value. A smaller velocity could be a result of water topping the banks and being less concentrated in the channel.

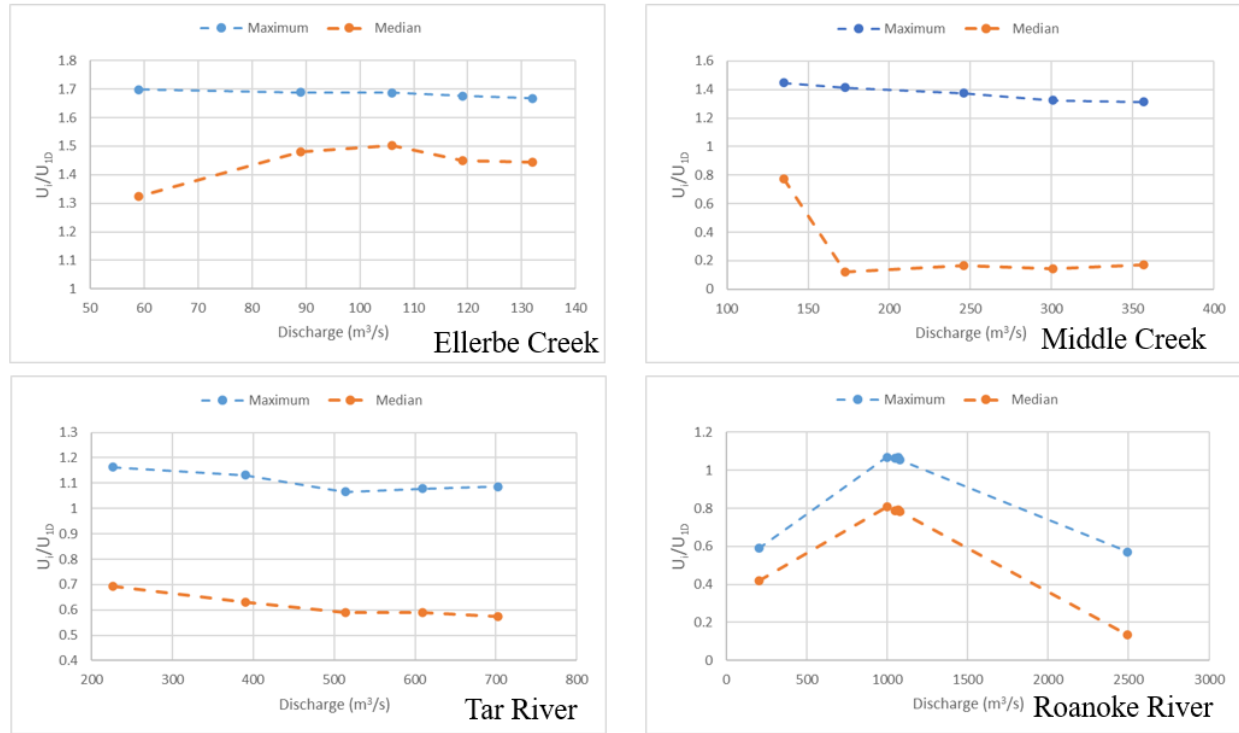


Figure 3-57. All four plots of velocity maximum and median values for the bridge crossings.

Lastly, a trend can also be drawn from the shear stress results (figure 3-58). There appears to be more variability in the shear stress distribution than in the stage or velocity. The Roanoke River once again is the only site that consistently predicted values greater than the 1D value. At Ellerbe Creek the maximum and median values converged as water discharge increased, but at Middle Creek the values diverged. At Tar River and Roanoke River the difference between these values remained approximately the same.

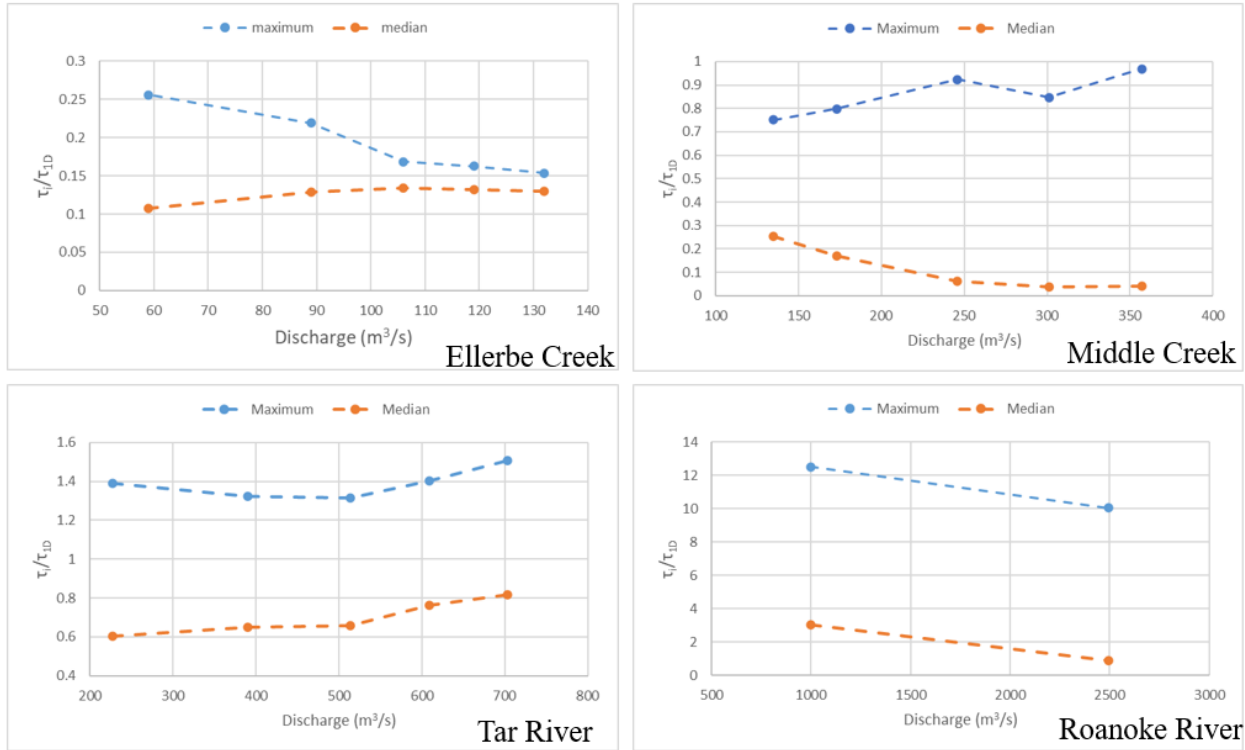


Figure 3-58. All four plots of shear stress maximum and median values for the bridge crossings.

Scour Depth Comparison

The 2D fixed-bed and mobile-bed approaches scour depth results for each bridge crossing at the evaluated water discharges were normalized against the 1D value (Figure 3-59). The 1D values used in the normalization can be seen in table 3-25 through table 3-28. For Ellerbe Creek and Tar River, the normalized values for both the fixed- and mobile-bed approaches stayed within 0.8 and 0.9 across the range of water discharges. For Middle Creek and Roanoke River, all the values are greater than one meaning that the 2D values were greater than the 1D value. The most variability between the fixed- and mobile-bed scour values occurred at low discharges on the Roanoke River. This implies that enough sediment was transported to change the shape of the channel-bed enough to affect the depth and velocity at the approach cross-section.

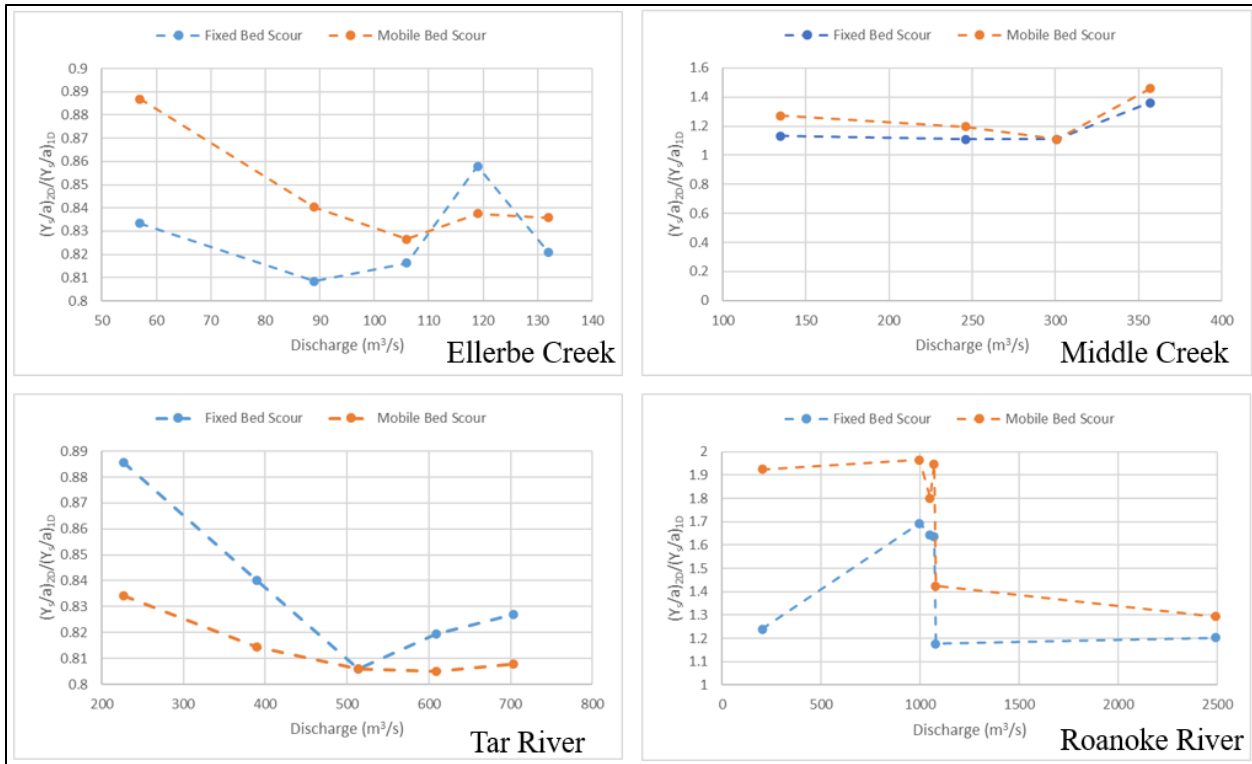


Figure 3-59. Comparison of normalized scour depth predictions for each bridge crossing.

Table 3.25. The 1D HEC-18 produced values of pier scour used for normalization for Ellerbe Creek.

Discharge (m^3/s)	1D Y_s/a
57	1.68
89	1.88
106	1.96
119	1.97
132	2.01

Table 3.26. The 1D HEC-18 produced values of pier scour used for normalization for Middle Creek.

Discharge (m ³ /s)	1D Y _{s/a}
135	1.91
173	2.02
246	2.19
301	2.27
357	1.88

Table 3.27. The 1D HEC-18 produced values of pier scour used for normalization for Tar River.

Discharge (m ³ /s)	1D Y _{s/a}
227	1.75
390	1.94
514	2.01
609	2.05
703	2.08

Table 3.28. The 1D HEC-18 produced values of pier scour used for normalization for Roanoke River.

Discharge (m ³ /s)	1D Y _{s/a}
203	0.92
997	1.14
1051	1.15
1070	1.15
1079	1.58

3.5 Conclusions

The objective of this chapter was to compare the relative performance of 1D and 2D process-based numerical models when resolving the flow variables that are used as input for the application of the HEC-18 equation. Specifically, the flow variables were solved using three different approaches: HEC-RAS 1D with hydrodynamic module only (i.e., fixed-bed approach); SRH-2D with hydrodynamic module only (i.e., 2D fixed-bed approach); and SRH-2D with both hydrodynamic and morphodynamic modules (i.e., 2D mobile-bed approach).

The three hydraulic variables analyzed (stage, velocity, and shear stress) were normalized against the 1D values to allow for comparisons to be drawn. For the stage, the trend was that three of the bridge crossings rarely exceed the HEC-RAS 1D value. The exception was the Roanoke River bridge crossing in which the 2D values were higher than the 1D values. Another trend with the stage was that the values tend to decrease as water discharge increased. The exception was the Tar River bridge crossing. This trend could be explained by the width of the floodplains. For example, the floodplain at the Tar River bridge crossing was narrow which implies that the water does not extend over the floodplains and thus stage does not decrease with

increasing water discharge. For the velocity values, the Ellerbe and Middle Creek bridge crossings tended to have higher maximum values than the Roanoke and Tar River bridge crossings. A smaller velocity for the bigger rivers could be a result of water topping over the banks and being less concentrated in the channels. For the shear stress plots, there appears to be more variability in the distribution. For example, at the Ellerbe Creek bridge crossing, the median and maximum values converged, but at the Middle Creek bridge crossing the values diverged.

Comparisons can also be drawn in the scour depth comparisons. For the Ellerbe Creek and Tar River bridge crossings, the normalized values for both 2D approaches were less than one, however, for the other sites, the values were greater than one. The most variability between the two 2D approaches occurred for the Roanoke River bridge crossing meaning that enough sediment was transported to change the shape of the channel-bed enough to affect the depth and velocity at the approach cross-section.

The trends that were observed in these data across stage, velocity, and shear stress can lead to a better understanding of hydraulic principles in modeling. Because all the bridge crossings have different river characteristics such as range of discharges and widths and different bridge geometries, but still performed similarly that means there are underlying hydraulic principles driving the results. The SRH-2D results were, for the most part, all like the HEC-RAS 1D results even though the model parameters (i.e., Manning's roughness) were different. This is a good indication of the models' accuracy. Future work could include modeling bridges and streams of the same sizes to determine if there are similarities.

CHAPTER 4: CONCLUSIONS

In this thesis, two FO prototypes were tested in the lab and eventually one of those was tested in the field. The advantage of prototype 1 was that it had increased vertical resolution; however, the construction of the device was more laboring and because the heating cable was wrapped on top of the FO cable there is more chance of the FO cable being distorted. The main advantage of prototype 2 was that the FO cable was sturdier than prototype 1 and had the heating cable built inside the armoring; however, the vertical resolution was nearly half that as prototype 2. The error stabilized after less time of heating for prototype 2 which also means that more experiments can be done in the same amount of time as prototype 1.

After each test was completed, it was decided that the field device should be constructed using the same materials as that of prototype 2. The FO cable used for the field device had to be very durable against floating debris and animals. The device was tested one day in the field with promising results so far. The error was 1 to 2 cm which was similar to the error in the lab tests.

This work could have been improved by minimizing difference between the prototype experiments, for example using the same DTS and same heat pulse durations. Even though there were some differences, the results were able to be compared for this thesis.

Each of the experiments proved that the sand-water interface and air-water interface could be discerned using the developed algorithm, however there is some error in this measurement. This measurement error is mostly due to the observed gradient in the interface around the device. This research should be seen as a proof of concept that the FO-DTS method can indeed detect scour under ranges of flow, with different device construction, under laboratory and field conditions. FO-DTS has the potential of being a better way to measure bridge pier scour because of its superior durability and proven accuracy. This research expands

on current monitoring techniques of bridge pier scour in hopes of learning how to better predict and prevent scour.

The objective of the modeling chapter was to compare the relative performance of 1D and 2D process-based numerical models when resolving the flow variables that are used as input for the application of the HEC-18 equation. Specifically, the flow variables were solved using three different approaches: HEC-RAS 1D with hydrodynamic module only (i.e., fixed-bed approach); SRH-2D with hydrodynamic module only (i.e., 2D fixed-bed approach); and SRH-2D with both hydrodynamic and morphodynamic modules (i.e., 2D mobile-bed approach). Overall, the 1D and 2D models performed well. The results were similar in most cases for all the outputs. This was expected, especially for scour depths, because a similar procedure or equation was used in both approaches.

The trends that were observed in these data across stage, velocity, and shear stress can lead to a better understanding of hydraulic principles in modeling. Because all the bridge crossings have different river characteristics such as range of discharges and widths and different bridge geometries, but still performed similarly that means there are underlying hydraulic principles driving the results. The SRH-2D results were, for the most part, all like the HEC-RAS 1D results even though the model parameters (i.e., Manning's roughness) were different. This is a good indication of the models' accuracy. Future work could include modeling bridges and streams of the same sizes to determine if there are similarities.

Having accurate measurements of real-time pier scour at one of the modeled sites will allow one to determine the accuracy of the models' predictions as well as potentially discover new patterns in how scour develops. Future work should include continuing to monitor the field installation and performing simulations in the models to match the conditions in which

measurements were taken to determine the models' accuracy. If information on how scour holes develop is learned, that information could then be applied to other bridge crossings in the future.

REFERENCES

- Arneson, L. A., Zevenbergen, L. W., Lagasse, P. F., & Clopper, P. E. (2012). Evaluating scour at bridges (HEC-18). *Technical Rep. No. FHWA (Federal Highway Administration)* HIF-12, 3.
- B&K Precision Corp., USA. Model 9205, Multi-Range Programmable DC Power Supplies - B&K Precision. Retrieved from <https://www.bkprecision.com/products/power-supplies/9205-600w-multi-range-60v-25a-dc-power-supply.html>
- Brownlie, W. R. (1983). Flow depth in sand-bed channels. *Journal of Hydraulic Engineering*, 109(7), 959-990.
- Brunner, G. W. (2016). HEC-RAS River Analysis System, 2D Modeling User's Manual Version 5.0. US Army Corps of Engineers Institute for Water Resources Hydrologic Engineering Center (HEC).
- Chang, W. Y., Lai, J. S., & Yen, C. L. (2004). Evolution of scour depth at circular bridge piers. *Journal of Hydraulic Engineering*, 130(9), 905-913.
- Cheng, Y., Sayde, C., Li, Q., Basara, J., Selker, J., Tanner, E., & Gentine, P. (2017). Failure of Taylor's hypothesis in the atmospheric surface layer and its correction for eddy-covariance measurements. *Geophysical Research Letters*, 44, 4287-4295.
- Dakin, J. P., Pratt, D. J., Bibby, G. W., & Ross, J. N. (1985). Distributed optical fibre Raman temperature sensor using a semiconductor light source and detector. *Electronics letters*, 21(13), 569-570.
- DeBell, T. C. (2021). A Novel Approach to High-Resolution Monitoring of Subsurface Water Dynamics in Media Based Treatment Practices. Master of Science Thesis. North Carolina State University. Raleigh, NC.

Deng, L., & Cai, C. S. (2009). Bridge scour: Prediction, modeling, monitoring, and countermeasures. *Practice Periodical on Structural Design and Construction*, 15(2), 125-134.

Doll, B. A., Wise-Frederick, D. E., Buckner, C. M., Wilkerson, S. D., Harman, W. A., Smith, R. E., & Spooner, J. (2002). Hydraulic geometry relationships for urban streams throughout the Piedmont of North Carolina, *JAWRA Journal of the American Water Resources Association*, 38(3), 641-651.

Doll, B. A., Dobbins, A. D., Spooner, J., Clinton, D. R., & Bidelsbach, D. A. (2003). Hydraulic geometry relationships for rural North Carolina coastal plain streams. NC Stream Restoration Institute, Report to NC Division of Water Quality for, 319(11).

Dong, J., Steele-Dunne, S.C., Ochsner, T.E., Hatch, C.E., Sayde, C., Selker, J., Tyler, S., Cosh, M.H. & van de Giesen, N. (2016). Mapping high-resolution soil moisture and properties using distributed temperature sensing data and an adaptive particle batch smoother, *Water Resources Research*, 52, 7690-7710.

Fisher, M., Chowdhury, M. N., Khan, A. A., & Atamturktur, S. (2013). An evaluation of scour measurement devices. *Flow Measurement and Instrumentation*, 33, 55-67.

Froehlich, D. C., & Fisher, P. F. (2000). Storm surge scour at coastal bridges: documenting the effects of hurricanes Bonnie and Floyd in North Carolina. In *Building Partnerships* (pp. 1-10).

Lai, Y. G. (2008). SRH-2D version 2: Theory and User's Manual- Sedimentation and River Hydraulics- Two-Dimensional River Flow Modeling. *Bureau of Reclamation*.

Lai, Y. G., & Greimann, B. P. (2008). Predicting Contraction Scour with a 2D Model. In *World Environmental and Water Resources Congress 2008: Ahupua'a* (pp. 1-11).

- Lai, Y. G. (2017). Modeling stream bank erosion: Practical stream results and future needs. *Water*, 9(12), 950.
- Landers, M. N., & Mueller, D. S. (1996). Evaluation of selected pier-scour equations using field data. *Transportation Research Record*, 1523(1), 186-195.
- Lin, Y. B., Chen, J. C., Chang, K. C., Chern, J. C., & Lai, J. S. (2005). Real-time monitoring of local scour by using fiber Bragg grating sensors. *Smart materials and structures*, 14(4), 664.
- Petrie, J., Diplas, P., Gutierrez, M., & Nam, S. (2013). Combining fixed-and moving-vessel acoustic Doppler current profiler measurements for improved characterization of the mean flow in a natural river. *Water Resources Research*, 49(9), 5600-5614.
- Rouhnia, M. (2016). Vertical Transport of Sediment from Muddy Buoyant River Plumes in the Presence of Different Modes of Interfacial Instabilities (Doctoral dissertation, Virginia Tech).
- Sayde, C., Gregory, C., Gil-Rodriguez, M., Tufillaro, N., Tyler S., van de Giesen, N., English, M., Cuénca, R., & Selker, J.S. (2010). Feasibility of soil moisture monitoring with heated fiber optics, *Water Resour. Res.*, 46, W06201.
- Sayde, C., Thomas, C. K., Wagner, J., & Selker, J. (2015). High-resolution wind speed measurements using actively heated fiber optics. *Geophysical Research Letters*, 42(22), 10-064.
- Sebok, E., Duque, C., Engesgaard, P., & Boegh, E. (2015). Application of Distributed Temperature Sensing for coupled mapping of sedimentation processes and spatio-temporal variability of groundwater discharge in soft-bedded streams. *Hydrological Processes*, 29(15), 3408-3422.

- Selker, J. S., Thévenaz, L., Huwald, H., Mallet, A., Luxemburg, W., Van De Giesen, N., ... & Parlange, M. B. (2006). Distributed fiber-optic temperature sensing for hydrologic systems. *Water Resources Research*, 42(12).
- Teledyne Marine. (n.d.). RiverRay ADCP. ProductPage. Retrieved October 19, 2021, from <http://www.teledynemarine.com/riverray-adcp?ProductLineID=13>.
- Tyler, S. W., Selker, J. S., Hausner, M. B., Hatch, C. E., Torgersen, T., Thodal, C. E., & Schladow, S. G. (2009). Environmental temperature sensing using Raman spectra DTS fiber-optic methods. *Water Resources Research*, 45(4).
- U.S. Bureau of Reclamation. (2019). *SRH-2D*. <https://www.usbr.gov/tsc/techreferences/computer%20software/models/srh2d/index.html>
- van Rijn, L. C., Walstra, D. J., Grasmeijer, B., Sutherland, J., Pan, S., & Sierra, J. P. (2003). The predictability of cross-shore bed evolution of sandy beaches at the time scale of storms and seasons using process-based profile models. *Coastal Engineering*, 47(3), 295-327.
- Yu, X., & Yu, X. B. (2008). 1D and 2D hydraulic simulations for bridge scour prediction: A comparative study. In Proceedings 4th International Conference on Scour and Erosion (ICSE-4). November 5-7, 2008, Tokyo, Japan (pp. 226-232).

APPENDIX

Appendix A

Ellerbe Creek Hydraulic Results

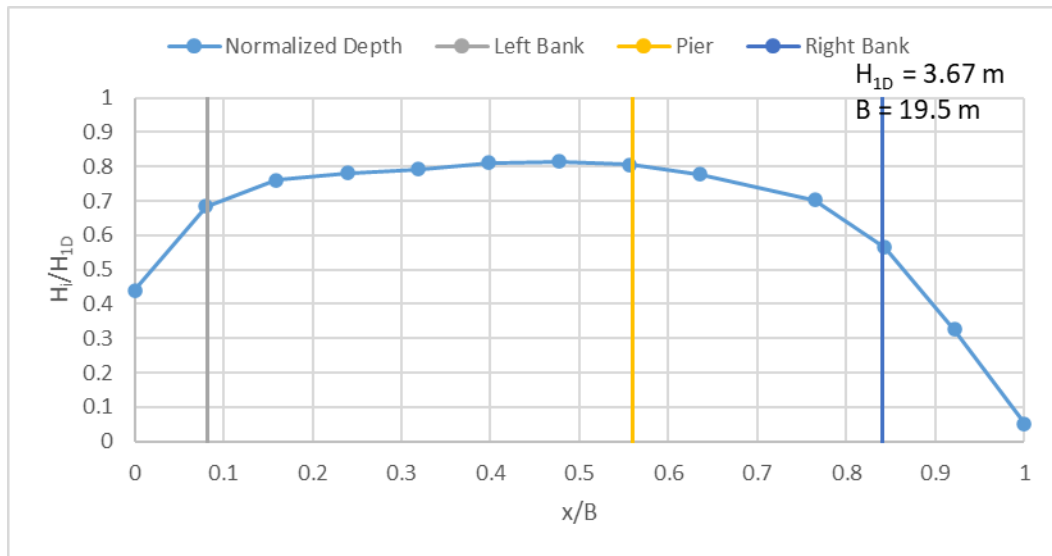


Figure B-1. The depth profile created by SRH-2D for Ellerbe Creek at 89 m³/s.

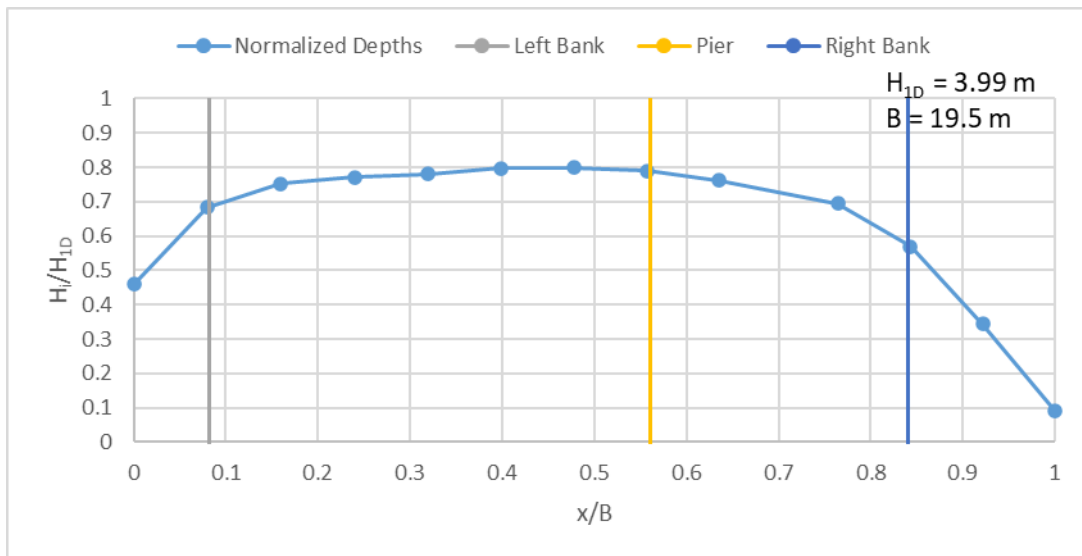


Figure B-2. The depth profile created by SRH-2D for Ellerbe Creek at 106 m³/s.

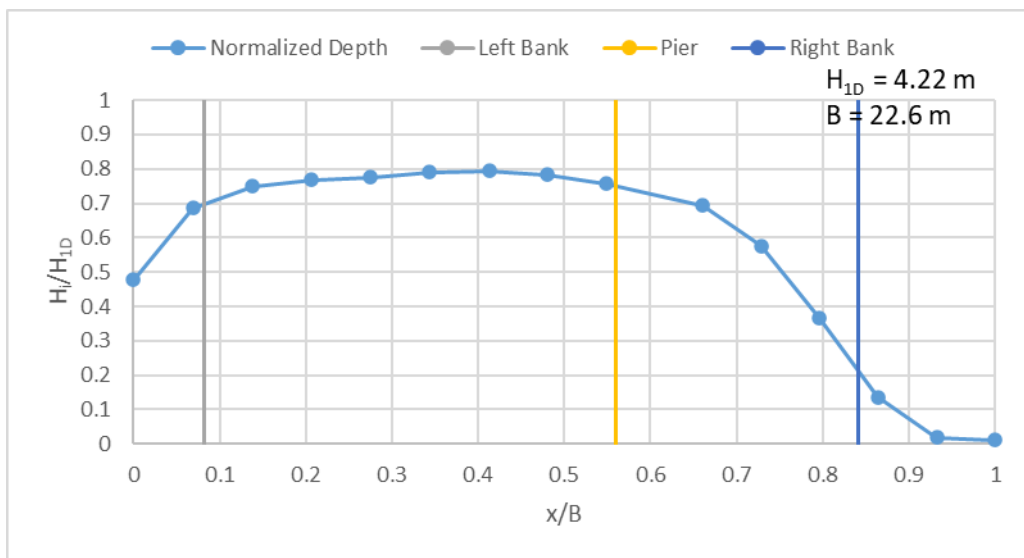


Figure B-3. The depth profile created by SRH-2D for Ellerbe Creek at $119 \text{ m}^3/\text{s}$.

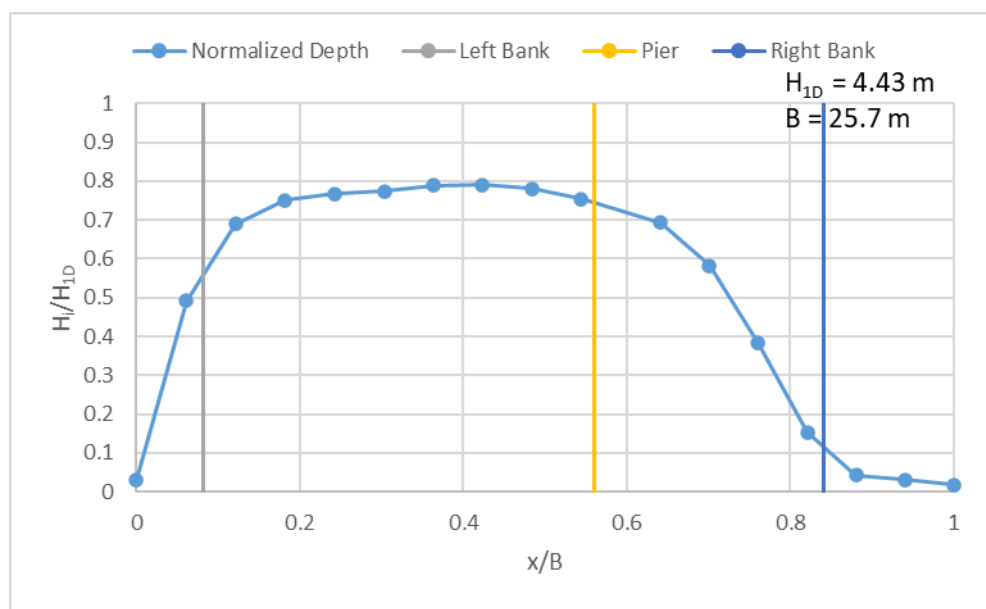


Figure B-4. The depth profile created by SRH-2D for Ellerbe Creek at $132 \text{ m}^3/\text{s}$.

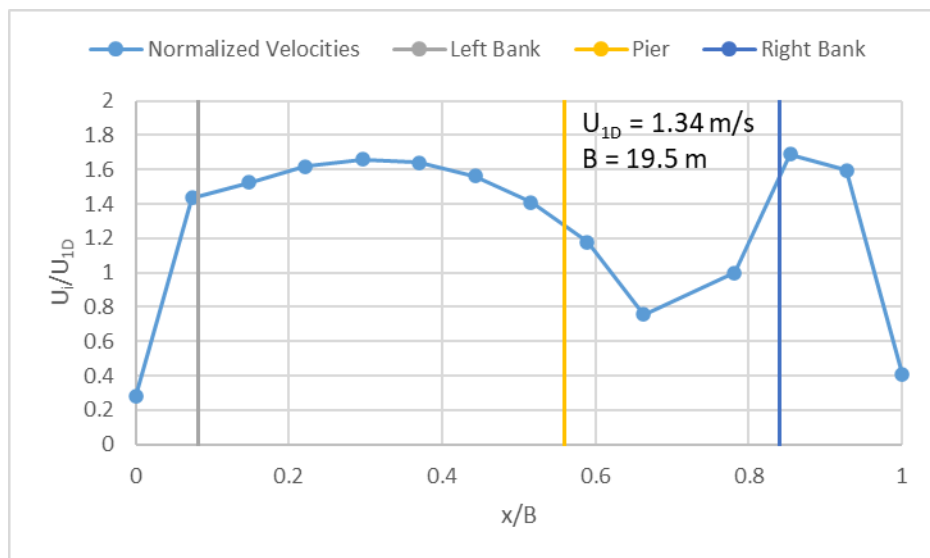


Figure B-5. The velocity profile created by SRH-2D for Ellerbe Creek at $89 \text{ m}^3/\text{s}$.

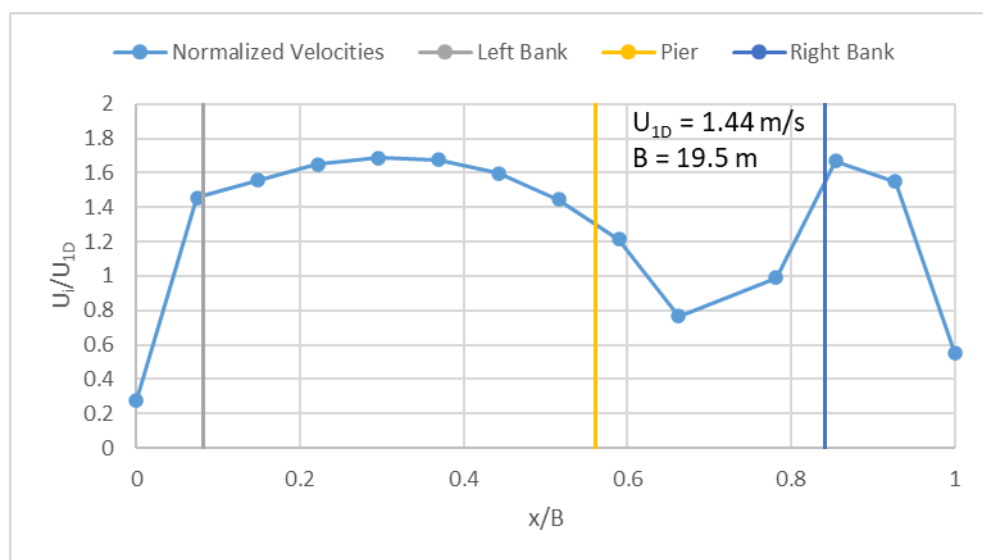


Figure B-6. The velocity profile created by SRH-2D for Ellerbe Creek at $106 \text{ m}^3/\text{s}$.

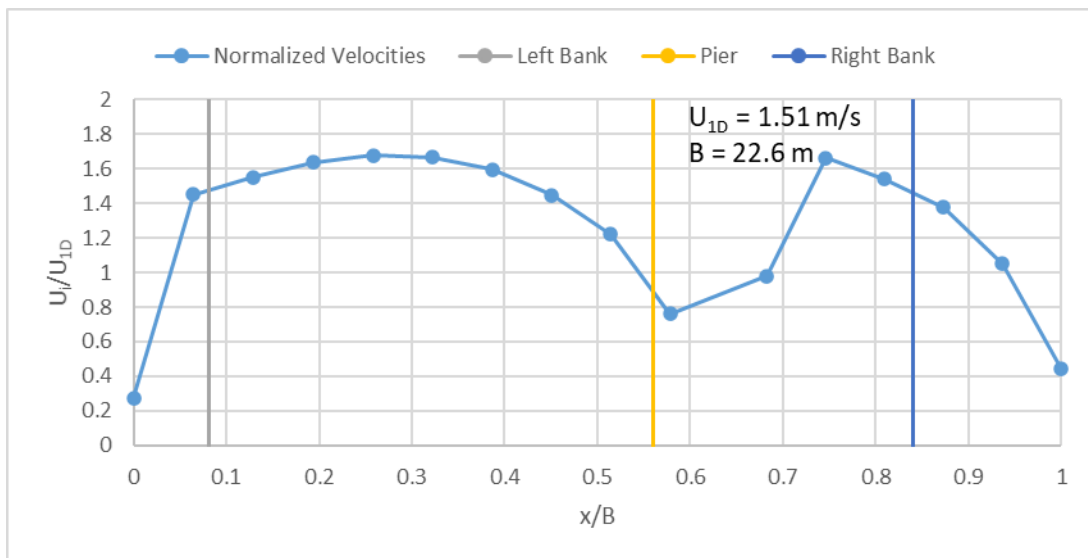


Figure B-7. The velocity profile created by SRH-2D for Ellerbe Creek at $119 \text{ m}^3/\text{s}$.

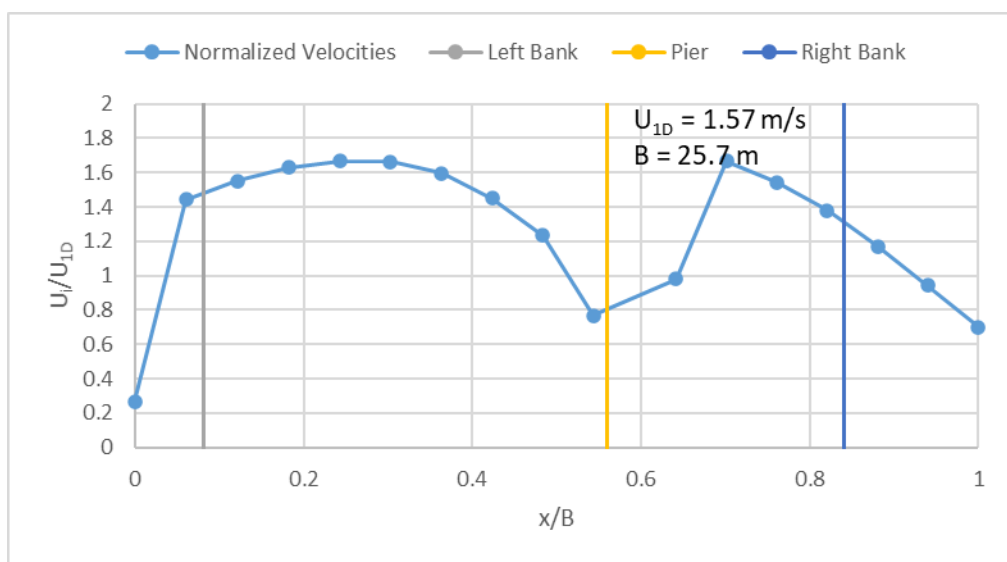


Figure B-8. The velocity profile created by SRH-2D for Ellerbe Creek at $132 \text{ m}^3/\text{s}$.

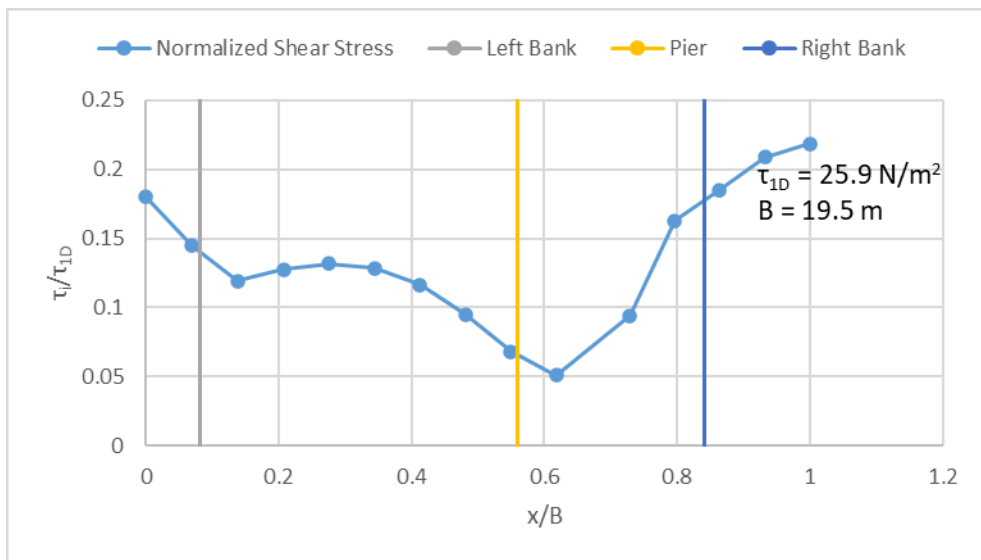


Figure B-9. The shear stress profile created by SRH-2D for Ellerbe Creek at $89 \text{ m}^3/\text{s}$.

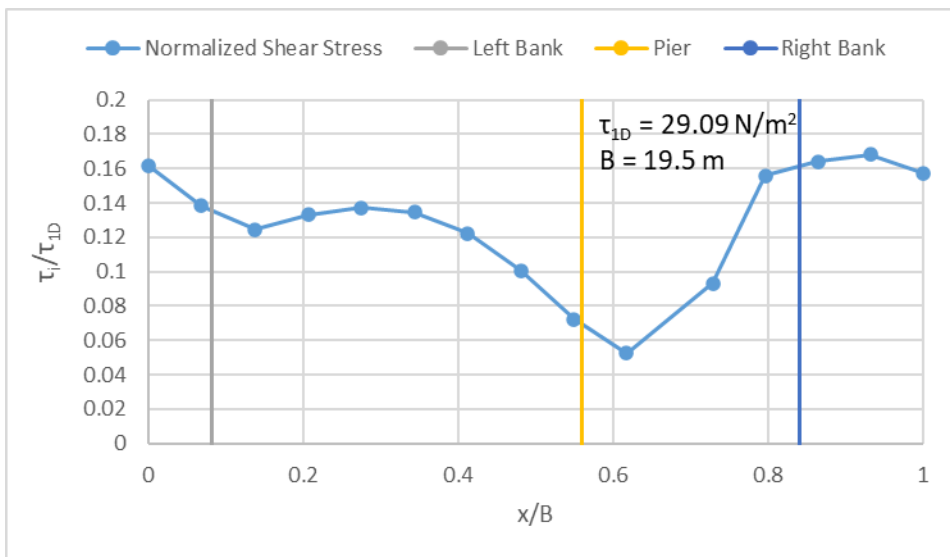


Figure B-10. The shear stress profile created by SRH-2D for Ellerbe Creek at $106 \text{ m}^3/\text{s}$.

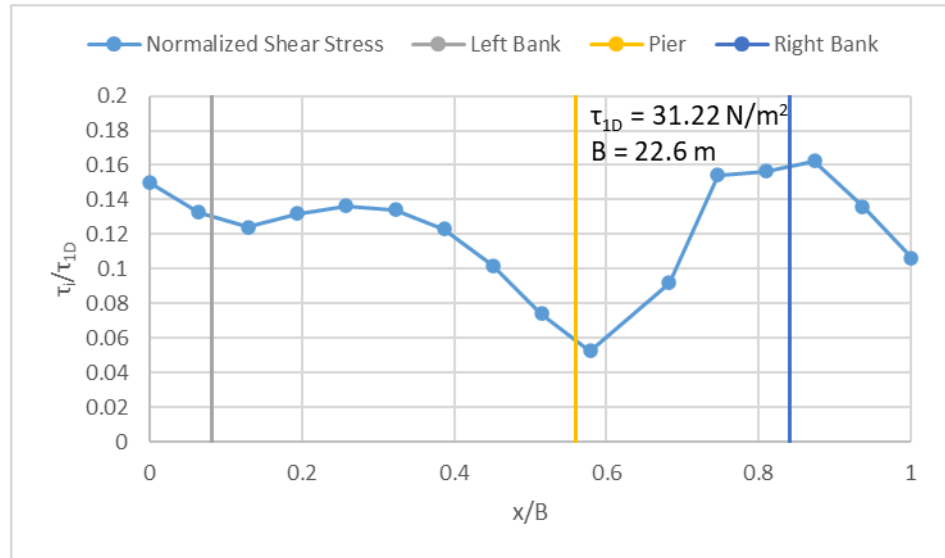


Figure B-11. The shear stress profile created by SRH-2D for Ellerbe Creek at $119 \text{ m}^3/\text{s}$.

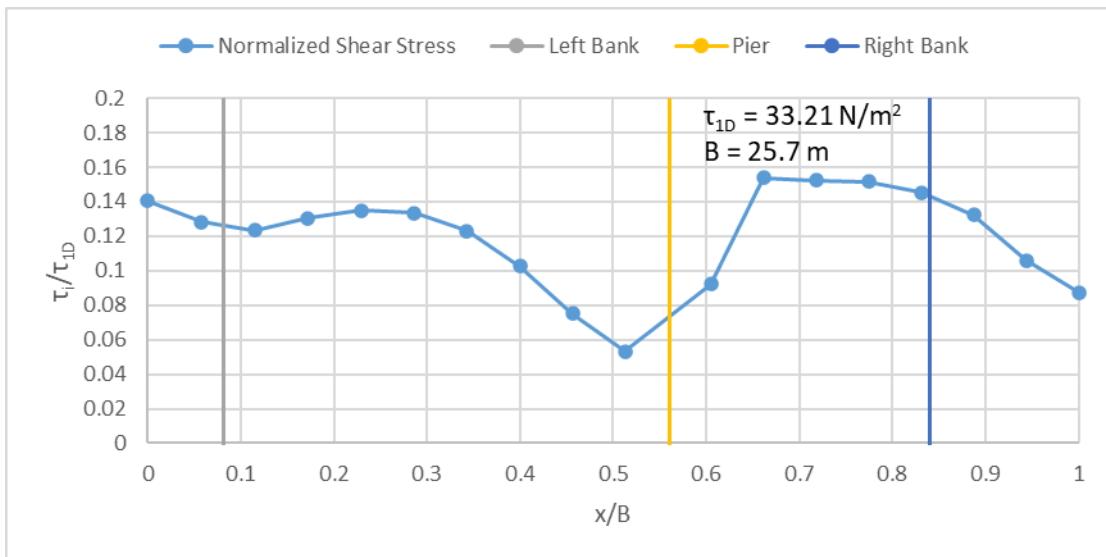


Figure B-12. The shear stress profile created by SRH-2D for Ellerbe Creek at $132 \text{ m}^3/\text{s}$.

Middle Creek Hydraulic Results

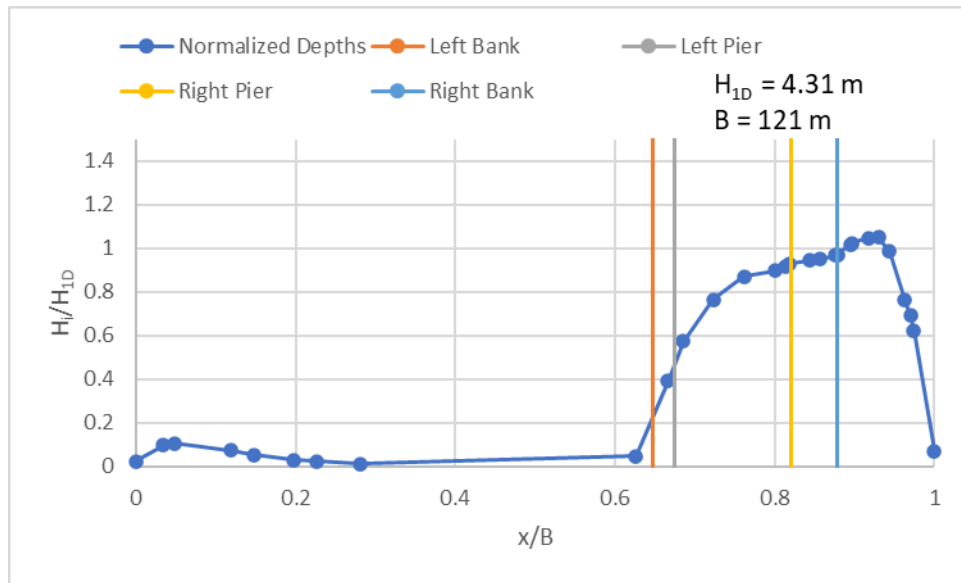


Figure B-13. The depth profile created by SRH-2D for Middle Creek at $173 \text{ m}^3/\text{s}$.

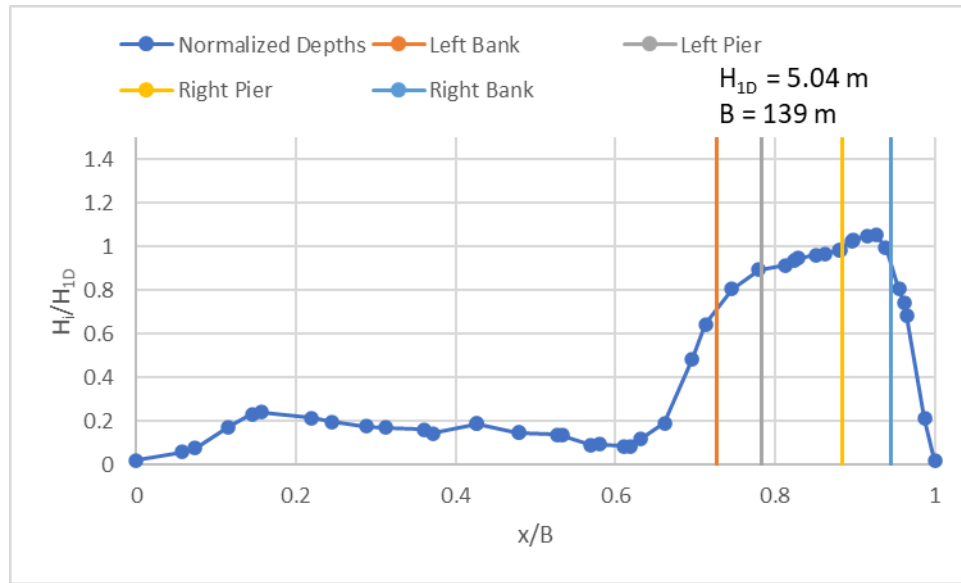


Figure B-14. The depth profile created by SRH-2D for Middle Creek at $246 \text{ m}^3/\text{s}$.

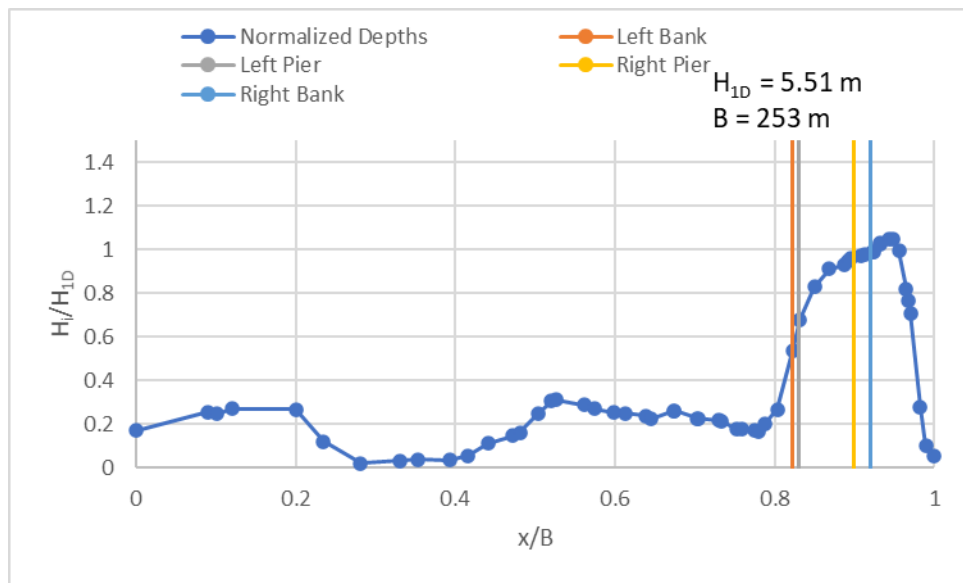


Figure B-15. The depth profile created by SRH-2D for Middle Creek at $301 \text{ m}^3/\text{s}$.

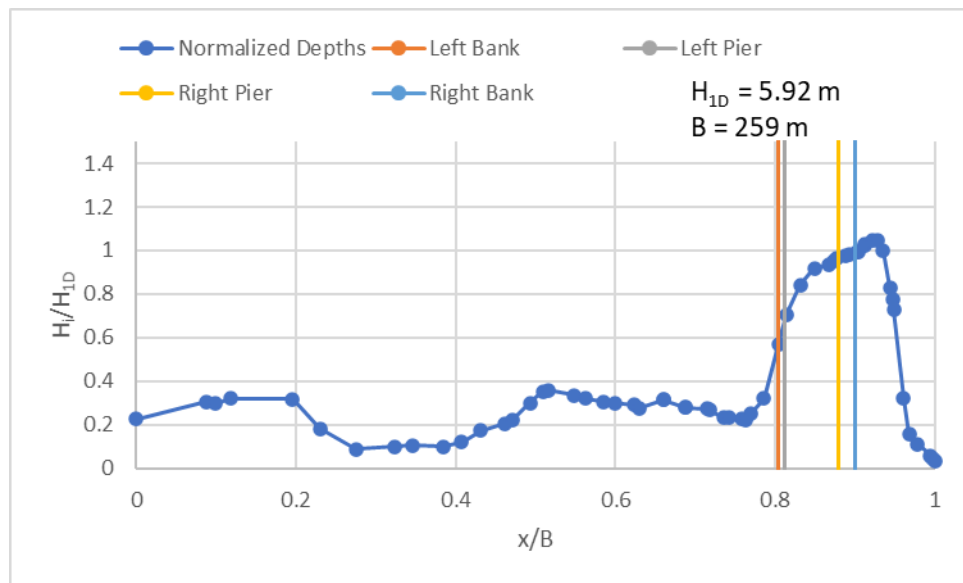


Figure B-16. The depth profile created by SRH-2D for Middle Creek at $357 \text{ m}^3/\text{s}$.

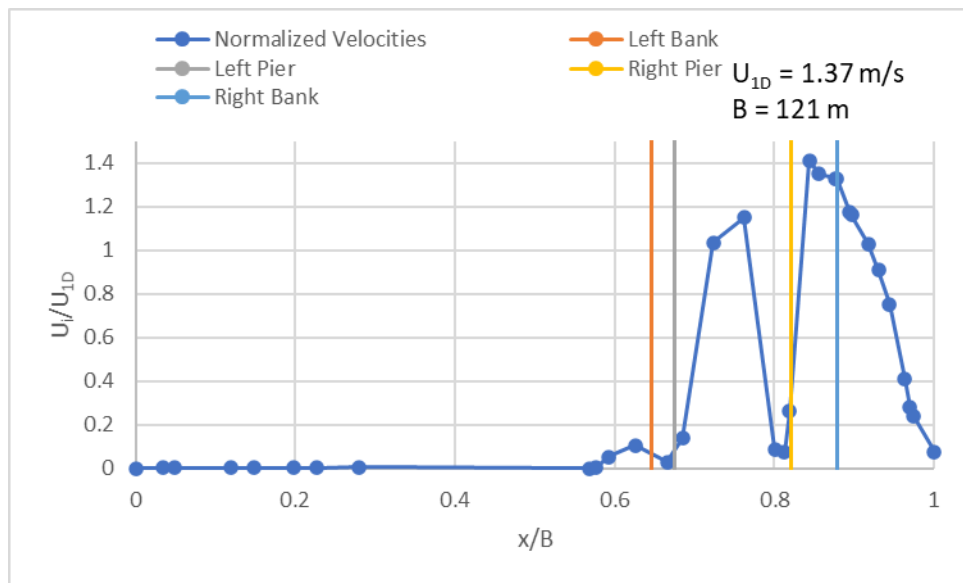


Figure B-17. The velocity profile created by SRH-2D for Middle Creek at $173 \text{ m}^3/\text{s}$.

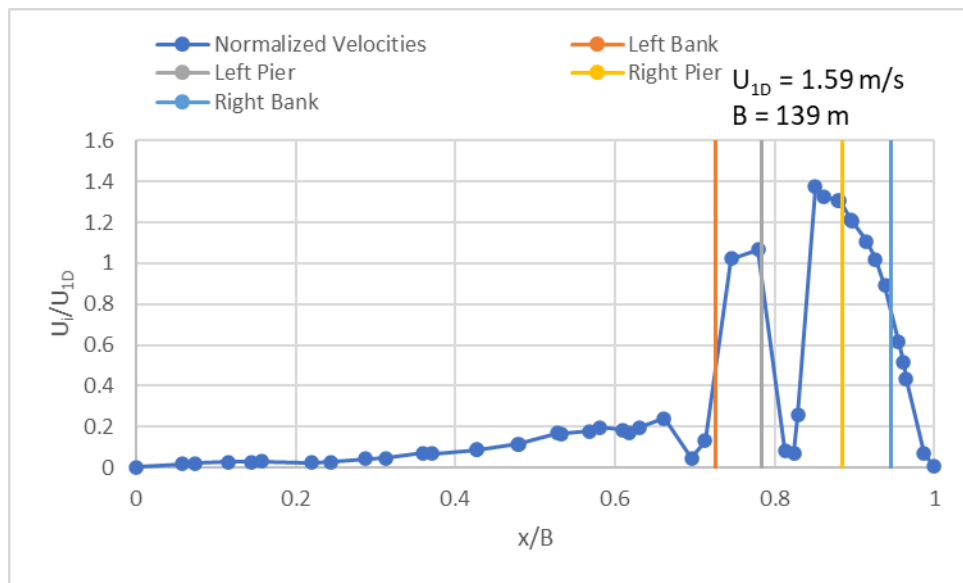


Figure B-18. The velocity profile created by SRH-2D for Middle Creek at $246 \text{ m}^3/\text{s}$.

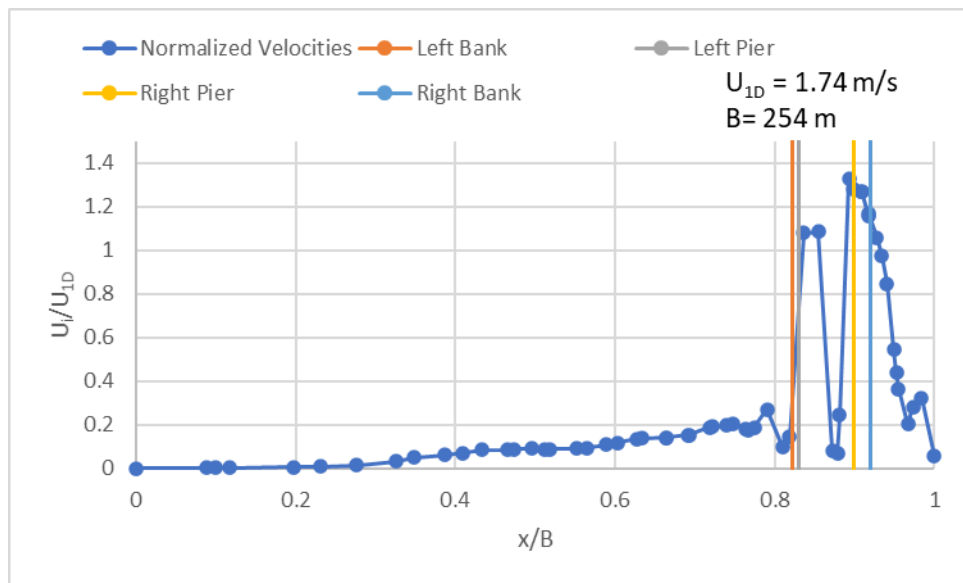


Figure B-19. The velocity profile created by SRH-2D for Middle Creek at $301 \text{ m}^3/\text{s}$.

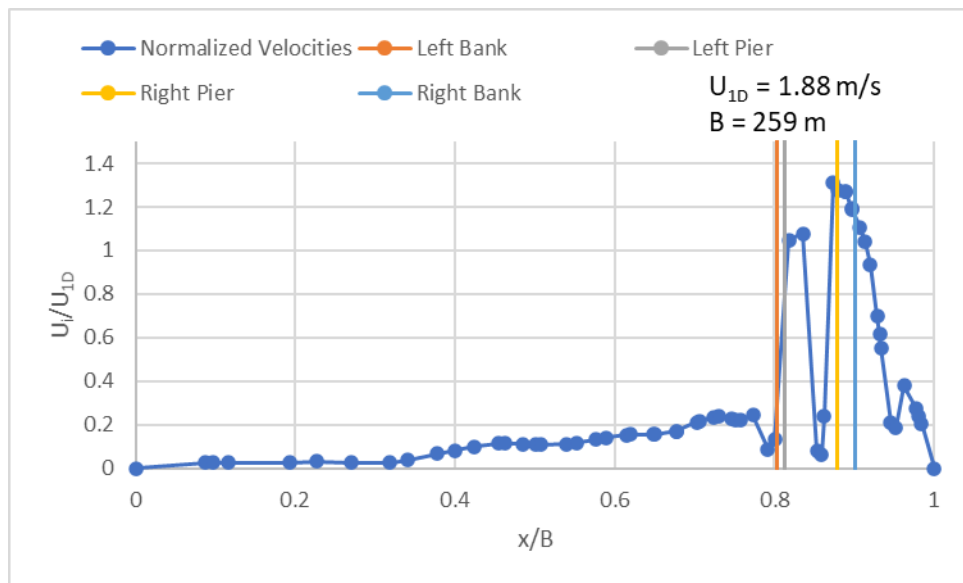


Figure B-20. The velocity profile created by SRH-2D for Middle Creek at $357 \text{ m}^3/\text{s}$.

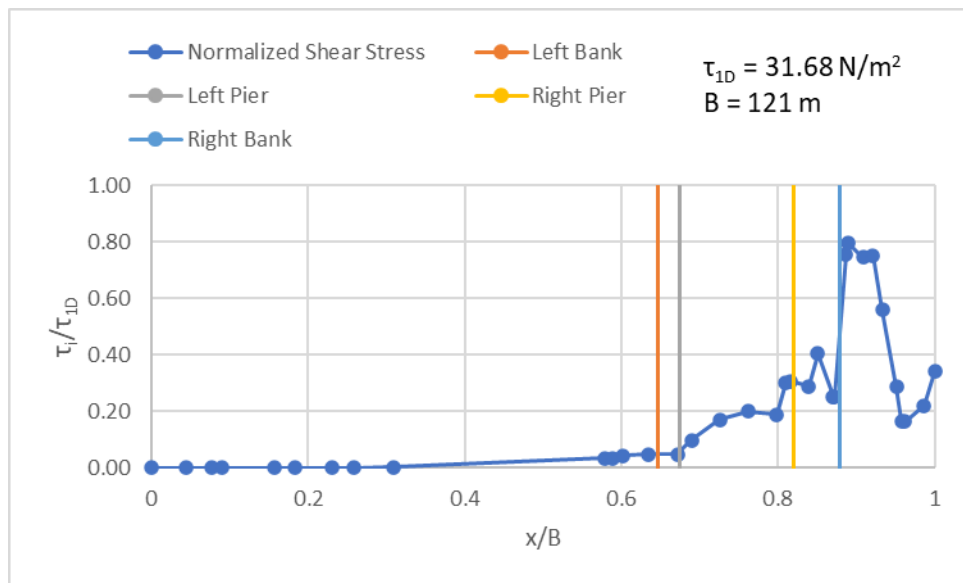


Figure B-21. The shear stress profile created by SRH-2D for Middle Creek at $173 \text{ m}^3/\text{s}$.

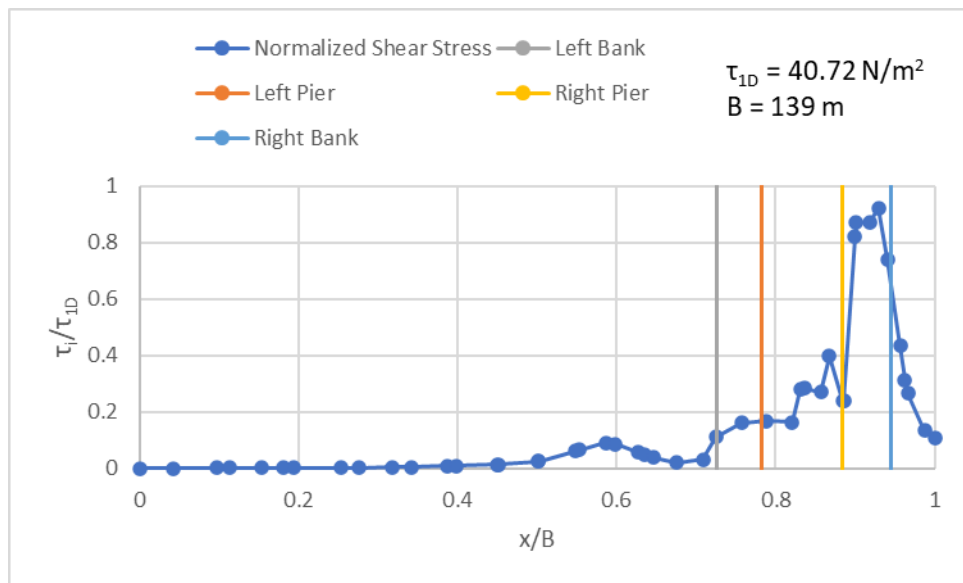


Figure B-22. The shear stress profile created by SRH-2D for Middle Creek at $246 \text{ m}^3/\text{s}$.

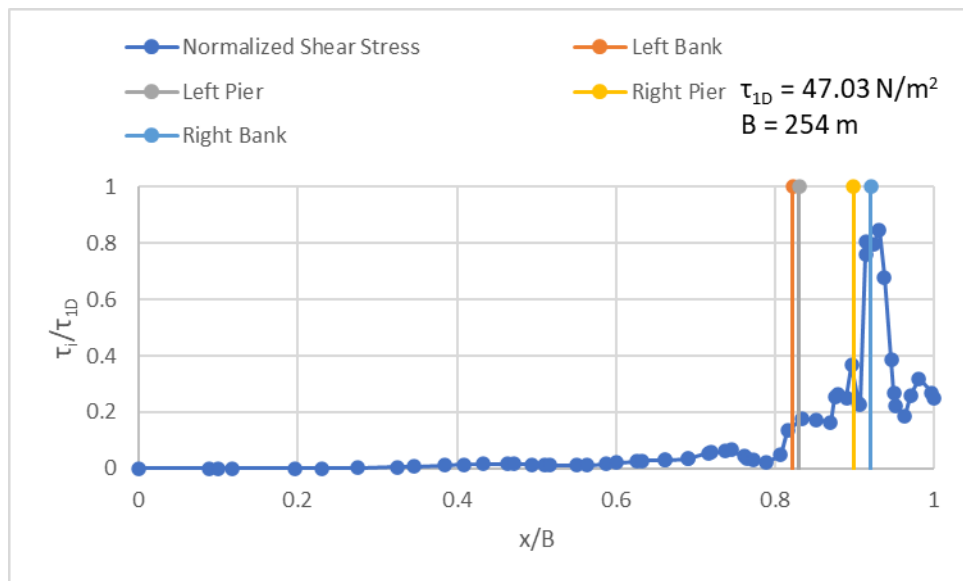


Figure B-23. The shear stress profile created by SRH-2D for Middle Creek at $301 \text{ m}^3/\text{s}$.

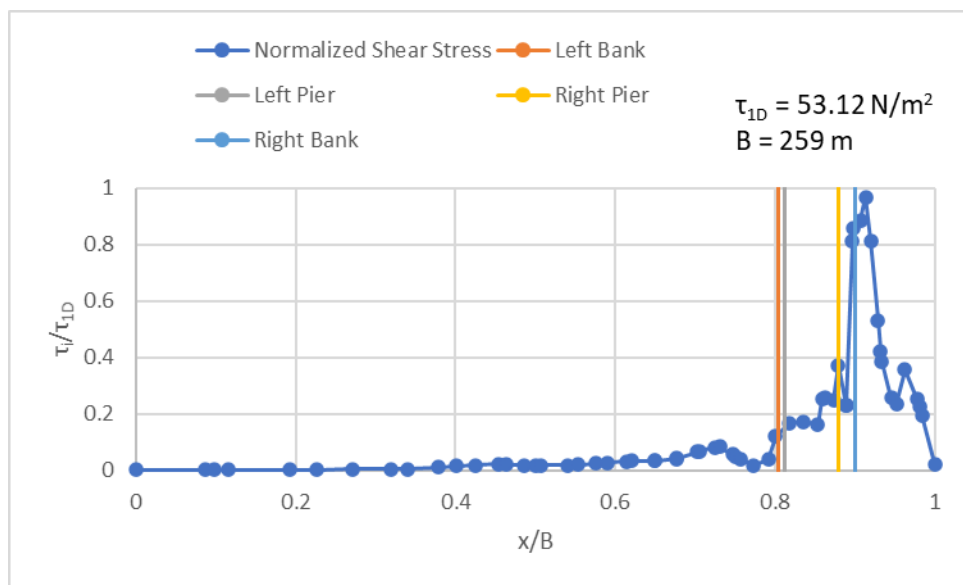


Figure B-24. The shear stress profile created by SRH-2D for Middle Creek at $357 \text{ m}^3/\text{s}$.

Tar River Hydraulic Results

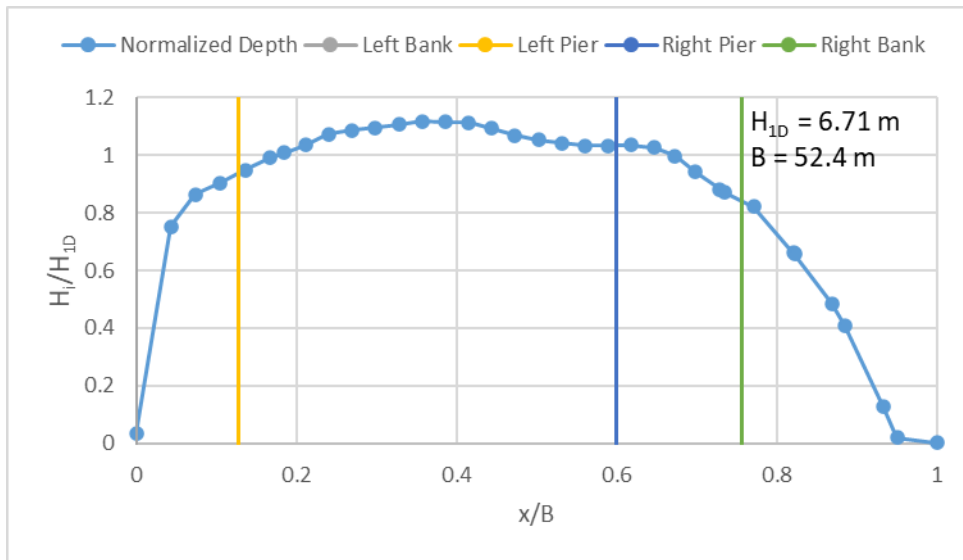


Figure B-25. The depth profile created by SRH-2D for Tar River at $390 \text{ m}^3/\text{s}$.

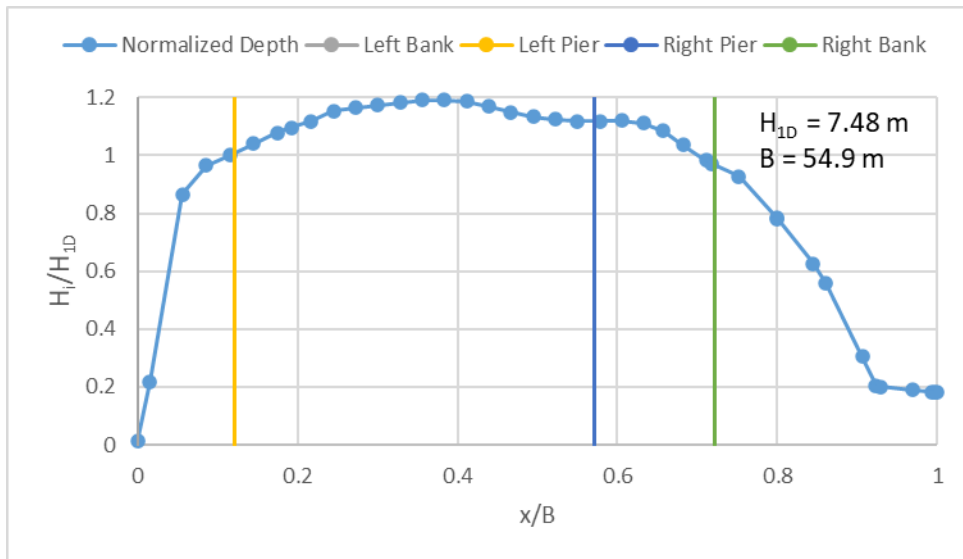


Figure B-26. The depth profile created by SRH-2D for Tar River at $514 \text{ m}^3/\text{s}$.

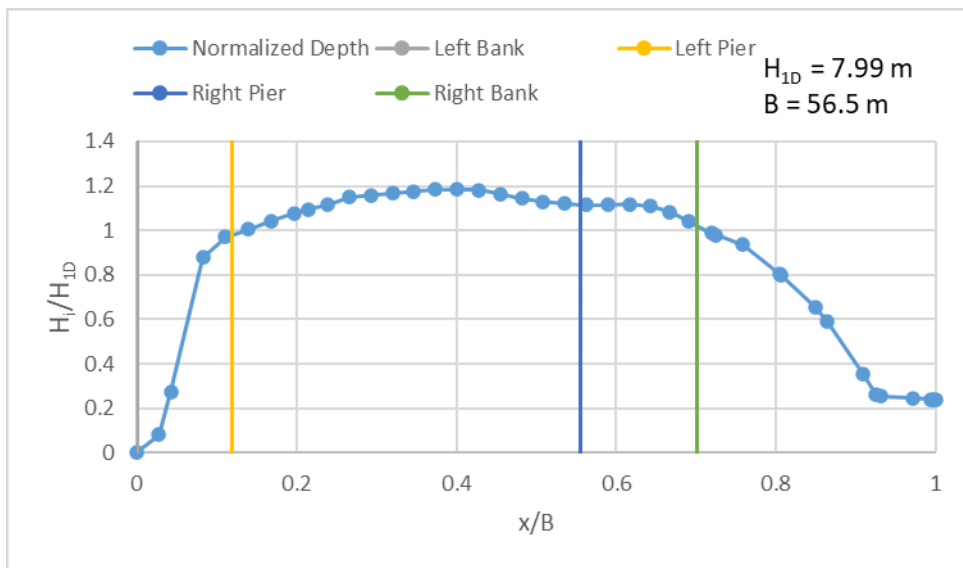


Figure B-27. The depth profile created by SRH-2D for Tar River at $609 \text{ m}^3/\text{s}$.

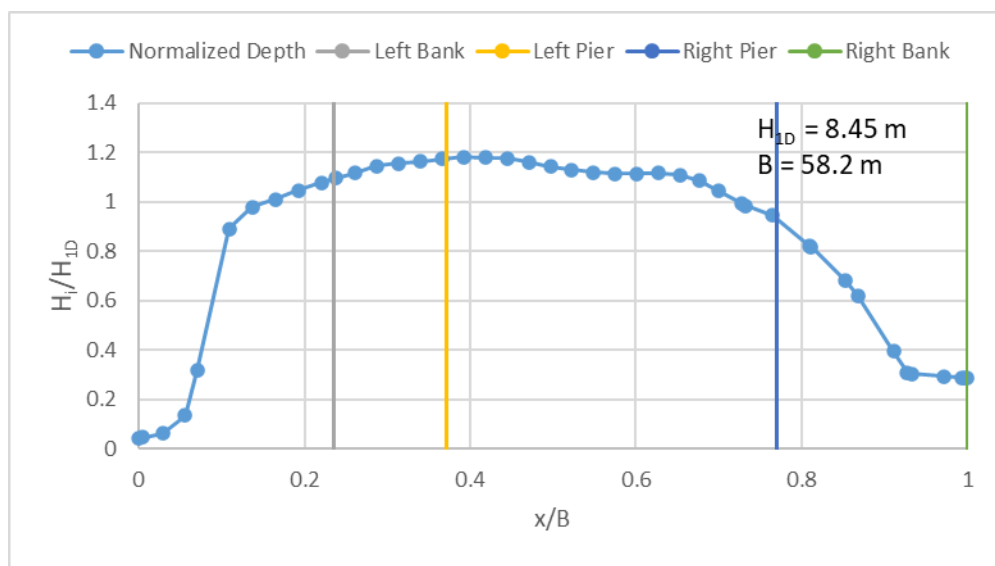


Figure B-28. The depth profile created by SRH-2D for Tar River at $703 \text{ m}^3/\text{s}$.

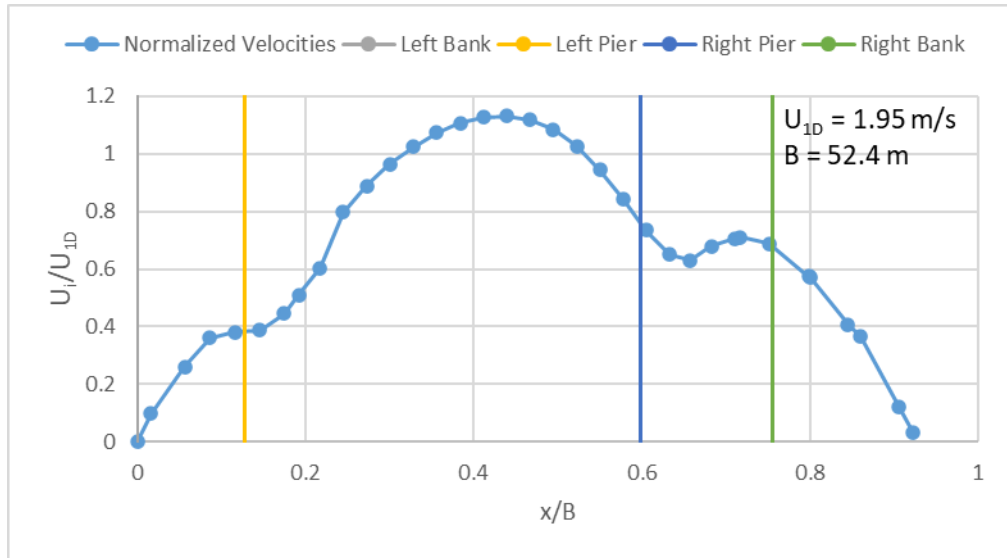


Figure B-29. The velocity profile created by SRH-2D for Tar River at $390 \text{ m}^3/\text{s}$.

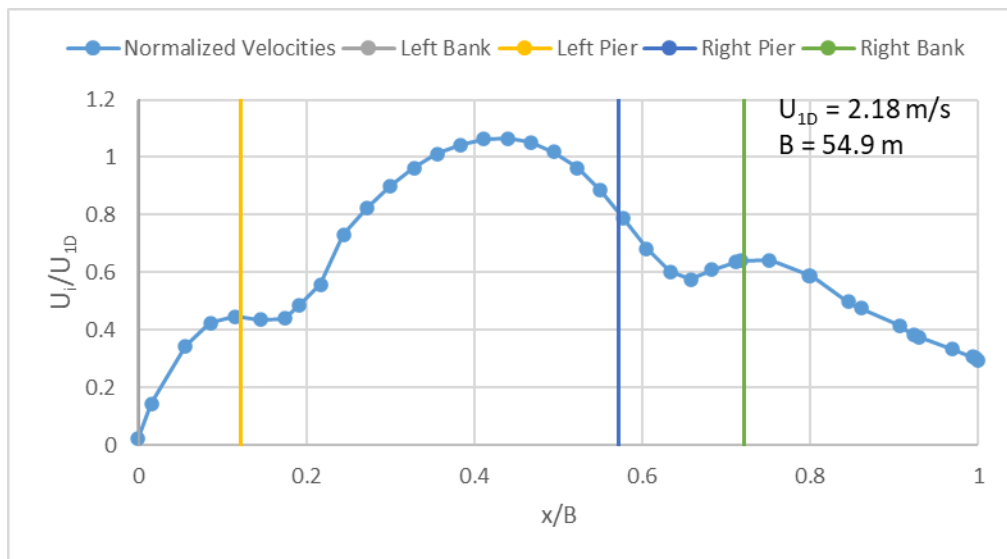


Figure B-30. The velocity profile created by SRH-2D for Tar River at $514 \text{ m}^3/\text{s}$.

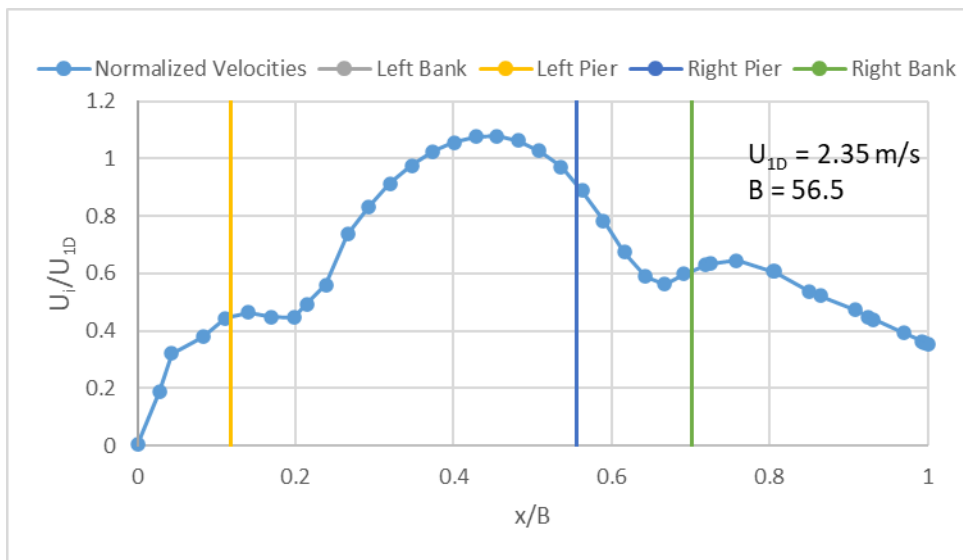


Figure B-31. The velocity profile created by SRH-2D for Tar River at $609 \text{ m}^3/\text{s}$.

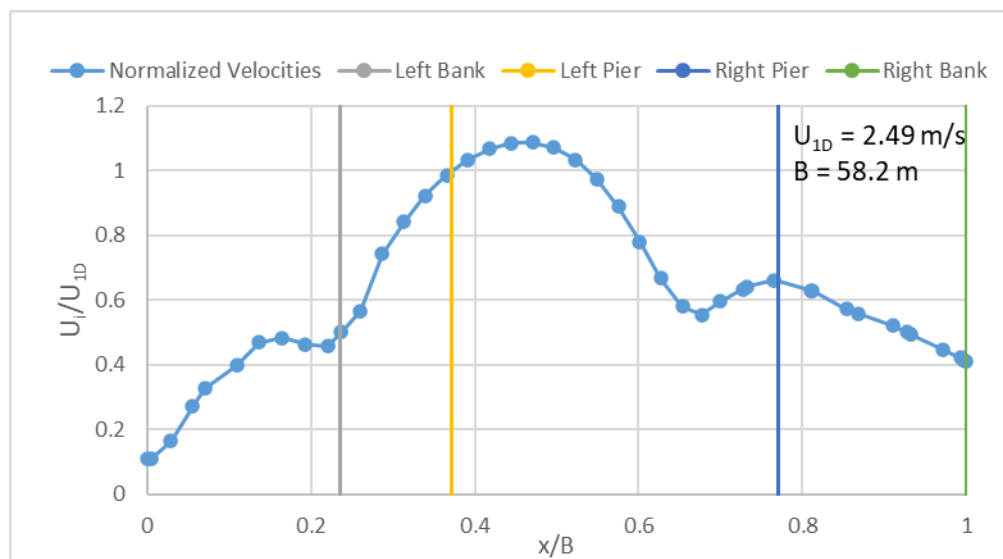


Figure B-32. The velocity profile created by SRH-2D for Tar River at $703 \text{ m}^3/\text{s}$.

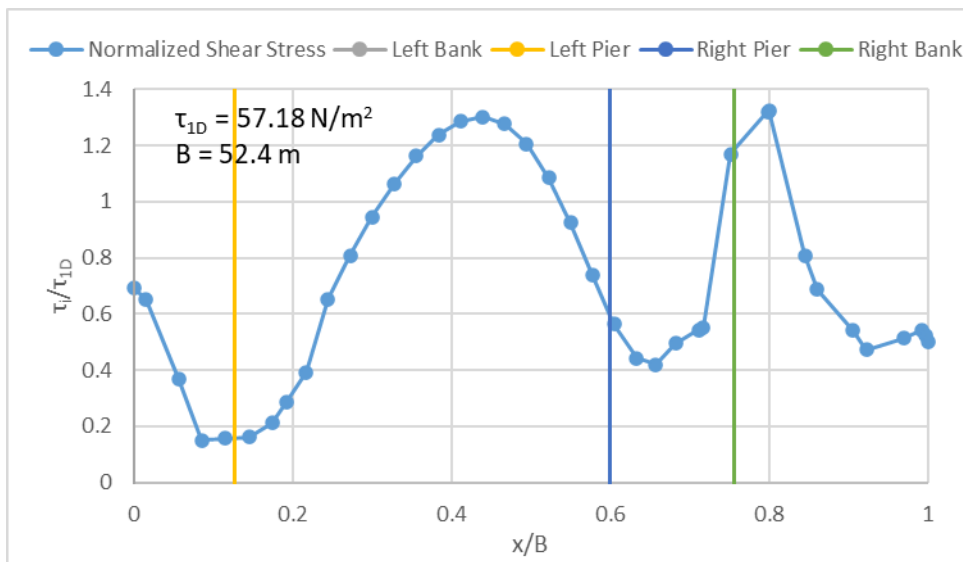


Figure B-33. The shear stress profile created by SRH-2D for Tar River at $390 \text{ m}^3/\text{s}$.

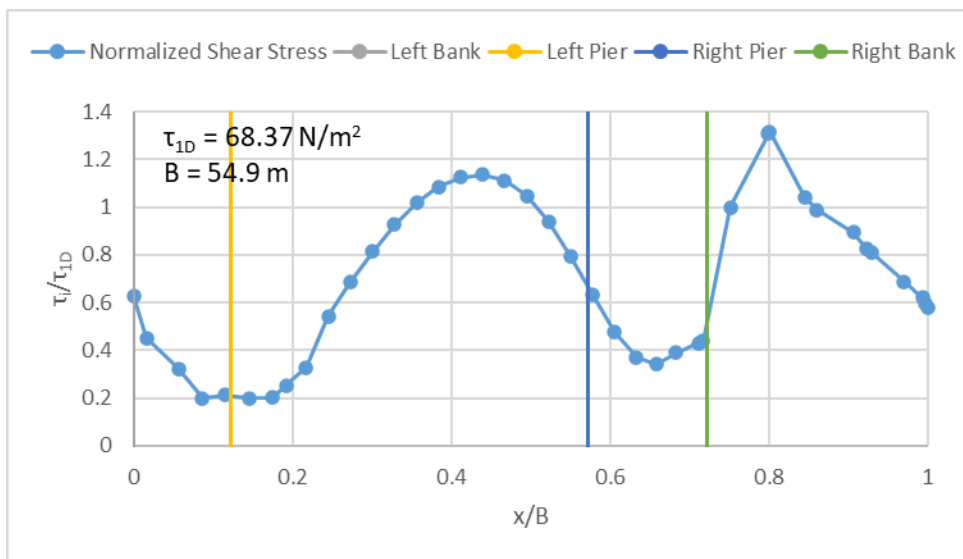


Figure B-34. The shear stress profile created by SRH-2D for Tar River at $514 \text{ m}^3/\text{s}$.

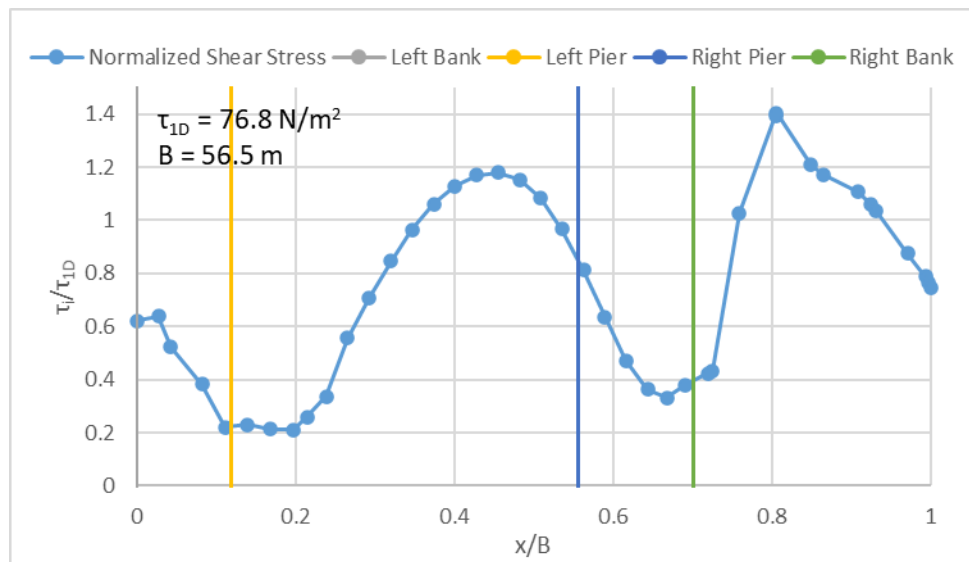


Figure B-35. The shear stress profile created by SRH-2D for Tar River at $609 \text{ m}^3/\text{s}$.

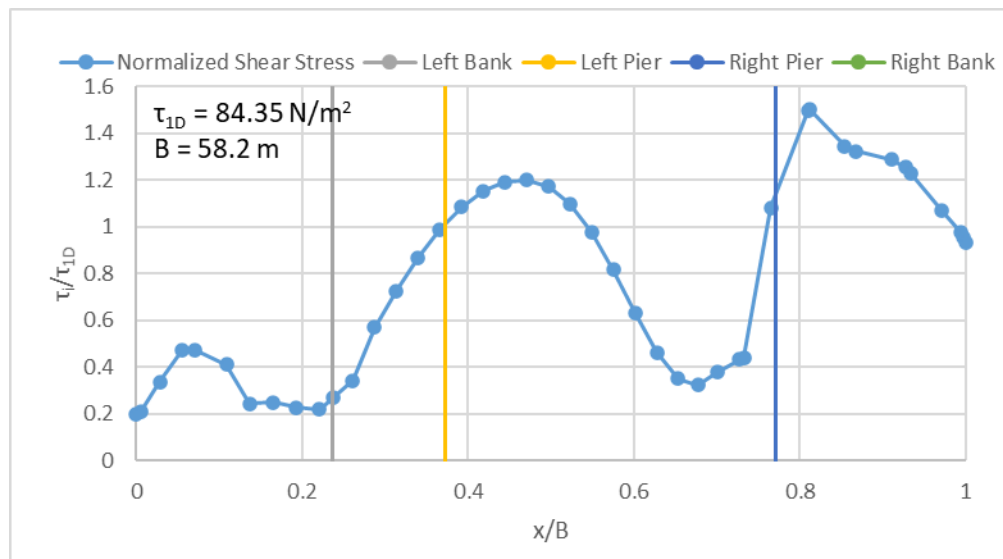


Figure B-36. The shear stress profile created by SRH-2D for Tar River at $703 \text{ m}^3/\text{s}$.

Roanoke River Hydraulic Results

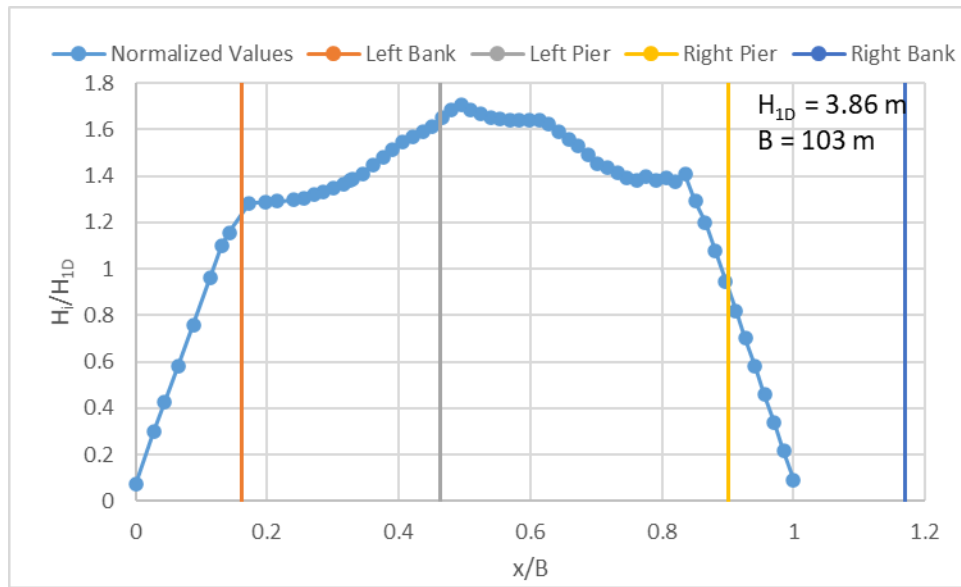


Figure B-37. The depth profile created by SRH-2D for Roanoke River at $203 \text{ m}^3/\text{s}$.

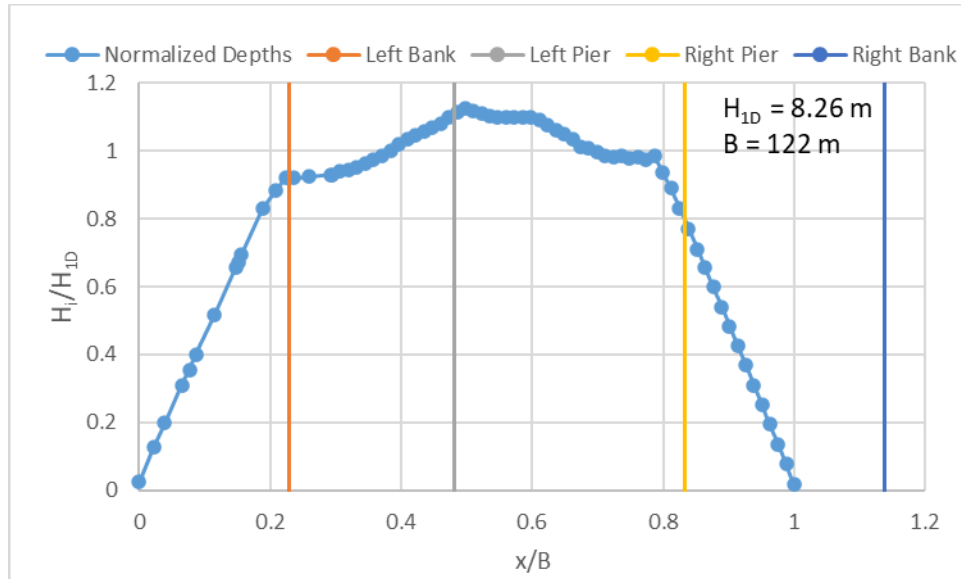


Figure B-38. The depth profile created by SRH-2D for Roanoke River at $997 \text{ m}^3/\text{s}$.

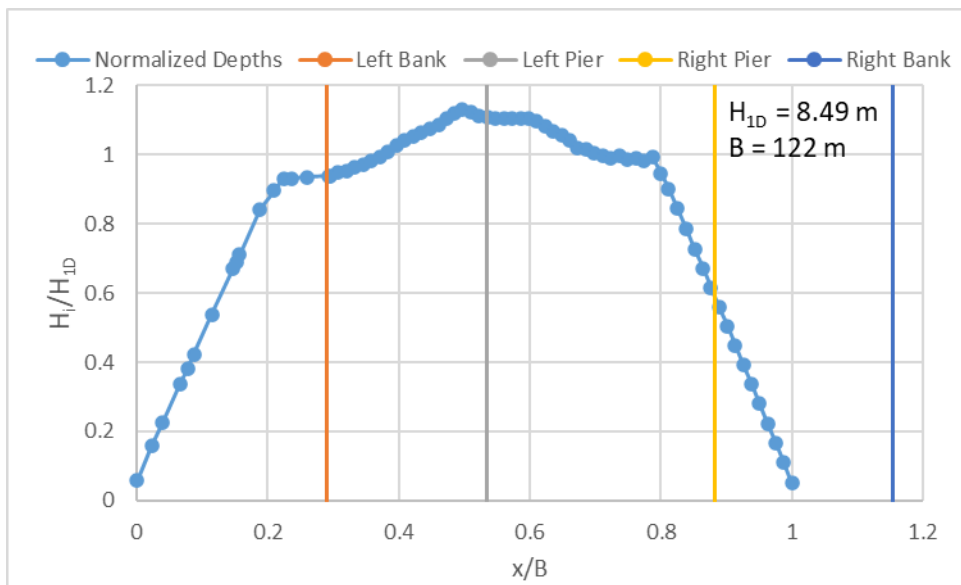


Figure B-39. The depth profile created by SRH-2D for Roanoke River at $1051 \text{ m}^3/\text{s}$.

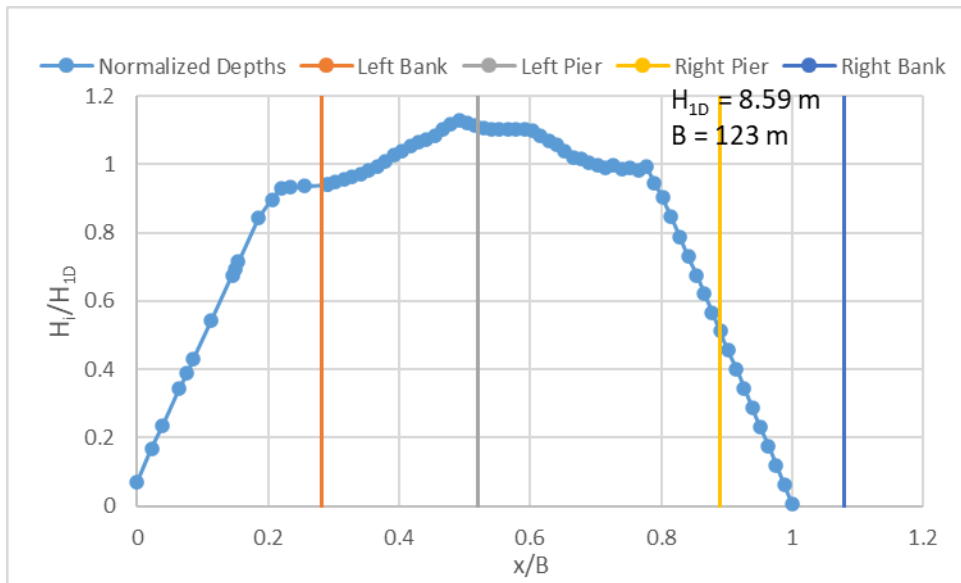


Figure B-40. The depth profile created by SRH-2D for Roanoke River at $1070 \text{ m}^3/\text{s}$.

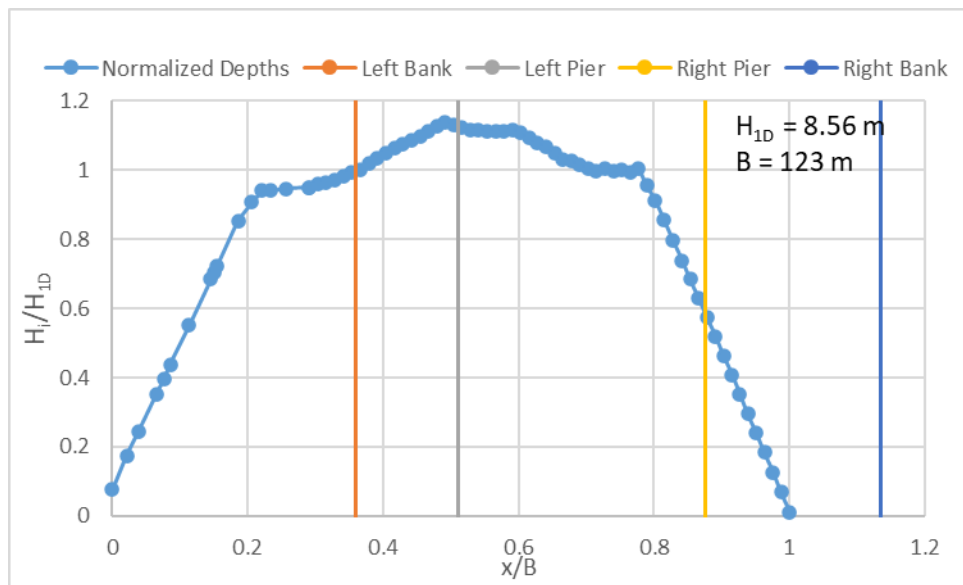


Figure B-41. The depth profile created by SRH-2D for Roanoke River at $1079 \text{ m}^3/\text{s}$.

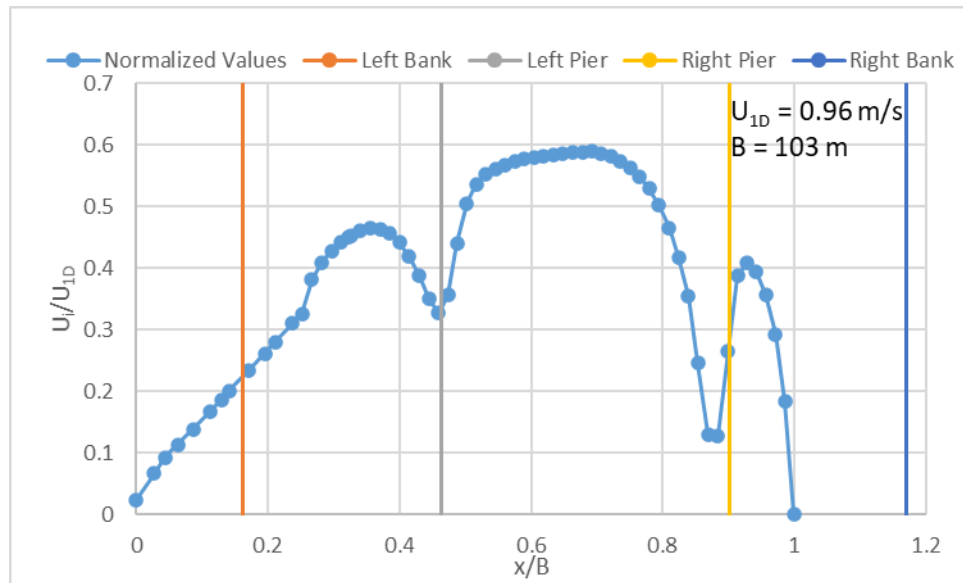


Figure B-42. The velocity profile created by SRH-2D for Roanoke River at $203 \text{ m}^3/\text{s}$.

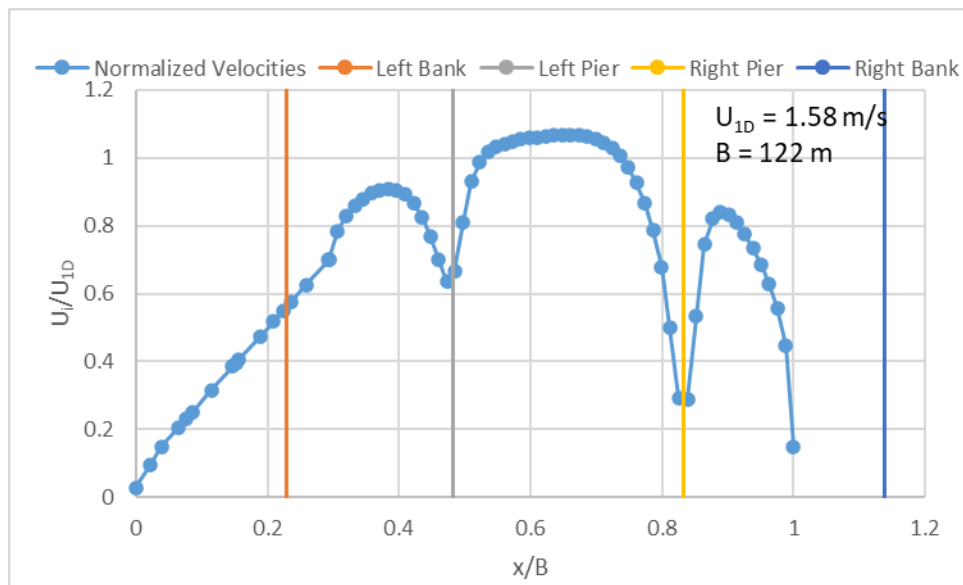


Figure B-43. The velocity profile created by SRH-2D for Roanoke River at $997 \text{ m}^3/\text{s}$.

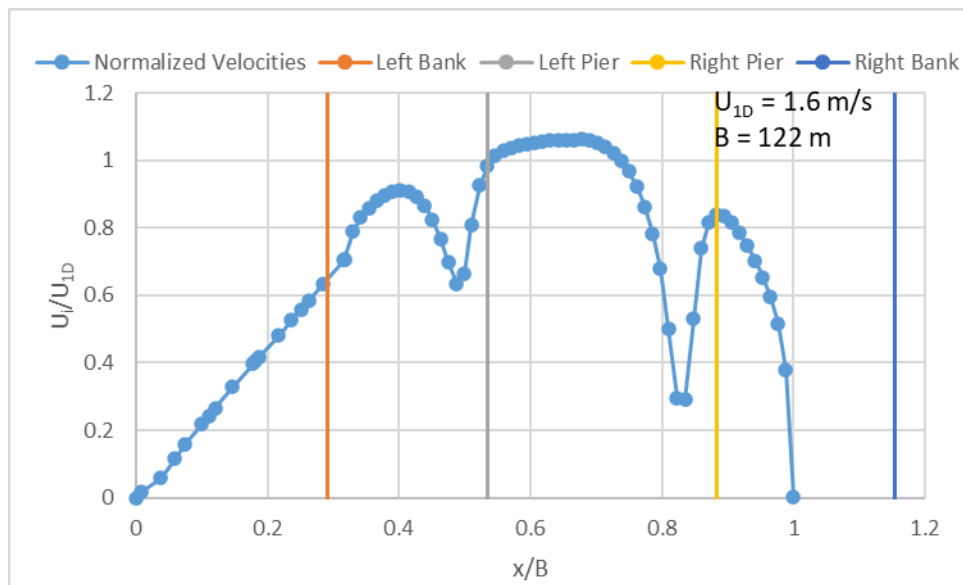


Figure B-44. The velocity profile created by SRH-2D for Roanoke River at $1051 \text{ m}^3/\text{s}$.

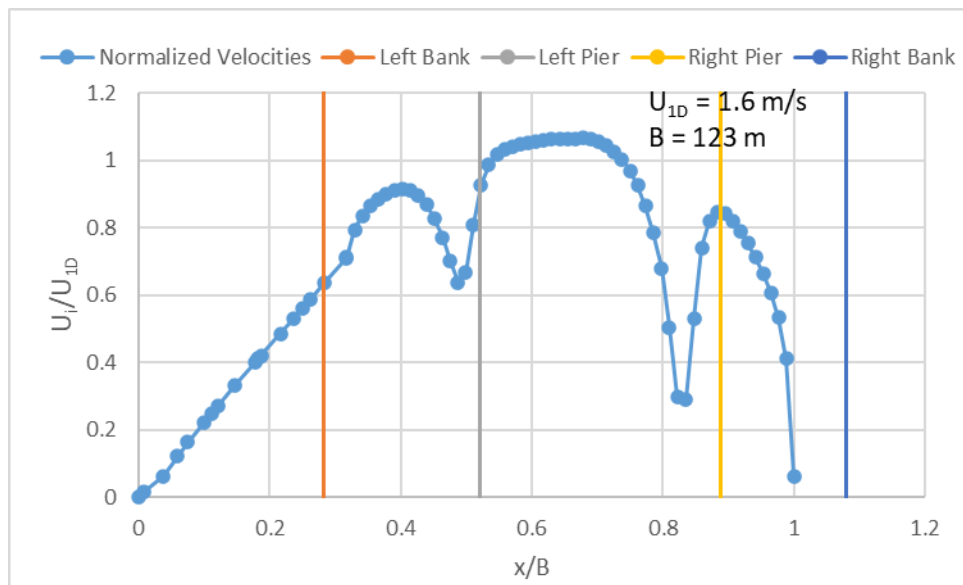


Figure B-45. The velocity profile created by SRH-2D for Roanoke River at $1070 \text{ m}^3/\text{s}$.

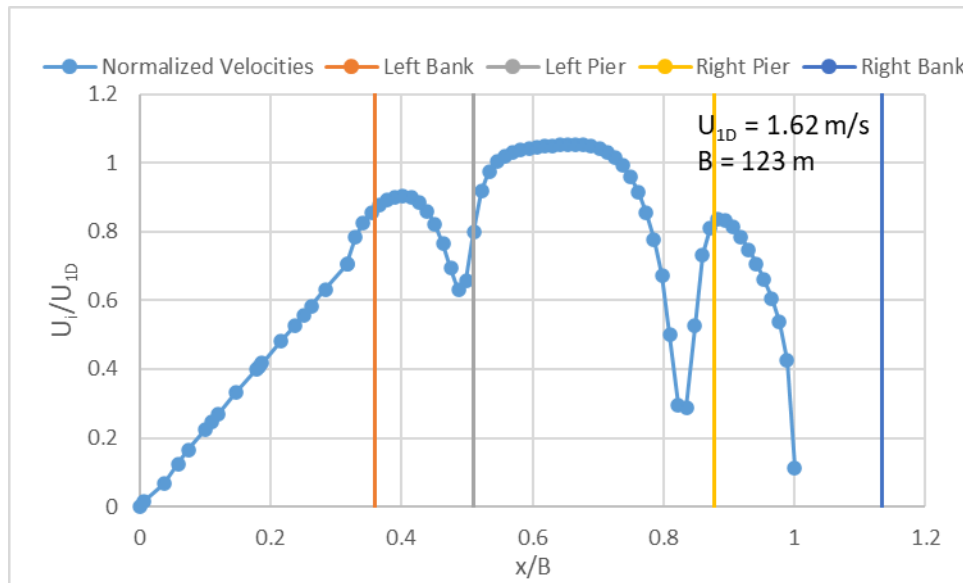


Figure B-46. The velocity profile created by SRH-2D for Roanoke River at $1079 \text{ m}^3/\text{s}$.

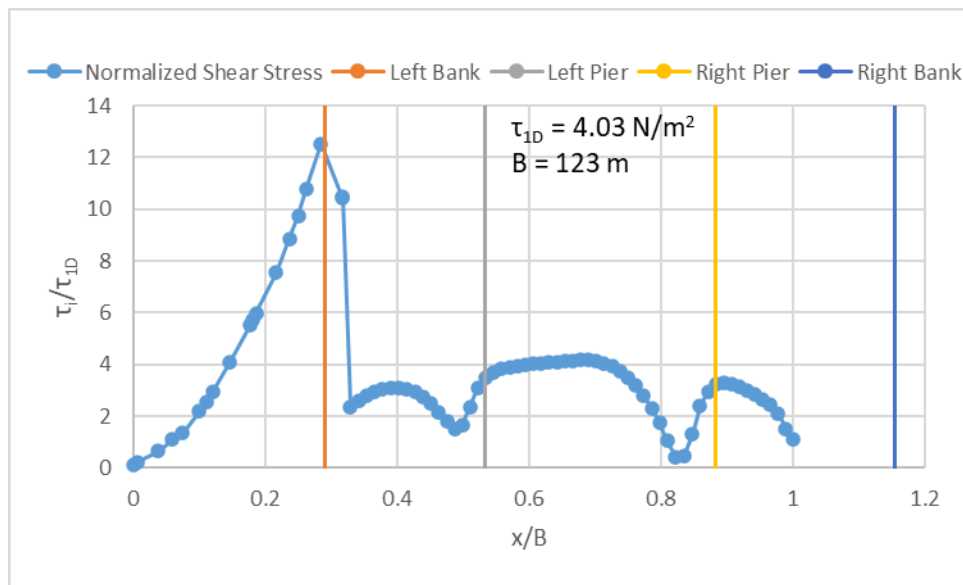


Figure B-47. The shear stress profile created by SRH-2D for Roanoke River at $1051 \text{ m}^3/\text{s}$.